

Multiparametric Cardiac Magnetic Resonance Imaging with Motion Compensation

vorgelegt von

M. Sc.

Kirsten Miriam Kerkering

ORCID: 0000-0002-8165-5943

an der Fakultät V - Verkehrs- und Maschinensysteme

der Technischen Universität Berlin

zur Erlangung des akademischen Grades

Doktorin der Ingenieurwissenschaften

-Dr.-Ing.-

genehmigte Dissertation

Promotionsausschuss:

Vorsitzender: Prof. Dr.-Ing. Marc Kraft

Gutachter: Prof. Dr. rer. nat. Tobias Schäffter

Gutachterin: Dr. Claudia Prieto Vasquez

Tag der wissenschaftlichen Aussprache: 06. Februar 2020

Berlin 2020

Zusammenfassung

Die Magnetresonanztomografie ist ein wichtiges medizinischen Bildgebungsverfahren für die Diagnose von kardiovaskulären Erkrankungen, da neben Anatomie und Herzfunktion auch Gewebeeigenschaften nicht-invasiv bestimmt werden können. Der Goldstandard für die Erkennung von Myokardschäden ist derzeit die kontrastmittelverstärkte Magnetresonanztomografie. Dieses Verfahren hat jedoch den Nachteil, dass gesundes Myokardgewebe im Bild vorhanden sein muss, um Pathologien von gesundem Gewebe abgrenzen zu können. Somit können nur fokale Veränderungen des Myokards identifiziert werden. Im Gegensatz dazu liefert die longitudinale Relaxationszeit T_1 unabhängig von dem umliegenden Gewebe Informationen über die Gewebeeigenschaften. Dies hat den Vorteil, dass auch diffuse Erkrankungen, die das komplette Myokard betreffen, diagnostiziert werden können. Da dieser Parameter quantitativ ist, und somit unabhängig von Messverfahren und Scannertyp, kann außerdem die Vergleichbarkeit von verschiedenen Messungen sichergestellt werden, sodass T_1 für die Überwachung eines Krankheitsverlaufes verwendet werden kann.

Die orts aufgelöste Bestimmung von T_1 , das T_1 -Mapping, ist sehr zeitintensiv, da eine Anzahl an qualitativen T_1 -gewichteten Bildern aufgenommen werden müssen, wodurch lange Aufnahmezeiten benötigt werden. Eine einzelne kardiovaskuläre Untersuchung besteht allerdings aus mehreren Aufnahmen, um alle für die Diagnose erforderlichen Informationen zu erhalten. Infolgedessen wird die Anwendung von T_1 -Mapping zur Zeit in der klinischen Routine nur begrenzt eingesetzt. Es werden schnelle Verfahren benötigt, die genaue T_1 -Werte liefern, jedoch die Aufnahmezeit nicht zusätzlich verlängern. Dies ist gerade für kardiovaskuläre Anwendungen aufgrund von Herz- und Atembewegungen äußerst herausfordernd.

In dieser Dissertation wurde ein multiparametrisches Verfahren entwickelt, mit dessen Hilfe T_1 und die Herzfunktion simultan bestimmt werden können, ohne die Aufnahmezeit zu verlängern. Unter Verwendung von einer neuen modellbasierten Bildrekonstruktionsmethode, die Vorwissen über den zu erwartenden Signalverlauf beinhaltet, konnten aus den unterabgetasteten Daten die T_1 -Werte akkurat bestimmt werden. Zudem konnte durch die Integration von Herzbewegungskorrekturtechniken die Aufnahmezeit zusätzlich reduziert werden, während die Präzision der T_1 -Bestimmung verbessert wurde. Die genannten Methoden wurden in Phantommessungen evaluiert und in gesunden Probanden und Patienten getestet.

Die vorgestellten Verfahren sind vielversprechend für die gleichzeitige Abbildung mehrerer klinisch relevanter Parameter durch effiziente Datenerfassung und -nutzung. Dieser multiparametrische Ansatz könnte für zukünftige Entwicklungen der kardiovaskulären Diagnostik wichtig sein, da die Aufnahme eine quantitative und kontrastmittelfreie Bildgebung in einer kurzen Zeit ermöglicht.

Abstract

Magnetic resonance imaging is a non-invasive imaging modality for the diagnosis of cardiovascular diseases. A broad range of diagnostic parameters can be obtained within a single examination, including information about morphology, physiology and tissue viability.

Currently, qualitative contrast-enhanced imaging is the gold standard for the detection of myocardial pathologies by visual assessment. In such qualitative approaches healthy myocardium has to be present in the image to have a contrast between healthy myocardium and pathological areas. Therefore, only focal myocardial defects can be accurately diagnosed. Recently, it has been shown that T_1 -relaxation times can be used to characterize myocardial pathologies even if they are not localized but affect the entire myocardium (diffuse disease). Furthermore, T_1 serves as a tissue specific quantitative diagnostic parameter which ensures comparability of different scans and allow for multi-centre studies and monitoring of disease progression or treatment response even over a long period of time.

T_1 mapping relies on the acquisition of a number of qualitative T_1 -weighted images to encode the recovery of longitudinal magnetization, resulting in long acquisition times. However, a cardiac examination consists of multiple scans in order to obtain all information needed for diagnostics, such as cardiac function, leaving little room for additional scan time. This hinders its application in clinical practice. Therefore, fast and robust T_1 mapping techniques have to be developed, without prolonging examination time or loss in accuracy or precision. Furthermore, cardiac T_1 mapping is very challenging because of cardiac and respiratory motion.

In this thesis, a multiparametric magnetic resonance imaging technique was developed to increase the efficiency of data acquisition. Using this approach, accurate T_1 maps and functional images were obtained simultaneously without prolongation of the scan time. High-resolution T_1 mapping was realized by advanced model-based image reconstruction that utilizes prior knowledge of T_1 recovery to obtain accurate T_1 estimation. By integration of cardiac motion correction techniques based on the reconstructed functional images, the scan duration was reduced by 50%, while precision of T_1 mapping was increased. The presented techniques were evaluated in phantoms and feasibility was shown in healthy volunteers and in patients.

The imaging approaches proposed in this thesis have been demonstrated to hold great promise for simultaneous imaging of multiple clinically relevant parameters by efficient data sampling and advanced image reconstruction methods. The multiparametric approach could be important for future directions in cardiovascular magnetic resonance imaging, because the fast and contrast-free examination allows for quantitative imaging in a short examination time.

Acknowledgements

The last years have been an exciting and challenging experience for me and this work could never have happened without the help of many people. First and foremost, I am deeply grateful to my supervisor Dr. Christoph Kolbitsch for his professional and personal support throughout the last years. He taught me that there were more ways than just a Fourier transform to reconstruct MR images and always offered his time when I needed it. His guidance, knowledge and patience contributed greatly to this work.

I would like to thank Prof. Dr. Tobias Schäffter for his constructive and invaluable advice, immensely improving the quality of the work. I learned a lot from his broad experiences in imaging research.

My sincere thanks goes to my supervisor Prof. Dr. Jeanette Schulz-Menger. Her advice and clinical input have been crucial to ensure that the developed methods are meaningful for patients. She also facilitated multidisciplinary collaborations and ongoing discussions, which is the key for our research.

I am grateful to Prof. Dr. Marc Kraft giving me the opportunity to be part of TU Berlin and for being the chairman of the doctoral committee.

I am obliged to all of my colleagues of our MRI department for their support. Thanks to Dr. Bernd Itterman for providing a pleasant research environment. In particular I would like to thank Juliane, Ariane, Clarissa, Johannes, Semiha, Jean-Pierre, Layla, Sebastian, Sebastian, Rüdiger, Frank W and Karin for their help and for the enjoyable time we spent together at PTB, conferences, holidays and Kowski. André and Sven worked together with me on the T_1 project for several month. Thanks for your commitment.

I also thank Dr. Edyta Blaszczyk, Dr. Stephanie Wiesemann, Kerstin Kretschel, Denise Kleindienst and Evelyn Polzin for answering all of my clinically-related questions, showing me the CMR routine, acquiring data and for your time in the evenings, when we implemented and tested our methods at your scanner.

I also want to thank all volunteers spending their time for me in the scanner.

Finally, I would like to thank my family and friends. They always gave me support to accomplish my personal goals, no matter what project I started or to which city I moved. Especially, I would like to thank Janis for his ongoing explanations of the biomedical part of the work, proofreading of the thesis and for always believing in me. Without the encouragement and motivation of my family and friends, I would not have been able to complete my PhD thesis.

Table of Contents

List of Figures	xiii
List of Tables	xv
Abbreviations	xvii
1 Introduction	1
1.1 Scope of the thesis	3
1.2 Outline	3
2 Cardiac MRI	5
2.1 Cardiac function	6
2.2 Assessment of cardiac function	8
2.3 Myocardial tissue characterization	9
2.4 Assessment of myocardial viability	10
2.4.1 Contrast enhanced imaging	10
2.4.2 Quantitative MRI for myocardial viability	11
2.4.3 T_1 mapping principles	12
2.4.4 Cardiac T_1 mapping techniques and challenges	13
3 Continuous Acquisition for cardiac T_1 Mapping	19
3.1 Introduction	19
3.2 Methods	20
3.2.1 Model function of longitudinal magnetization	20
3.2.2 Optimization of data acquisition for cardiac T_1 mapping	21
3.2.3 Influence of cardiac motion on T_1 mapping accuracy	22
3.2.4 Influence of blood inflow on T_1 mapping accuracy	23
3.3 Results	24
3.3.1 Optimization of data acquisition for cardiac T_1 mapping	24
3.3.2 Influence of cardiac motion on T_1 mapping accuracy	26
3.3.3 Influence of blood inflow on T_1 mapping accuracy	27
3.4 Discussion	28
3.5 Conclusion	29

TABLE OF CONTENTS

4	Simultaneous T_1 Mapping and Cine imaging using iterative model-based Reconstruction	31
4.1	Introduction	31
4.2	Methods	32
4.2.1	Data acquisition	32
4.2.2	Iterative T_1 reconstruction	33
4.2.3	Cine reconstruction	34
4.2.4	Experiments	35
4.2.5	Numerical simulations	35
4.2.6	Phantom experiments	35
4.2.7	In vivo study	36
4.3	Results	37
4.3.1	Numerical simulations	37
4.3.2	Phantom experiments	40
4.3.3	In vivo study	40
4.4	Discussion	46
4.5	Conclusion	49
5	High-resolution T_1 Mapping of all four Chambers	51
5.1	Introduction	51
5.2	Methods	53
5.2.1	T_1 mapping	53
5.2.2	In vivo imaging	53
5.3	Results	53
5.4	Discussion	55
5.5	Conclusion	55
6	Native T_1 Mapping using cardiac motion correction	57
6.1	Introduction	57
6.2	Methods	58
6.2.1	Data acquisition	59
6.2.2	Cine reconstruction	59
6.2.3	Motion estimation	59
6.2.4	Motion corrected T_1 mapping	60
6.2.5	Phantom experiments	60
6.2.6	In vivo experiments	61
6.2.7	Analysis	62
6.3	Results	63
6.3.1	Phantom experiments	63
6.3.2	Cine reconstruction	63
6.3.3	Motion estimation	65
6.3.4	Native T_1 mapping	66
6.3.5	Impact of scan time on T_1 mapping	70

6.3.6	Repeatability of T_1 mapping	70
6.4	Discussion	70
6.5	Conclusion	77
7	Assessment of Myocardial Scar using post-contrast T_1 Mapping	79
7.1	Introduction	79
7.2	Methods	80
7.2.1	Data acquisition and cine reconstruction	80
7.2.2	Iterative model-based T_1 mapping	80
7.2.3	Cardiac motion corrected T_1 mapping	80
7.2.4	In vivo experiments	81
7.2.5	Evaluation of post-contrast T_1 mapping	81
7.3	Results	82
7.3.1	Iterative model-based T_1 mapping	82
7.3.2	Motion corrected T_1 mapping	84
7.4	Discussion	86
7.5	Conclusion	88
8	Combining model-based Reconstruction and cardiac motion corrected T_1 Mapping	89
8.1	Introduction	89
8.2	Methods	89
8.3	Results	91
8.4	Discussion	92
8.5	Conclusion	93
9	Summary	95
	References	99
	List of Author's Publications	109

List of Figures

2.1	Anatomy of the heart	5
2.2	Heart as a pump	6
2.3	Electrocardiogram.	7
2.4	Cine imaging.	8
2.5	Pathology of myocardial fibrosis.	10
2.6	Late gadolinium enhancement for visualization of fibrosis.	11
2.7	Recovery of longitudinal magnetization.	13
2.8	Recovery of Look-Locker acquisition.	14
2.9	T_1 mapping approach using 3(3)3(3)5 MOLLI.	15
3.1	Longitudinal relaxation curve applying multiple inversions.	21
3.2	Relaxation curve and data selection in cardiac T_1 mapping.	22
3.3	Optimization of flip angle using the Ernst angle.	24
3.4	Relaxation curve including multiple inversions and data selection in cardiac T_1 mapping.	25
3.5	T_1 mapping accuracy for different intervals between inversion pulses.	25
3.6	Impact of through-plane motion.	26
3.7	Impact of inflowing blood.	27
4.1	Data acquisition and selection for model-based image reconstruction.	33
4.2	Iterative model-based image reconstruction.	34
4.3	Simulated T_1 map and images of all coils.	38
4.4	Reference and reconstructed TI images.	38
4.5	Evolution of k-space and images during iterative process in numerical phantom.	39
4.6	Convergence behaviour of estimated T_1 in blood and myocardium over iterations in numerical phantom.	39
4.7	Phantom evaluation.	40
4.8	Evolution of all fitted parameter in a healthy subject.	41
4.9	Evolution of in vivo T_1 times.	41
4.10	T_1 maps of five healthy volunteers in SAX view.	42
4.11	T_1 maps of two healthy volunteers in 4ChV.	42
4.12	Reproducibility of T_1 mapping.	43
4.13	Cine T_1 maps.	44
4.14	Reconstructed cine images and reference cine scan.	45

LIST OF FIGURES

4.15	Functional analysis of the cine images.	45
4.16	Systolic T_1 maps with different acquisition windows and slice profiles.	48
5.1	T_1 mapping of all four chambers.	52
5.2	T_1 maps of two subjects in 4ChV.	54
5.3	T_1 map through both atria.	54
5.4	Result of the voxel-wise T_1 fitting.	54
5.5	Overlay of T_1 and anatomy.	55
6.1	Data acquisition and cardiac motion estimation.	58
6.2	T_1 mapping using 80% of the cardiac cycle.	61
6.3	Phantom validation of motion corrected T_1 mapping.	64
6.4	SAX cine images.	64
6.5	4ChV cine images.	64
6.6	Motion correction on 8 s cine images.	65
6.7	Estimated motion of two subjects in 16 s and 8 s.	66
6.8	Deformation in each myocardial segment for 16 s and 8 s.	66
6.9	Impact of motion on uncorrected T_1 map at different heart rates.	67
6.10	Impact of motion correction on T_1 maps.	67
6.11	Native T_1 maps in 8 s of three healthy subjects.	68
6.12	Native T_1 maps in 8 s and 4ChV.	69
6.13	Maps of all estimated parameter.	69
6.14	T_1 times and spatial variation of T_1 in 8 s.	70
6.15	Stack of SAX slices.	71
6.16	Impact of scan time on T_1 times and spatial variations of T_1 across the myocardium.	71
6.17	Repeatability of myocardial motion estimation.	72
6.18	Repeatability of motion corrected T_1 mapping in 8 s.	72
6.19	Impact of scan time on motion corrected T_1 mapping.	76
6.20	Motion corrected T_1 maps for different spatial resolutions.	77
7.1	Data acquisition, cine imaging and T_1 mapping.	80
7.2	Post-contrast cine images from 8 s acquisition.	82
7.3	LGE images, model-based T_1 maps and bull's eye plots.	83
7.4	Bland-Altman analysis for diastolic and systolic T_1 and spatial variation. . . .	83
7.5	Estimated deformation of the left ventricle in post-contrast cine images. . . .	84
7.6	Cine images and motion correction after contrast administration.	84
7.7	LGE images, motion corrected T_1 maps and bull's eye plots.	85
7.8	Box-Whisker plots of T_1 times and precisions averaged over all patients. . . .	86
8.1	Methods of motion corrected model-based T_1 mapping.	90
8.2	Motion corrected model-based T_1 maps.	91

List of Tables

2.1	Literature T_1 times for MOLLI and SASHA.	16
4.1	T_1 times across ten healthy subjects using iterative model-based reconstruction.	43
5.1	T_1 times of all four chambers.	53
8.1	T_1 times and precision of motion corrected model-based T_1 mapping for different scan durations.	92

Abbreviations

1D	one-dimensional.
2D	two-dimensional.
3D	three-dimensional.
4ChV	four-chamber view.
ASAX	apical short axis.
bpm	beats per minute.
bSSFP	balanced steady-state free-precession.
CMR	cardiovascular magnetic resonance.
CO	cardiac output.
CT	computed tomography.
CVD	cardiovascular disease.
ECG	electrocardiogram.
ECM	extracellular matrix.
ECV	extracellular volume.
EDV	end-diastolic volume.
EF	ejection fraction.
ESV	end-systolic volume.
FFT	fast fourier transformation.
FOV	field of view.
GRE	gradient echo.
GROG	self-calibrating GRAPPA operator gridding.
IR	inversion recovery.
LA	left atrium.
LGE	late gadolinium enhancement.
LV	left ventricle.
MOLLI	modified Look-Locker inversion recovery.
MRI	magnetic resonance imaging.
PET	positron emission tomography.
RA	right atrium.
rf	radiofrequency.
RMS	root mean square.
ROI	region of interest.
RV	right ventricle.

Abbreviations

R^2	coefficient of Determination.
SAPPHIRE	saturation-pulse prepared heart-rate independent inversion-recovery.
SASHA	saturation-recovery single-shot acquisition.
SAX	short axis.
SE	spin echo.
SNR	signal-to-noise ratio.
SPECT	single-photon emission computed tomography.
SR	saturation recovery.
STD	standard deviation.
SV	stroke volume.
TE	echo time.
TI	inversion time.
TR	repetition time.
T_1	longitudinal relaxation time.
T_2	transverse relaxation time.
T_2^*	effective transverse relaxation.
T_{ic}	interval between inversions.

1

Introduction

In the last two decades, improved therapy led to a reduction of mortality in patients with cardiovascular diseases (CVDs) by up to 40% [1]. Adequate therapy relies on accurate diagnostics, disease staging, treatment planning and patient monitoring. Thus, advances in medical imaging play an important role for the treatment of CVD patients.

Several medical imaging modalities can be used to diagnose CVDs. Echocardiography is a widely used method, because it is cheap and easy to use at the bedside of the patient. Nevertheless, signal-to-noise ratio (SNR) is low and the choice of the imaging plane is limited and highly user dependent. Computed tomography angiography yields excellent visualization of coronary arteries with high spatial and temporal resolution, but involves ionizing radiation and iodine-containing contrast agents to enhance the otherwise low soft tissue contrast. Nuclear imaging modalities, such as positron emission tomography (PET) and single-photon emission computed tomography (SPECT), are reliable imaging modalities for myocardial perfusion, but radiotracers are required and spatial resolution and SNR are low, making detection of small abnormalities difficult.

Magnetic resonance imaging (MRI) is more expensive than echocardiography and slower compared to computed tomography (CT), but offers excellent inherent soft tissue contrast and does not require any ionizing radiation. The main advantage of MRI is that a broad range of diagnostic parameters can be obtained within a single examination, including information about morphology, physiology and tissue viability. In cardiovascular magnetic resonance (CMR), an examination often includes assessment of myocardial wall motion, chamber volumes, stroke volume, valve function, blood flow patterns, tissue viability and perfusion, which can be measured in arbitrary imaging planes, covering the whole heart non-invasively. This allows for a differential diagnosis of a broad range of cardiac diseases, such as cardiomyopathies, carditis, valvular diseases and infarction.

Myocardial fibrosis, a remodeling of cardiac tissue composition, is involved in many ischemic and non-ischemic cardiac diseases [2, 3, 4] and therefore it is an important marker for the detection, grading and prognosis of these diseases. Currently, late gadolinium enhancement (LGE) MRI is the gold standard for the detection of ischemic heart diseases in clinical routine,

1. INTRODUCTION

where images are obtained after application of a contrast agent [5]. Differences in washing-out kinetics between healthy and fibrotic tissue result in higher signal intensities in fibrosis compared to healthy myocardium [6]. A disadvantage of LGE for the verification of fibrotic tissue is that the presence of healthy myocardium is needed in the image in order to have a contrast between healthy myocardium and areas with defects, because the LGE images are purely qualitative. In these qualitative images, signal intensities are not just dependent on biophysical parameters of the tissue, such as proton density, the longitudinal relaxation time (T_1) and the transverse relaxation time (T_2), but also on a range of external parameters, such as measurement settings, scanner type or institution. Therefore, healthy reference tissue has to be present in the image and only focal myocardial defects can be diagnosed. For a pathology which affects the entire myocardium, LGE cannot be used because no healthy myocardium is in the image for reference. To detect these diseases, techniques have to be used which provide direct information of tissue viability, independent of the surrounding tissue.

In contrast to qualitative imaging, quantitative MRI provides direct information of intrinsic biophysical parameters. In MRI a range of different biophysical parameters can be measured allowing for diagnosis of different diseases. The spatially resolved measurement of biophysical parameters is often called mapping, providing images with the relaxation time of the tissue in each voxel. For cardiac applications, the relaxation time T_1 has been shown to be a good marker for myocardial diseases [7, 8, 9, 10]. In contrast to LGE, T_1 mapping does not require healthy reference tissue and is the only non-invasive imaging modality that allows for the detection of diffuse myocardial fibrosis. This could be important in the context of diseases such as rheumatoid arthritis, systemic sclerosis, amyloidosis or hypertrophic cardiomyopathy [11, 12, 7, 13]. Beyond this, not only the presence of a pathology could be detected, but the exact T_1 times of the myocardium could be used as an indication for the classification of a disease. For example, T_1 values are elevated in amyloidosis and myocardial infarction, but lowered in iron-overload and intracellular lipid disorders [7]. The quantitative property of T_1 mapping provides comparability between measurements, patients and scanner. Hence, it can also be employed for monitoring of treatment response. More important, T_1 mapping can be applied without the need for contrast agents.

Despite the great potential of cardiac T_1 mapping, T_1 mapping is not fully used in clinical routine. The main problem of T_1 mapping are long examination times, which hinders its clinical application, especially for cardiac examinations. The three main challenges are:

1. For the diagnosis of cardiac diseases using CMR, various parameters (e.g. anatomy and cardiac function) have to be obtained in multiple scans during one examination in order to obtain all information needed for diagnostics, leaving little room for additional scan time.
2. For each two-dimensional (2D) T_1 map, multiple 2D qualitative images have to be acquired, leading to long scan times. Therefore, T_1 mapping is exceedingly challenging for its application in the heart, handling with respiratory motion. In order to minimize artefacts due to respiratory motion of the heart, patients are asked to hold their breath during data acquisition. All data is usually acquired during one single breath hold of

several seconds. Therefore, current T_1 mapping techniques lack accuracy, so comparability between sequences is not given and its full potential is not yet reached [14, 15, 16].

3. Data acquisition has to be synchronised with the heart beat, to ensure data is always acquired in the same cardiac phase (cardiac triggering) to avoid cardiac motion artefacts. In only about 15% of the overall scan time data is acquired, leading to a highly inefficient scan and resulting in low precision or low spatial resolution of the obtained T_1 maps. This also implies that the T_1 map shows only one cardiac phase and all information about cardiac function is lost. However, the information about cardiac wall motion is one of the most important parameters for diagnostics.

Therefore, fast and robust T_1 mapping techniques for the heart have to be developed, without prolonging examination time or loss in accuracy or precision.

1.1 Scope of the thesis

The work presented in this thesis aims to develop efficient imaging techniques for fast CMR examinations by combining T_1 mapping and functional imaging, the use of advanced reconstruction techniques and the integration of cardiac motion correction techniques. The three main challenges were addressed by the following developments:

1. A multiparametric scan is developed, obtaining information of T_1 relaxation as well as cardiac function from the same raw data without prolonging the acquisition time compared with imaging of only one parameter. This yields two different parameter, myocardial viability (T_1) and cardiac function, usually obtained in different scans and thus reduces the overall examination time.
2. A model-based image reconstruction technique for cardiac T_1 mapping is introduced that make use of prior knowledge of T_1 recovery in order to ensure accurate T_1 mapping even from highly undersampled data and thus very short scan time. This approach allows for an increase in spatial resolution and enables T_1 mapping not just of the left ventricle but also of the right ventricle and atria.
3. Cine images are utilized to estimate cardiac motion which is then integrated in cardiac motion corrected T_1 mapping. This allows for highly efficient data use and leads to a further reduction of the scan time while increasing the precision of T_1 mapping.

1.2 Outline

The thesis is divided into nine chapters:

Chapter 2 Anatomy, physiology and cardiomyopathies of the heart are presented and the main principles of functional imaging using CMR are introduced. MRI techniques for myocardial tissue characterization using quantitative T_1 mapping are discussed.

Chapter 3 A highly efficient data acquisition scheme is developed which yields functional information of the heart as well as T_1 maps to reduce the overall examination time for the

1. INTRODUCTION

diagnosis of cardiac diseases. The effect of blood flow and motion of the heart through the imaging plane on T_1 estimation are analyzed in simulations. Parts of this chapter have been published in [J2].

Chapter 4 Based on the acquisition presented in chapter 3, it is shown how cine images as well as T_1 maps can be reconstructed using the same data which reduces the total number of scans needed during an examination. An advanced model-based reconstruction technique is introduced which allows for robust and accurate cardiac T_1 mapping on highly undersampled data from a short 168 ms window of each cardiac phase. In addition to T_1 maps, it is also shown that estimation of functional parameter based on the cine images is as accurate as for conventional cine images. This chapter, except for numerical simulations, has been published as [J2].

Chapter 5 T_1 mapping of thin myocardial walls of atria and the right ventricle is explored, by prolonging the acquisition window used for T_1 mapping and thus the efficiency of the method. Functional images of the data are used to determine the full quiescent phase of the heart instead of using a predefined delay and acquisition window. Using the increased amount of data, a higher spatial resolution is possible and feasibility of T_1 mapping of small structures such as the atria is shown. This chapter has been published as [C4].

Chapter 6 In order to fully utilize the efficient data acquisition of chapter 3, cardiac motion correction is implemented in T_1 mapping. Cardiac motion corrected T_1 mapping is presented which allows a reduction of scan time to 50% while increasing the precision of T_1 mapping by 34%. The changes of the cardiac anatomy during the cardiac cycle can be estimated on the cine images. By correcting for this cardiac motion in T_1 mapping of exactly the same acquisition, T_1 mapping is performed on a window of 80% of the data instead of 15 - 20% as done in chapter 4 and standard techniques without introduction of artifacts because of different breath hold positions. Parts of this chapter have been published in [J1].

Chapter 7 The approaches presented in chapter 4 and 6 are extended to post-contrast T_1 mapping and feasibility is shown in patients. The use of both techniques to detect myocardial fibrosis is explored. Post-contrast T_1 maps are compared to qualitative LGE imaging to confirm focal fibrosis. Motion corrected post-contrast T_1 mapping in patients has been published in [J1].

Chapter 8 Possible future research using the introduced multiparametric acquisition is shown. Combining both techniques (i.e. motion correction and model-based image reconstruction) further boost T_1 mapping by reduction of the scan time to only 2 s for a 2D slice without loss in precision.

Chapter 9 In the final part, a summary and general discussion of the proposed approaches is given, and general conclusions are drawn for the integration of the T_1 mapping techniques in clinical routine.

2

Cardiac MRI

CMR can be used for morphological as well as physiological imaging of the heart. Although CVDs is one of the most common causes of death in the western world, CMR examinations only represent a very small share in the total number of MRI examinations. This is mainly due to the complexity of CMR exams and the impact of physiological motion of the heart. This chapter gives an overview of cardiac morphology and function. State-of-the-art imaging techniques are discussed, with a focus on functional imaging (cine imaging) and myocardial tissue characterization by means of quantitative T_1 mapping.

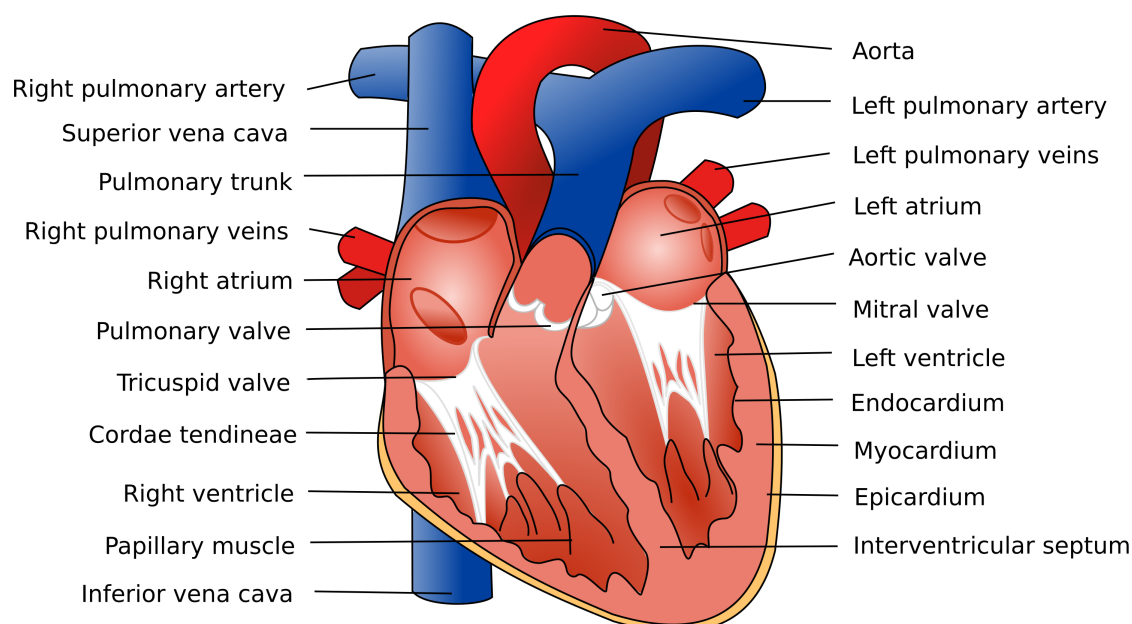


Figure 2.1: Anatomy of the heart, based on [17].

2.1 Cardiac function

The heart consists of four chambers, enable the circulation of blood through the body, which are the superior atria and inferior ventricles (Figure 2.1). Each cardiac cycle consists of two phases: contraction of the ventricles (systole) and the time of relaxation (diastole). The blood is pumped into different circuits from the ventricles (Figure 2.2). The right ventricle (RV) pumps deoxygenated blood into the pulmonary circuit, to the lungs and back to the left atrium (LA) and passes through to the left ventricle (LV). From here, oxygenated blood is transported to body tissue via the systemic circuit, where nutritions and gases are exchanged across the capillaries. Via three veins, the right atrium (RA) receives deoxygenated blood [17, 18].

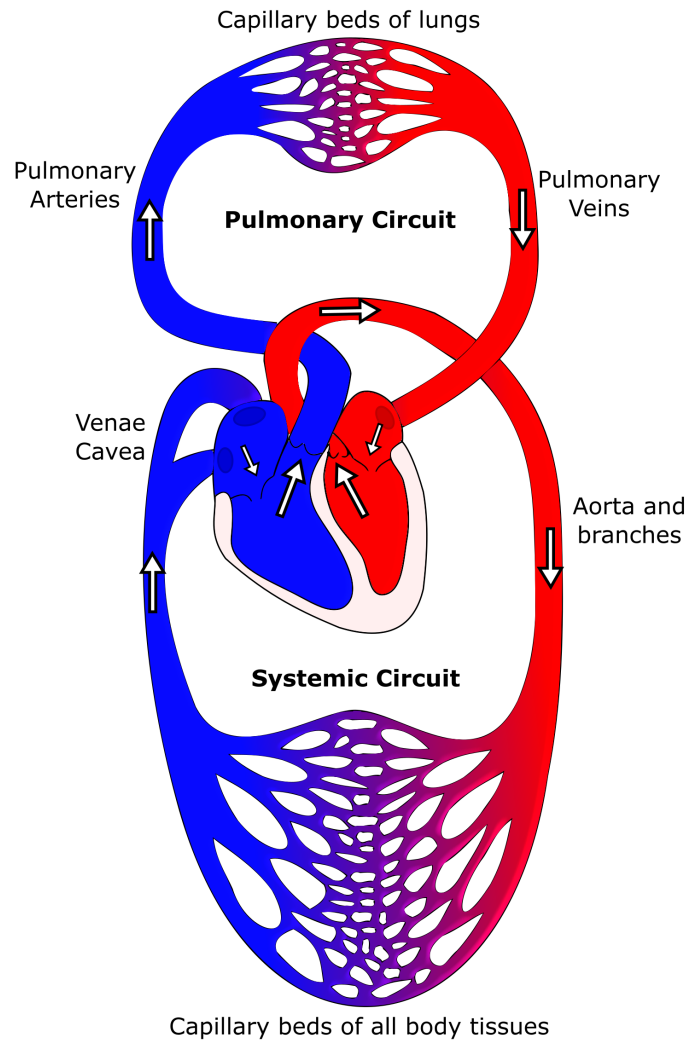


Figure 2.2: Heart as a pump - Blood circulation through the body. Red indicates oxygen-rich blood and blue indicates oxygen-poor blood. Blood is pumped by the LV into the systemic circuit, delivering oxygen and nutritions to the body tissues via the capillary bed. From the RV, blood is flowing into the pulmonary circuit to exchange carbon dioxide and oxygen in the capillaries of the lungs.

The shortest circuit is the coronary circulation, responsible for blood supply of the heart. The circuit originates from the base of the aorta, encircling the heart with two coronary arteries and entering the right atrium via several cardiac veins. Atria and ventricles are

separated by atrioventricular valves, which prevent back flow of blood during ventricular systole. These valves are connected via collagen cords and papillary muscles to the ventricles (Figure 2.1), to prevent the valve flaps to be blown into the atria during systole, because of the high ventricular pressure [17, 18]. The myocardium of the LV is thicker (5 - 6 mm [19]) compared to the RV (3 - 4 mm [20]), because of a five times higher workload to pump blood through the systemic circuit than to the pulmonary circuit. Atrial wall thickness is even smaller than the RV wall, with an averaged thickness of 3 mm [21]. Therefore, imaging of the RV and atria is more challenging, because a higher spatial resolution is needed.

The ability of cardiac contraction is intrinsic and thus independent of the nervous system and the heart rate can be adjusted by the autonomic nervous system. The conduction system consists of autorhythmic cells, initiating action potentials that spread via noncontractile cells in order to depolarize contractile cardiac muscle cells in a coordinated fashion. The action potentials of all conduction cells and contractile cells generate an electric current in the body which varies during the cardiac cycle and can be recorded by an electrocardiogram (ECG) (Figure 2.3).

The cardiac cycle begins with the depolarization of the atria and its contraction (atrial systole), which can be recognized by the P-wave in the ECG in Figure 2.3. Subsequently RV and LV are contracting (ventricular systole), starting with the QRS complex. This ventricular systolic phase lasts about 300 ms and is mainly independent of the heart rate. The atria already relax during ventricular systole and ventricular diastole occur between T-wave and Q-peak. In the following chapters, diastole and systole refer to the ventricular cardiac phases. The ECG is recorded during a CMR examination in order to synchronize data acquisition with the heart beat.

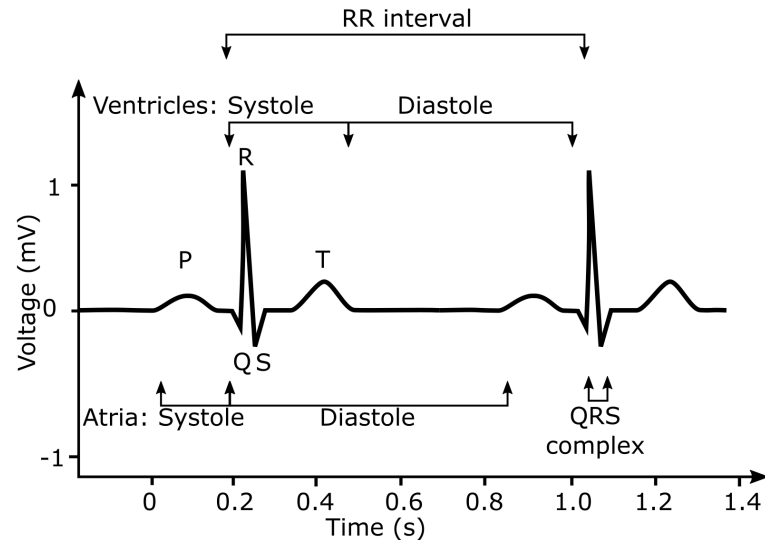


Figure 2.3: Electrocardiogram. The cardiac cycle starts with the depolarization of the atria, triggered by autorhythmic cells (P-wave). The QRS-complex is referred to ventricular depolarization, followed by repolarization of the of the ventricles (T-wave). Systolic and diastolic phases of both atria and ventricles are marked. The RR interval is used during examination to calculate the heart rate and to trigger the data acquisition. Modified from: [22], Figure 11-1, p.124.

2.2 Assessment of cardiac function

To assess the function of the heart, MRI images are obtained at multiple time points during the cardiac cycle. This is commonly referred to as MR cine imaging. In order to resolve the fast contraction and expansion of the heart, 20 - 30 images are obtained to cover the cardiac cycle. Real-time cine imaging is possible, but this limits the achievable spatial and temporal resolution [23]. Instead, data is obtained continuously throughout several cardiac cycles, which usually requires 10-20 cardiac cycles. This continuously obtained data is retrospectively reordered, which is called binning and means that data of all cardiac cycles belonging to one specific cardiac phase is combined before image reconstruction. Binning and reconstructed cine images are shown in Figure 2.4. Binning is performed based on the R-peaks of the recorded ECG, by assigning the delay time between previous R-peak and acquisition time of each acquired line in k-space to the data. During image reconstruction, k-space lines of different cardiac cycles but with the same delay times, are combined, in order to achieve a sufficient coverage of the k-space for each of the 20 - 30 cardiac phases (Figure 2.4). Instead of using an external ECG, information about the different cardiac phases can also be obtained directly from the MR signal, but this is not the clinical standard [24, 25].

In cine imaging, fast gradient echo sequences are used, reaching a steady-state magnetization to provide a constant contrast over the cardiac cycles that is proportional to T_1 (spoiled-gradient echo (GRE)) or the ratio of T_2 and T_1 (balanced steady-state free-precession (bSSFP)). In 2D acquisitions, inflowing blood does not reach a steady-state magnetization and results in high blood signal in comparison to steady-state signal of the myocardium, generating a bright-blood contrast (Figure 2.4). In clinical routine, 8 - 12 slices of cine images are obtained to cover the entire heart.

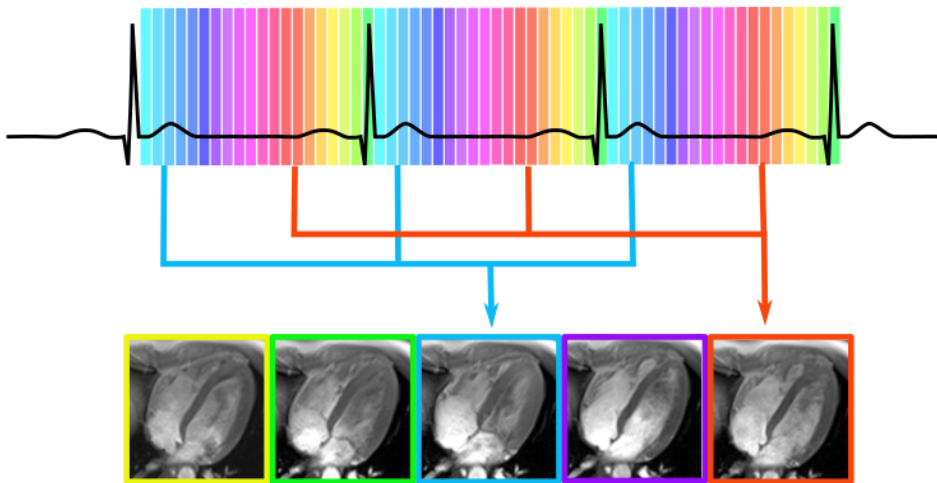


Figure 2.4: Imaging of cardiac function (cine imaging). Usually, data is binned into 20 - 30 cardiac phases for cine imaging using the recorded ECG (colors). Per cardiac phase, data from all 10 - 15 cardiac cycles is combined before image reconstruction (red and blue arrows). Here, five of 20 reconstructed cardiac phases are shown in a four chamber view. Blood appears bright because of unsaturated blood flowing into the slice.

By visual inspection of the images, global and regional cardiac wall motion abnormalities can be detected. Furthermore, quantitative assessment of functional parameters can be determined, such as the mass of the myocardium, end-diastolic volume (EDV) and end-systolic volume (ESV). The volumes can be used to calculate the ejection fraction (EF) of the chambers, which is a measure for pumping efficiency and can be calculated by the blood volume pumped out of the chamber (stroke volume (SV)) with each contraction divided by the EDV. Furthermore, the cardiac output (CO), the pumped blood volume per time is used in clinical routine and can be determined by:

$$CO = SV \times \text{heart rate} \quad (2.1)$$

and the cardiac index, which is the CO related to the body surface area of the individual. The assessment of these functional parameters is applied in chapter 4. In chapter 6, quantitative analysis of cardiac function is shown.

These quantitative functional parameters are important for the detection of various cardiac and systemic diseases with cardiac involvement. Another quantitative functional parameter is blood flow, which can be obtained by other MRI techniques, such as velocity encoded MRI [26].

2.3 Myocardial tissue characterization

Not only the mechanical function of the heart can be measured, but also the viability of the tissue can be assessed by CMR. Healthy myocardium consists of approximately 75% cardiomyocytes and 25% extracellular volume (ECV) (Figure 2.5) [27]. The maintenance of shape, size and function is mainly sustained by the collagen network as part of the extracellular matrix (ECM). Fibrosis is a general pathological process of remodeling of the extracellular space and the extent and distribution of remodeling depends on the underlying pathology.

Different types of fibrosis can be classified [27, 28, 29]. In replacement fibrosis (also known as scarring fibrosis), collagen fibers replace myocytes after cell death or necrosis of myocytes and accumulate in the interstitial space of the myocardium. The imbalance of cardiomyocytes and excessive collagen deposition has multiple consequences for cardiac function, including diastolic dysfunction, arrhythmias and systolic performance, because of reduced contractility of the myocardium and increased stiffness of the tissue. The distribution of myocardial fibrosis can be localized, such as in ischemic cardiomyopathies or myocarditis, or diffuse, such as in inflammatory diseases or toxic cardiomyopathies [27, 29]. Replacement fibrosis is present in the end-stage of many diseases, regardless of the cause of the underlying cardiomyopathy. Also, it is an end-stage result of infiltrative fibrosis or reactive fibrosis. Reactive fibrosis is a causative factor of cardiac dysfunction in metabolic diseases, such as diabetes mellitus and obesity, as well as hypertension and aging. This type of fibrosis is often diffuse and reversible under specific therapy of the disease. If reactive fibrosis is not treated, irreversible replacement fibrosis occurs. Also infiltrative fibrosis can be managed by intervention. Here, insoluble proteins (e.g. amyloidosis) or specific lipids (e.g. Anderson-Fabry disease) are deposited in the interstitium, which could lead to cellular damage if untreated [27, 30]. Therefore, detection of fibrosis is of high interest for therapy planning and monitoring.

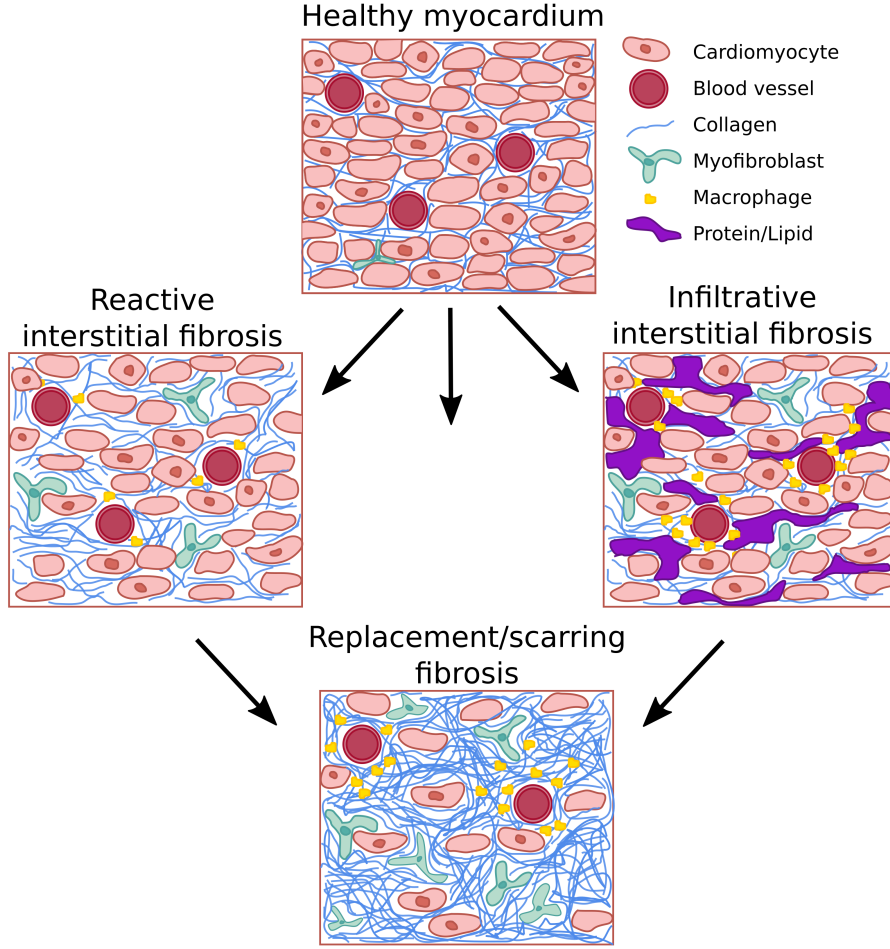


Figure 2.5: Pathology of myocardial fibrosis. Different types of myocardial fibrosis can be classified. The figure is based on [27], [28] and [29].

Endomyocardial biopsy and its histological investigation of the tissue was the gold standard for quantitative assessment of ECV fraction calculation and composition assessment. However, this technique is invasive and imaging is restricted to the endomyocardium. Hence, focal changes at different positions within the myocardium cannot be assessed. Clinical applications of imaging techniques, such as echocardiographic backscatter, nuclear imaging or the use of peripheral collagen biomarkers [31, 32, 33, 34, 35], has remained limited, but CMR has emerged as imaging modality for the assessment of myocardial viability covering the whole heart.

2.4 Assessment of myocardial viability

2.4.1 Contrast enhanced imaging

Nowadays, LGE imaging is the gold standard technique for non-invasive verification of the location and extent of focal fibrosis in ischemic heart diseases [36, 37, 38, 39, 40], which is based on T_1 -shortening of the contrast agent's surrounding tissue and the difference in its distribution within fibrosis and non-fibrotic tissue. An extracellular contrast agent containing a chelate and gadolinium is administered intravenously. Wash-in and wash-out kinetics are delayed in fibrosis,

because of the increased interstitial space in fibrotic tissue. LGE imaging is performed 10 – 30 minutes after contrast administration and at this time point, the contrast agent is already washed out from healthy tissue, but still present in fibrosis. Image acquisition is triggered to one specific cardiac phase to minimize motion artefacts. In order to obtain contrast between healthy and pathological tissue, magnetization is prepared by an inversion radiofrequency (rf)-pulse and images are acquired at zero-crossing of the longitudinal magnetization of healthy tissue. Because of T_1 shortening due to gadolinium deposition, the defect appears bright and non-pathological tissue appears dark (Figure 2.6) [6]. Gray areas in these images belong to a admixture of healthy and fibrotic tissue [41].

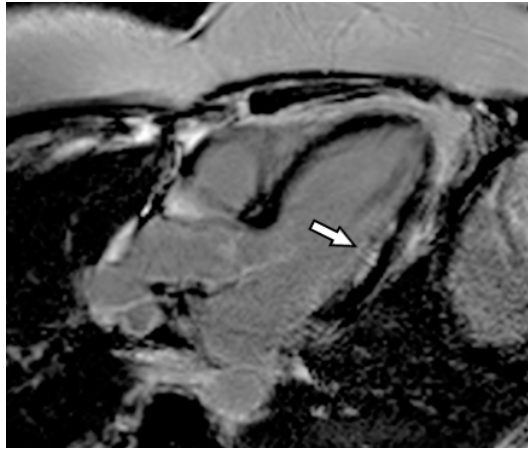


Figure 2.6: Late gadolinium enhancement for visualization of fibrosis. Fibrosis can be detected by the bright signal intensity at the endomyocardial wall of the LV (arrow).

Based on these images, location, size and structure of pathological tissue can be assessed, which is done in chapter 7. This technique is beneficial especially in ischemic heart diseases with focal myocardial damage, because of the excellent contrast between healthy and pathological tissue. For globally diffuse fibrosis, however, discrimination between healthy and pathological tissue cannot be performed. Furthermore, only a qualitative assessment of defects can be performed and the severity of ECM expansion cannot be quantified. Therefore, the development of quantitative CMR techniques is important for the detection of diffuse fibrosis.

2.4.2 Quantitative MRI for myocardial viability

T_1 , T_2 and the effective transverse relaxation (T_2^*) are intrinsic relaxation times describing how the NMR signal changes over time after excitation of the spins. In a static magnetic field, a spin system is at thermal equilibrium, with its net magnetization vector M_0 aligned with the static magnetic field. The spin system can be excited by application of a resonant rf-pulse and subsequently it relaxes back, restoring its equilibrium state. This transition can be described by the three relaxation constants.

Longitudinal T_1 relaxation is also called spin-lattice relaxation because it involves the molecular surrounding of the spins. The T_1 time indicates the duration of the excited spin system returning to thermal equilibrium orientated parallel to the magnetic field (z-axis) with its longitudinal net magnetization. This is done by emitting the absorbed energy to its surrounding, losing its energy.

Transverse T_2 decay refers to spin-spin relaxation. After excitation, neighbouring nuclear spins start to dephase by interactions between the spins. The net magnetic moment dephases in the transverse plane (xy-plane) until its equilibrium is reached, which is complete decoherence of the transverse magnetization and thus a net transverse magnetization of zero. T_2 only includes the effect of neighbouring spins to the decay of transverse magnetization, but after excitation, dephasing also occurs because of inhomogeneities of the static magnetic field B_0 or local differences in magnetic susceptibility. Therefore the spin system relaxes faster, with T_2^* as its relaxation time.

These biophysical parameters are specific for a tissue and its pathophysiological status. Whereas T_2 is sensitive to diseases with increased water content, such as edema [10], it was shown that especially T_1 is assumed to be sensitive to fibrotic changes of the myocardium [10]. Therefore, estimation of the exact T_1 time provides information of myocardial viability, even in diffuse diseases, because no contrast to healthy tissue is needed. Native T_1 times are sensitive to intracellular and extracellular changes, whereas post-contrast T_1 times are mainly affected by extracellular pathologies. However, post-contrast T_1 times depend on interindividual factors, such as renal function, hematocrit, time point of measurement, type of the contrast agent at the applied dose of the contrast agent [36]. Consequently, post-contrast T_1 times vary per measurement and thus these T_1 times alone are not sufficient for diagnosis of diffuse pathologies.

Native and post-contrast T_1 times can be used to calculate the ECV (2.2), which is a direct marker for the extent of myocardial fibrosis [42, 43] and has prognostic value [44]. It presents the physiology directly and because the ratio is taken between post-contrast T_1 times and native T_1 times, intraindividual factors can be partly excluded.

$$ECV = (1 - hematocrit) \frac{1/T_{1,LGE,myo} - 1/T_{1,native,myo}}{1/T_{1,LGE,blood} - 1/T_{1,native,blood}} \quad (2.2)$$

Despite the promising medical use, T_1 mapping is not yet used in most clinical institutions. In the following sections, main principles of T_1 measurements and cardiac T_1 mapping are discussed in more detail.

2.4.3 T_1 mapping principles

M_z describes the z-component of the net magnetization vector M . At thermal equilibrium, M lies along the direction of the magnetic field, with $M_z = M_0$. The net magnetization can be perturbed by exposing the spins to a resonant rf pulse and T_1 describes how the longitudinal magnetization returns to M_0 (Figure 2.7).

The relaxation process of M_z can be expressed by:

$$\frac{dM_z}{dt} = \frac{M_0 - M_z}{T_1} \quad (2.3)$$

and M_z can be calculated by:

$$M_z(t) = M_0 + (M_z(t_0) - M_0)e^{-t/T_1}, \quad (2.4)$$

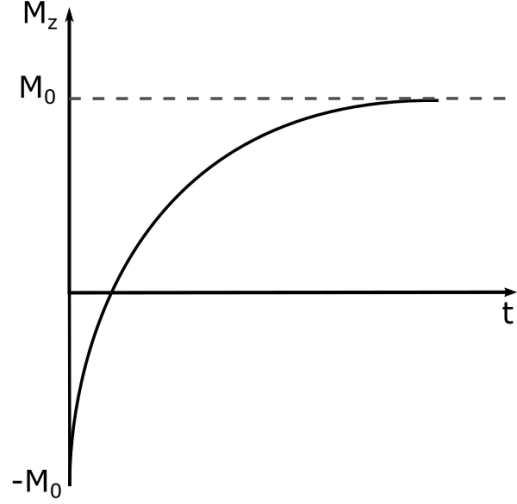


Figure 2.7: Recovery of longitudinal magnetization after application of an inversion rf-pulse.

where $M_z(t_0)$ describes M_z immediately after an excitation rf-pulse. After applying an inversion rf-pulse, the starting magnetization $M_z(t_0)$ is equal to $-M_0$ and thus, the magnetization recovers by

$$M_z(t) = M_0(1 - 2e^{-t/T_1}). \quad (2.5)$$

The T_1 time can be estimated by measuring the magnetization at different inversion times (TIs), the time between a magnetization preparation and data acquisition, and eventually by mathematical fitting of the data points to its physical model 2.4. The most accurate method for TI image acquisition is to perform a series of independent single-point inversion-recovery measurements at different TIs. A long repetition time (TR) between preparation is necessary for full recovery. Consequently, this technique is in general too time consuming for clinical use.

If more data is acquired during one TR cycle, the recovery curve will be disrupted, and the model has to be adapted to the acquisition. One example is the continuous acquisition introduced by Look and Locker [45], where data is sampled using a continuous train of GRE pulses using a constant flip angle. Here, a transient magnetization is reached instead of M_0 (Figure 2.8) and the model is dependent on the flip angle, T_2 influences, magnetization transfer effects and B_0 inhomogeneities, which has to be taken into account during data fitting. More details on this signal behaviour are given in chapter 3, section 3.2.1.

In cardiac applications, T_1 mapping is extremely challenging because of respiratory and cardiac motion limiting the acquisition time. Therefore, T_1 mapping techniques especially for the heart has to be invented.

2.4.4 Cardiac T_1 mapping techniques and challenges

Cardiac T_1 mapping has to deal with respiratory and cardiac motion. The total scan time is usually fixed to one 10 - 20 s breath hold to minimize respiratory motion artefacts. Furthermore, cardiac motion leads to differences in motion states between qualitative TI images. Therefore, most cardiac T_1 mapping techniques utilize cardiac triggering to one specific cardiac phase, which further limits the amount of data acquired.

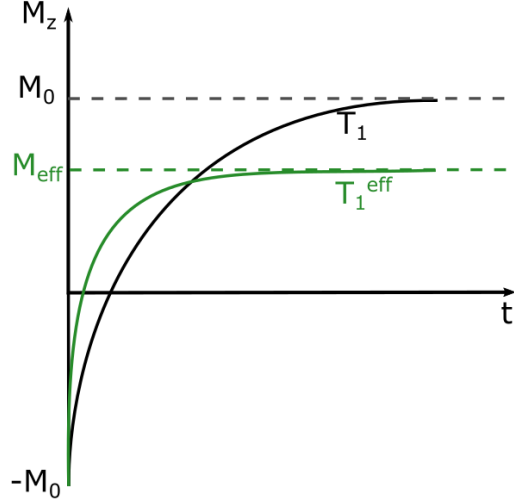


Figure 2.8: Recovery of Look-Locker acquisition (green) compared to recovery without Look-Locker (black). Longitudinal magnetization recovers to an effective M_0 , M_{eff} , that is smaller than M_0 and the effective T_1 is shorter than in free recovery.

One of the first cardiac T_1 mapping approaches was the modified Look-Locker inversion recovery (MOLLI) technique [46]. The acquisition scheme is illustrated in Figure 2.9. Different implementations exist, but all contain the following steps: After inversion of the spins, one image is acquired per 3 - 5 cardiac cycles in a window of 150 - 300 ms during diastole, followed by cardiac cycles where image acquisition is paused for recovery of M_z to M_0 . This is repeated one or two times. The first implementation had the scheme 3(3)3(3)5, where the numbers correspond to the number of cycles with data acquisitions and in brackets, the number of cycles for recovery. Subsequently, TI images were reordered by its TI and fitted to the Look-Locker model.

Disadvantages are heart rate dependence of estimated T_1 times and imperfections of T_1 estimation. These imperfections arise from a simplified model for fitting. Data acquisition is triggered, but data points are fitted to a continuous Look-Locker model, which does not reflect the acquisition, leading to incorrect T_1 estimation. Additionally, incomplete recovery is not taken into account. During the cardiac cycles without data acquisition, longitudinal magnetization is recovering to M_0 (Figure 2.9). However, if this period is not long enough, recovery is incomplete and after the next inversion, $-M_0$ is not reached. This effect is dependent on the heart rate, because the higher the heart rate, the shorter is the recovery period and the higher the error in T_1 estimation. Other commonly used schemes are 5(3)3, 5(1)1(1)1, that is also called shMOLLI, and 4(1)3(1)2 for post-contrast T_1 mapping. In 5(3)3 MOLLI, the impact of the heart rate on T_1 is smaller compared to 3(3)3(3)5 MOLLI, because of the use of correction factors, but triggered data is still fitted to the Look-Locker model. Nevertheless, 3(3)3(3)5 and 5(3)3 MOLLI are the most common cardiac T_1 mapping technique in clinical studies, because of its robustness and high precision.

In contrast to MOLLI, saturation-recovery single-shot acquisition (SASHA) uses saturation pulses instead of inversion pulses, that eliminate the influence of incomplete recovery of longitudinal magnetization on T_1 mapping for a more accurate T_1 estimation [47]. However, only half of the dynamic range is used, resulting in a lower precision of estimated T_1 maps.

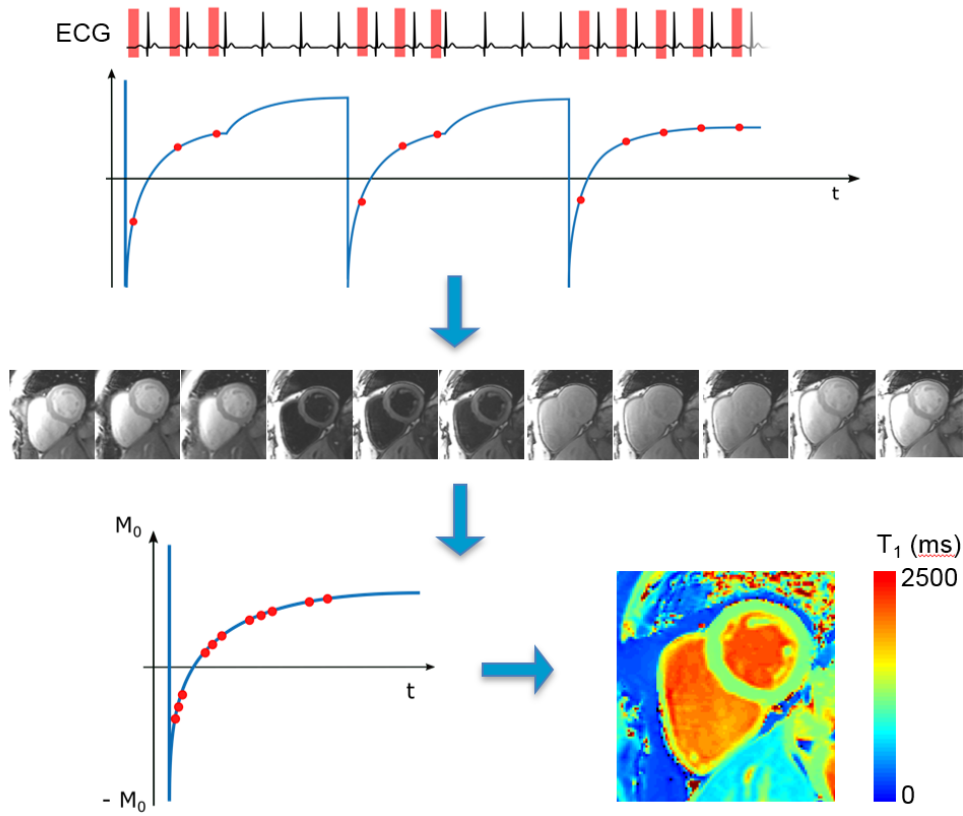


Figure 2.9: T_1 mapping approach using 3(3)3(3)5 MOLLI. After inversion of the spins, one fully sampled image is acquired per three cardiac cycles in a window of 150 - 300 ms during diastole, followed by three cardiac cycles where image acquisition is paused for recovery of M_z to M_0 . This is repeated twice, with five acquired images after the third inversion. After acquisition, images are reordered based in the TIs and image intensities are voxel-wise fitted to a Look-Locker model of the longitudinal magnetization.

2. CARDIAC MRI

T_1 times of healthy tissue using SASHA and MOLLI differ (Table 2.1), so obtained T_1 cannot be compared between studies using MOLLI and SASHA, because normal ranges of healthy myocardium does depend on the technique. This is a main limitation for the use of T_1 mapping in clinical routine. Therefore, the development of new cardiac T_1 mapping techniques is an active field of research, aiming to improve accuracy, precision, robustness, scan time and spatial resolution of T_1 maps.

	1.5 T		3 T	
	MOLLI	SASHA	MOLLI	SASHA
T_1 Native myocardium (ms)	950	1174	1052	1523
T_1 Native blood (ms)	1551	1655	1736	1919
T_1 post-contrast myocardium (ms)	415	720	421	722

Table 2.1: Literature T_1 times for MOLLI and SASHA. T_1 times obtained by SASHA are longer compared to MOLLI. Please note that these values only give a rough estimate of measured in vivo T_1 times. T_1 times also differ between studies. Values are based on results presented in [48], [47] and [15].

To benefit from advantages of saturation as well as inversion recovery schemes, combinations of both techniques were investigated, such as saturation-pulse prepared heart-rate independent inversion-recovery (SAPPHIRE) [49], resulting in heart rate invariant T_1 times. For increased robustness against heart rate variabilities and reduction of partial volume effects, MOLLI and SAPPHIRE were acquired during systole [50, 51, 52], but spatial resolution and scan time stayed the same as in diastolic T_1 mapping. Fitting to Bloch equations instead of a simplified model improved accuracy of T_1 estimation, but spatial resolution and scan time was not improved [53, 54].

Techniques for the correction of residual respiratory motion between TI images were developed for incomplete breath holds with improved detection of myocardial borders in T_1 maps [55, 56, 57] and free breathing approaches were investigated to increase acquisition time without reduction of patient comfort [58, 59]. Using advanced acquisition and/or image reconstruction techniques, first multi-slice and three-dimensional (3D) approaches, covering the entire ventricles, were introduced [60, 61, 62, 63, 64]. In these approaches, the total scan time for a clinical examination was reduced, because less breath holds were necessary for imaging of the whole ventricles.

Recently, T_1 mapping techniques combine non-Cartesian image acquisitions, such as radial or spiral read outs, and advanced image reconstruction techniques, such as low-rank reconstruction and compressed sensing, to deal with highly undersampled data, and a model based on the Bloch equations was used for T_1 estimation [53, 65, 66].

Furthermore, it has been shown that fingerprinting is promising for fast quantitative imaging in the brain [67] and feasibility was shown for its cardiac application [68, 69], obtaining an additional T_2 map. However, due to cardiac motion, cardiac triggering was needed and total scan time was comparable to standard 3(3)3(3)5 MOLLI imaging. Furthermore, T_1 and T_2 times differ from acquisitions obtaining just one quantitative parameter [69].

In clinical routine, T_1 mapping is usually only carried out for the LV. Due the thinner myocardial walls of the other chambers, a higher spatial resolution would be needed, which is technically not yet feasible in a single breath hold. A first approach for high-resolution cardiac

T_1 mapping was investigated, suitable for mapping of the RV, but with a severe prolonged total scan time of 157 s. [70].

One of the main limitations of all of the mentioned approaches is the loss of information about cardiac function (cine imaging). The information is present during the scan time, but not acquired and thus lost due to triggering or gating of the data to one specific cardiac phase. This results in a very low scan efficiency. First proposals for the combination of functional and quantitative imaging were presented, such as TOPAZ, SALLI, multitasking or a 3D free-running method [71, 72, 73, 74], but these approaches suffer from reduced spatial resolution or prolonged acquisition times. For cine imaging, a constant contrast is required for all cardiac phases (section 2.2), whereas in T_1 mapping, different contrasts have to be obtained in order to be able to fit T_1 . Therefore, a suitable acquisition scheme has to be investigated including continuous data acquisition as well as preparation pulses to achieve both requirements and be able to carry out functional imaging and T_1 mapping in one scan. The next chapter discusses a novel acquisition scheme to extend the Look-Locker acquisition scheme to allow for T_1 mapping as well as cine imaging from the same data while ensuring high spatial resolution and clinically feasible scan times.

3

Continuous Acquisition for cardiac T_1 Mapping

3.1 Introduction

The main aim of this PhD project was to combine quantitative imaging and functional imaging for cardiac applications. Continuous data acquisition is needed in order to capture cardiac motion. In T_1 mapping approaches of the brain, it has been shown that T_1 can be quantified by continuous data acquisition following one inversion or saturation preparation pulse [75, 76, 77]. In these approaches, multiple qualitative images at different time points after the preparation pulse were reconstructed from all acquired data, leading to good coverage of the relaxation curve. As already shown in chapter 2, due to cardiac motion, data segmentation is needed for cardiac T_1 mapping to eliminate cardiac motion artefacts, which limits the coverage of the relaxation curve of longitudinal magnetization.

Furthermore, physiological motion has to be considered in T_1 mapping using continuous data acquisition. The myocardium is moving inside and through the imaging plane because of longitudinal motion of the heart. Atrial and ventricular blood is flowing throughout the acquisition. Both effects have an impact on the continuous relaxation curve and thus on T_1 quantification. Therefore, its influence must be studied.

The aim of this chapter was to investigate a suitable 2D data acquisition scheme for simultaneous cine imaging and cardiac T_1 mapping. For this, continuous data acquisition was optimized for cardiac T_1 mapping and the influence of physiological challenges on the accuracy of T_1 quantification was evaluated in numerical simulations.

3.2 Methods

3.2.1 Model function of longitudinal magnetization

The longitudinal magnetization M_z can be described by equation 2.4. This behaviour is only valid for free recovery and it changes if data acquisition is performed. In the following chapters a spoiled-GRE acquisition is used which can be described by the signal model introduced by Look and Locker [45]. During this acquisition, a series of rf-pulses is applied with low flip angles and a short TR between two consecutive rf-excitations. Each gradient echo with flip angle α changes the longitudinal magnetization from M_z to $M_z \cos(\alpha)$ (Figure 2.8). Due to this constant loss of magnetization caused by each excitation pulse, the longitudinal magnetization recovers with a shorter apparent relaxation time T_1^{eff} compared to T_1 and can be described by:

$$T_1^{eff} = [1/T_1 - (1/TR) \ln(\cos(\alpha))]^{-1} \quad (3.1)$$

and thus, T_1^{eff} is dependent on T_1 , TR and the flip angle α . The correction in T_1 for continuous acquisition is also called Look-Locker correction [78].

Due to the continuous excitation, the spin-density converges to M_0^{eff} instead of M_0 that is smaller than M_0 (Figure 2.8) and according to Deichmann and Haase [78], M_0^{eff} can be described as:

$$M_0^{eff} = M_0(1 - e^{-TR/T_1})(1 - e^{-TR/T_1^{eff}})^{-1}. \quad (3.2)$$

For the spoiled-GRE acquisition, $TR \ll T_1$ and $TR \ll T_1^{eff}$, thus the equation can be simplified to:

$$M_0^{eff} = M_0 T_1^{eff} T_1^{-1}. \quad (3.3)$$

The relaxation process of the longitudinal magnetization after application of an inversion rf-pulse can therefore be described by M_0 , M_0^{eff} and T_1^{eff}

$$M_z(t) = M_0^{eff} - (M_0 + M_0^{eff})e^{-t/T_1^{eff}}, \quad (3.4)$$

which is related to T_1 , TR, α and M_0 . TR is known and therefore, a three-parameter fit was applied, obtaining T_1 , α and M_0 during data fitting throughout this thesis. For reference measurements applied in this thesis, inversion recovery (IR)-spin echo (SE) sequences were used and a two-parameter fit was applied, obtaining T_1 and M_0 , because rf-pulses were not applied continuously and the signal follows the model described by equation 2.5. Therefore, fitting of α was not needed.

For the data acquisition used throughout the following chapters, not just one but multiple inversion pulses, applied at constant time intervals T_{ic} , are used (Figure 3.1). The above described IR Look-Locker concept can be further extended for multiple inversions applied at constant time intervals T_{ic} . Right before an inversion the longitudinal magnetization is given by M^+ . Immediately after the inversion, the longitudinal magnetization is $-M^+$, with

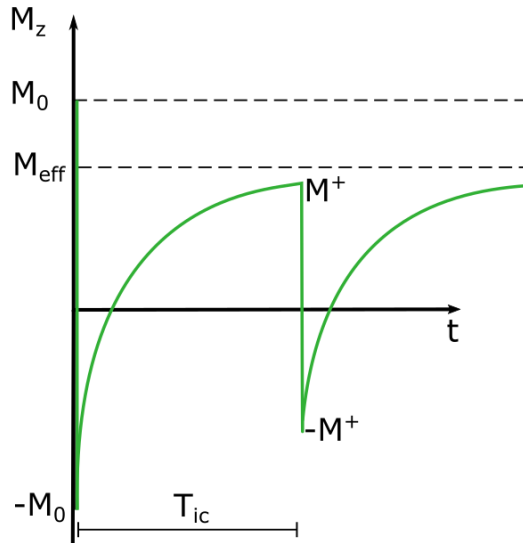


Figure 3.1: Longitudinal relaxation curve applying multiple inversions. Inversion pulses were applied at constant intervals (T_{ic}). The longitudinal magnetization reaches M^+ right before the second inversion. Therefore, the longitudinal magnetization is flipped to $-M^+$ by the second inversion pulse instead of $-M_0$.

the assumption of an inversion efficiency of 1. The relaxation after the j 's inversion can be described as

$$M_z(t) = M_0^{eff} - (M_j^+ + M_0^{eff})e^{-(t-(j-1)T_{ic})/T_1^{eff}}. \quad (3.5)$$

In our studies, the T_2 relaxation can be neglected since the echo time is short. The model is valid for $TR \ll T_1^{eff}$ and small α .

3.2.2 Optimization of data acquisition for cardiac T_1 mapping

For data acquisition, a spoiled-GRE read out with low flip angle [79] was selected. This acquisition is less susceptible to B_0 inhomogeneities compared to a bSSFP read out, although SNR is lower. To obtain the highest possible signal intensity for this acquisition, the Ernst angle (α_E) was calculated for a given TR and T_1 time by the equation [80]:

$$\alpha_E = \arccos(e^{-TR/T_1}). \quad (3.6)$$

The minimal TR is determined by the spatial resolution. Thus, the TR of the highest and lowest spatial resolution of the in vivo and phantom measurements were used, which were 5.3 ms and 4.5 ms for in-plane resolutions of $1.0 \times 1.0 \text{ mm}^2$ and $2.0 \times 2.0 \text{ mm}^2$, respectively. T_1 times were chosen between 300 ms and 1800 ms, to cover a wide range of tissue T_1 times obtained in cardiac imaging.

Only k-space lines corresponding to one specific cardiac phase were selected. For this, in each cardiac cycle, data with a specific delay time after the R-peak was used, which is shown in Figure 3.2. Consequently, the relaxation curve is not well covered, because most images were obtained within steady state magnetization. Therefore, data acquisition was extended for multiple inversions.

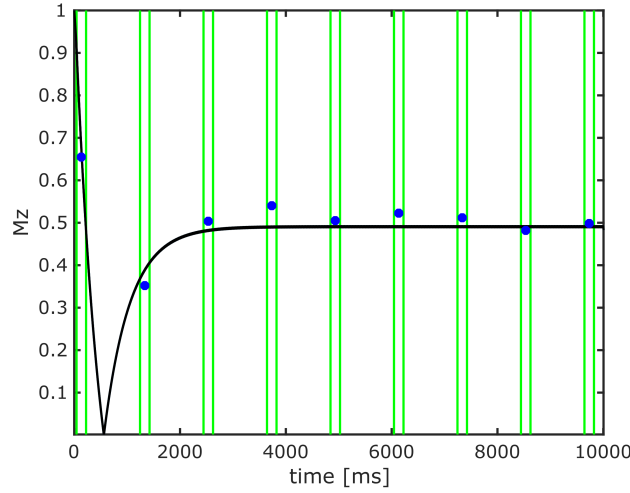


Figure 3.2: Relaxation curve and data selection in cardiac T_1 mapping. Relaxation curve of longitudinal relaxation after an inversion during continuous acquisition (black). Per cardiac cycle, one cardiac phase with a specific window length was selected (here 168 ms, green area). Thus, per cardiac cycle, only one data point was obtained for fitting (blue). This limits the coverage of the relaxation curve, especially immediately after inversion, with largest changes in magnetization (between 0 and 2000 ms).

To determine the best interval between inversions (T_{ic}) for cardiac T_1 mapping, a one-dimensional (1D) simulation was performed. Signal curves with 22 T_{ic} times between 1000 ms and 10000 ms and the following acquisition parameter were simulated: flip angle: 6° , TR: 5.3 ms, acquisition time: 10 s. Every simulation was performed with three different T_1 times important for cardiac imaging (fat: 300 ms, myocardium: 1000 ms and blood: 1500 ms, see table) and six different heart rates between 50 and 100 beats per minute (bpm). Gaussian noise was added to obtain a SNR of 16 for signal of steady state magnetization for a T_1 time of 1000 ms and T_1 was fitted by the three-parameter fit to the signal model 3.5 obtaining T_1 , M_0 and the flip angle.

For each combination of T_{ic} , heart rate and T_1 , the simulation was repeated 600 times and the average T_1 time and standard deviation (STD) of T_1 times were determined. The root mean square (RMS) error of the obtained T_1 times as well as the RMS of the STD across all heart rates was calculated for each combination of T_{ic} and T_1 . Furthermore, the RMS was determined across all heart rates and all T_1 times for each T_{ic} .

3.2.3 Influence of cardiac motion on T_1 mapping accuracy

This section was published in [J2].

Cardiac motion results in through-plane motion of the heart in 2D imaging during systole. The maximum longitudinal motion of the ventricles is about 10 mm [81], reached within a 300 ms long systolic phase, independent of the heart rate. A typical slice thickness for T_1 mapping is about 8 mm, so it was assumed that the ventricles were moved out of the acquired short axis (SAX) slice completely for half of the systolic phase (i.e. 150 ms). To investigate the effect of through-plane motion on T_1 mapping parameters, numerical simulations for diastolic

and systolic T_1 mapping within a single voxel were performed by extending our model by systolic and diastolic cardiac phases.

The model function 3.5 assumes continuous excitation of spins within the imaging plane. If the myocardium is moved out of the imaging plane, it is not affected anymore by the rf-excitation, changing the spin history. This is not captured by the model function which assumes continuous rf-excitation for all spins. Thus, through plane motion could cause errors in T_1 estimation.

In this simplified model, only two states were simulated, the voxel was completely outside of the measured slice or completely inside the slice for parts of the data acquisition. For the diastolic simulation, the model was adjusted such that the tissue did not experience rf-pulses during the systolic phase of 150 ms in each cardiac cycle. During the remaining 850 ms, rf-pulses were experienced, for a simulated heart rate of 60 bpm. For the systolic T_1 mapping simulation, rf-pulses were only simulated during 150 ms and recovery without rf-pulses was assumed during the remaining period of 850 ms. Data points were simulated for diastole and systole and the following parameters: T_1 : 1300 ms, TR: 4.93 ms, flip angle: 5° , heart rate: 60 bpm and M_0 : 1. Eventually, three-parameter fitting was performed to the signal model 3.5 that is uncorrected for through-plane motion.

3.2.4 Influence of blood inflow on T_1 mapping accuracy

T_1 determination of blood is important for clinical application because it is used for calculation of ECV fraction (chapter 2, equation 2.2). In 2D imaging, blood is flowing through the imaging plane throughout the acquisition. The impact on blood flow on the T_1 estimation is evaluated in this numerical experiment. This is done with two-parameter fitting as well as three-parameter fitting for evaluation of the need to fit the flip angle in cardiac T_1 mapping, because of decreased robustness compared to two-parameter fitting [14]. In two-parameter fitting, the flip angle is assumed to be constant and M_0^{eff} can be calculated based on the nominal flip angle, T_1 and M_0 . However, imperfections, such as the slice profile or flowing blood, could possibly not be absorbed and result in inaccurate T_1 estimation.

Only blood in the imaging plane experience readout pulses, whereas inflowing blood have not experience read out pulses before. Here, magnetization within one voxel was simulated, which was assumed to be a mixture of inflowing blood M_{inflow} and blood within the imaging plane M_{RF} . M_{RF} can be described by equation 3.5. Inversions were applied globally (i.e. non-selective IR pulses were used), so M_{inflow} can be described by the same equation as M_{RF} , but without Look-Locker correction (flip angle = 0°). Eventually, the magnetization within a voxel can be described by

$$M_{mix}(t) = \lambda M_{inflow}(t) + (1 - \lambda) M_{RF}(t), \quad (3.7)$$

where λ is the inflow ratio, which is 0 for no inflow and 1 for 100% inflow.

Data points during acquisition were simulated with the following parameters: TR: 4.93 ms, flip angle: 5° and M_0 : 1 and heart rate: 60 bpm. Blood T_1 is dependent on the hematocrit value [82], so the simulation is performed for T_1 : 1600, 1700, 1800 and 1900 ms. 21 difference values for λ were simulated between 0 and 1. Two different fits were performed. Firstly,

3. CONTINUOUS ACQUISITION FOR CARDIAC T_1 MAPPING

two-parameter fitting was performed to the the signal model to obtain T_1 and M_0 . Here, the flip angle was fixed to the ideal flip angle 5° . Secondly, three-parameter fitting was performed obtaining M_0 , T_1 and the flip angle. For each inflow ratio and T_1 , the error in T_1 and M_0 was calculated.

3.3 Results

3.3.1 Optimization of data acquisition for cardiac T_1 mapping

The highest signal intensity is obtained using the Ernst angle. The Ernst angle depends on the T_1 time (Figure 3.3). In cardiac T_1 maps, a large range of T_1 times is present. Myocardial T_1 times is between 1100 and 1500 ms [46, 47], so a flip angle of about 5° is optimal, independent of the spatial resolution. For fat, a two times higher flip angle would be optimal.

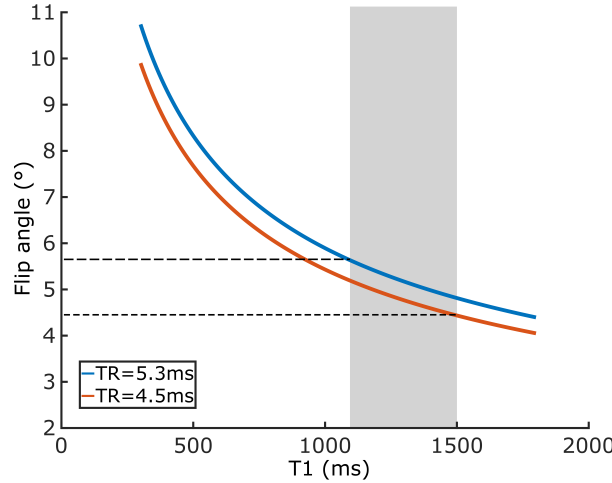


Figure 3.3: Optimization of flip angle using the Ernst angle. The optimal flip angle strongly depends on the T_1 time. For expected myocardial T_1 times between 1100 and 1500 ms (gray region), a flip angle of about 5° provides the best SNR (dashed lines) using a TR between 4.5 and 5.3 ms and thus in-plane spatial resolutions between $1.0 \times 1.0 \text{ mm}^2$ and $2.0 \times 2.0 \text{ mm}^2$ as used in this thesis. For fat (around 300-400 ms), a two times higher flip angle would be optimal, but this is less important for cardiac T_1 mapping

In Figure 3.4, data acquisition including multiple inversions at constant T_{ic} intervals is shown. Here, the relaxation curve is better covered compared to only one inversion (Figure 3.2). The error in T_1 fitting accuracy for different T_{ic} intervals can be found in Figure 3.5. The same trend of T_1 mapping accuracy error was found for all T_1 times. The largest error was found when using a T_{ic} of 10000 ms, which is equal to the Look-Locker concept described by Deichmann et. al [78]. For T_{ic} intervals between 1500 ms and 4000 ms, only small differences were found. Overall, the smallest error in both, T_1 and STD of T_1 fitting, was found for $T_{ic} = 2200$ ms. The large error in T_1 estimation for $T_1 = 300$ ms and $T_{ic} = 3500$ ms resulted from one outlier for only one specific combination of heart rate, T_1 and T_{ic} . For a heart rate of 50 bpm, data points were distributed such that only a small window around the zero-crossing is covered and the steady-state magnetization. T_1 is fitted using the absolute value of the data, so noise is not Gaussian-distributed at the zero-crossing, but shows a Rician distribution, leading to uncertainties in T_1 fitting.

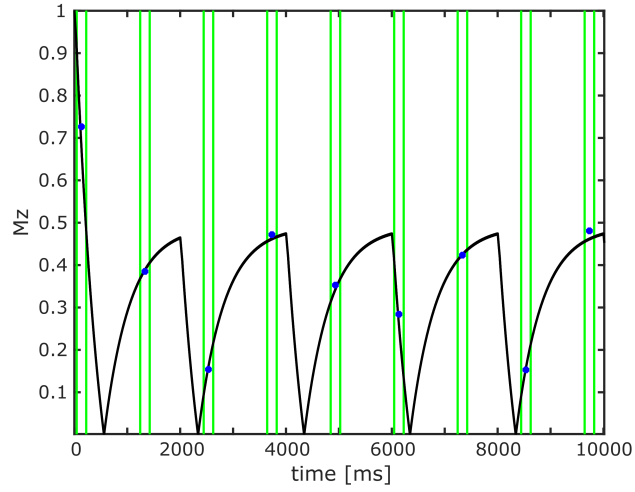


Figure 3.4: Relaxation curve including multiple inversions and data selection in cardiac T_1 mapping. Relaxation curve of longitudinal relaxation during continuous acquisition (black) and selected diastolic data points (blue). Per cardiac cycle, one cardiac phase with a specific window length was selected (here 168 ms, green area). Here, the relaxation curve is better covered compared to only one inversion (Figure 3.2).

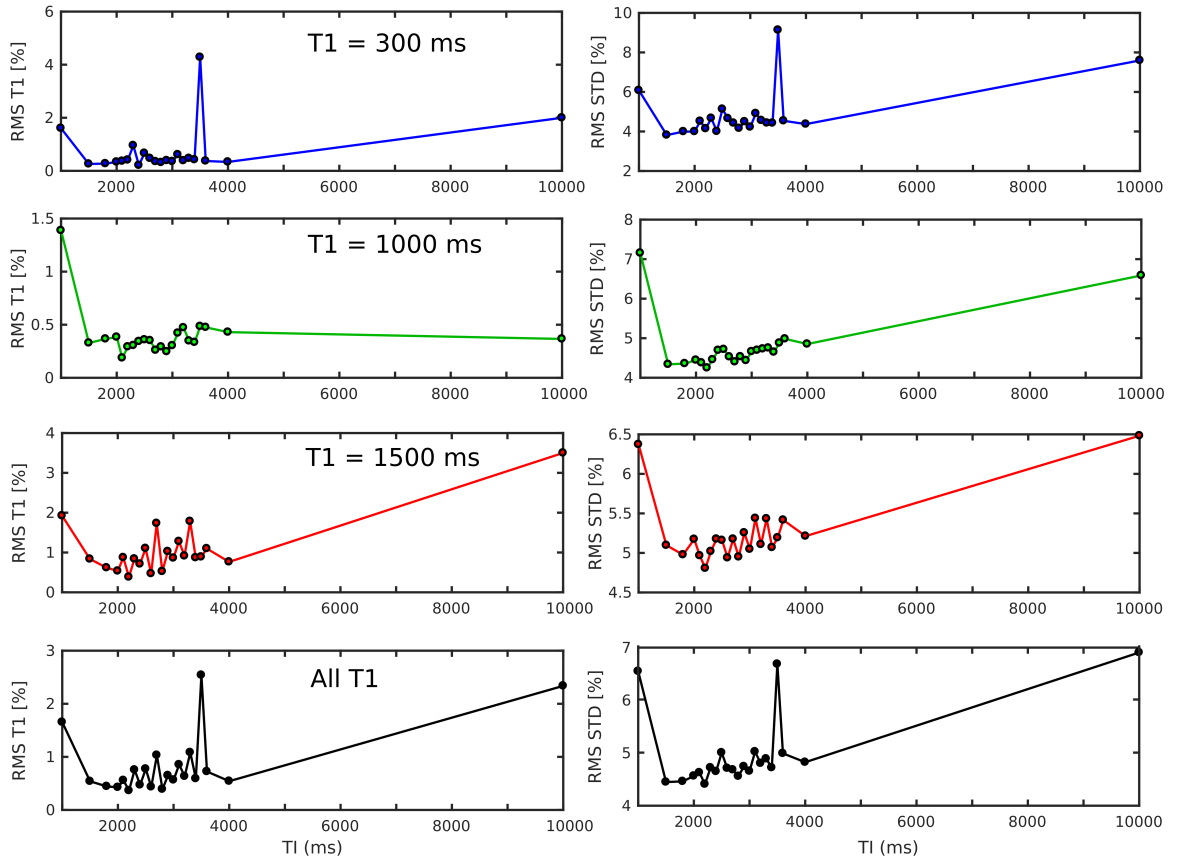


Figure 3.5: T_1 mapping accuracy for different T_{1c} intervals. On the left, the RMS error of T_1 estimation is shown for 300, 1000, 1500 ms and all T_1 times combined. On the right, the RMS of the T_1 STD is shown. The smallest error was found for $T_{1c} = 2200$ ms. A high RMS for $T_1 = 300$ and $T_{1c} = 3500$ resulted from one outlier using a heart rate of 50 bpm.

3. CONTINUOUS ACQUISITION FOR CARDIAC T_1 MAPPING

3.3.2 Influence of cardiac motion on T_1 mapping accuracy

In Figure 3.6, data simulation and result is shown for the investigation of through-plane motion. The simulated recovery curve can be found for diastole (Figure 3.6a) and systole (Figure 3.6b). During the systolic phase, through-plane motion disturbs the recovery curve of continuous acquisition. The fitted recovery curve without correction for through-plane motion can be found in (Figure 3.6c) and (Figure 3.6d).

In diastole, T_1 was estimated as 1287 ms (-1.00 %), M_0 as 0.98 (-2.00%) and the flip angle as 4.51° (-9.76%). In the simulation for systolic T_1 mapping, where rf-pulses were only applied during 150 ms of each cardiac cycle, T_1 was estimated as 1317 ms (+1.29%), M_0 as 1.00 (+0.12%) and the flip angle as 1.86° (-62.83%). Thus, through-plane motion mainly influences the estimated flip angle and has only a small effect on T_1 and M_0 .

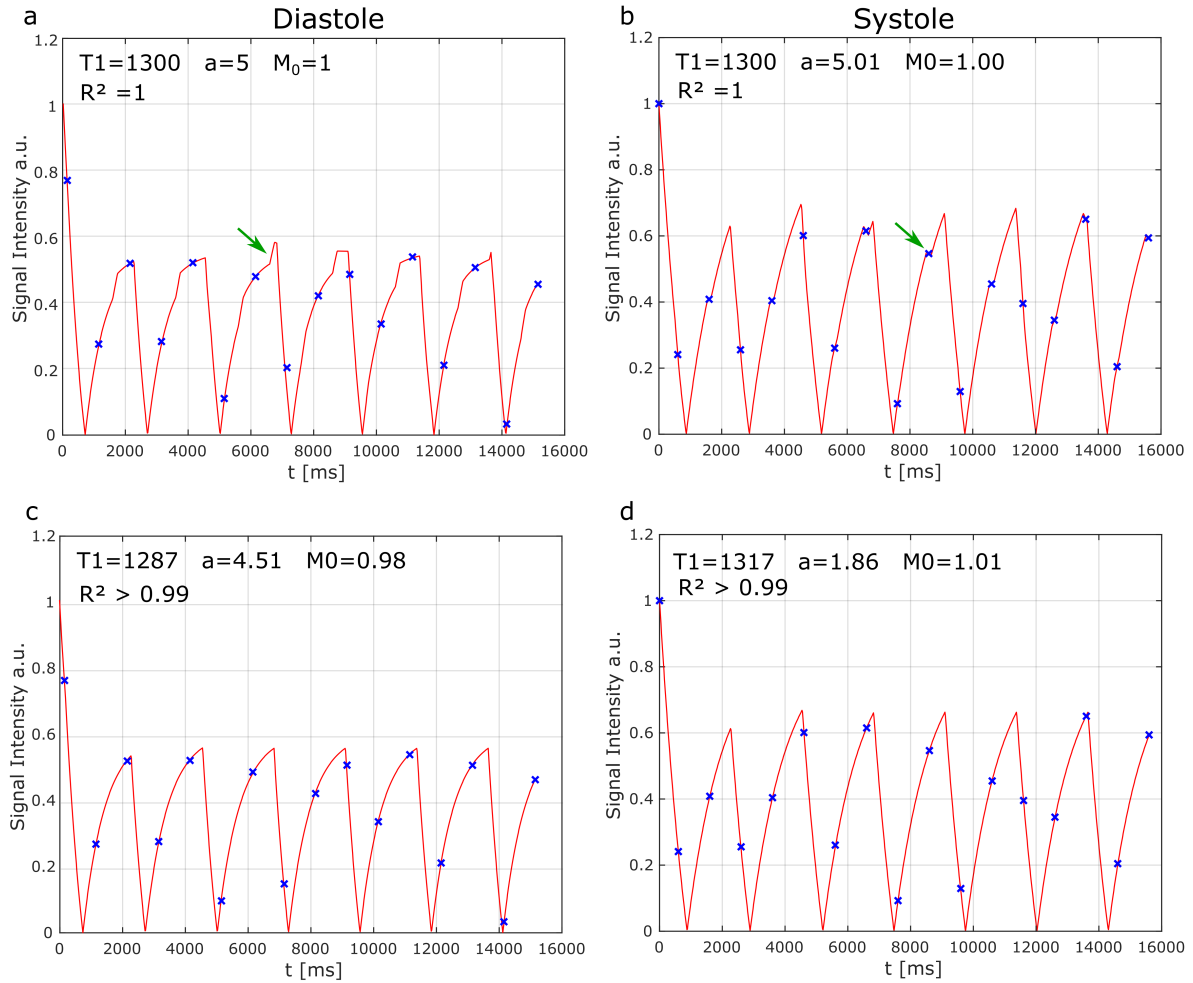


Figure 3.6: Impact of through-plane motion. In the upper row, the simulated recovery curve can be found for diastole (a) and systole (b). The green arrows show the impact of through-plane motion to the recovery curve, resulting in an adapted recovery behaviour during systolic phases of each cardiac cycle. Blue crosses indicate the data points used for fitting. These points were fitted to the recovery curve without correction for through-plane motion (c) and (d). Errors in T_1 estimation were smaller than 1.3%.

3.3.3 Influence of blood inflow on T_1 mapping accuracy

Estimated fit results were dependent on the inflow ratio (Figure 3.7). The three-parameter fit using the applied nominal flip angle during data acquisition, T_1 times and M_0 show large errors for high inflow ratios. The maximal error in T_1 was between 8.1 and 13.3% for T_1 times between 1600 and 1900 ms. In M_0 , errors were between 16.7% and 23.7%. Decreased fit quality can also be seen by the lower coefficient of Determination (R^2) values.

The three-parameter fit showed lower errors in T_1 and M_0 estimation. The maximal error in T_1 was between 2.7 and 3.2% for simulated T_1 times. In M_0 , maximal errors were 0.1%. The flip angle fit compensated for the inflow of blood, which can be seen by a decreasing flip angle for higher inflow. Therefore, the three-parameter fit, including the flip angle in addition to T_1 and M_0 , is beneficial for cardiac T_1 mapping.

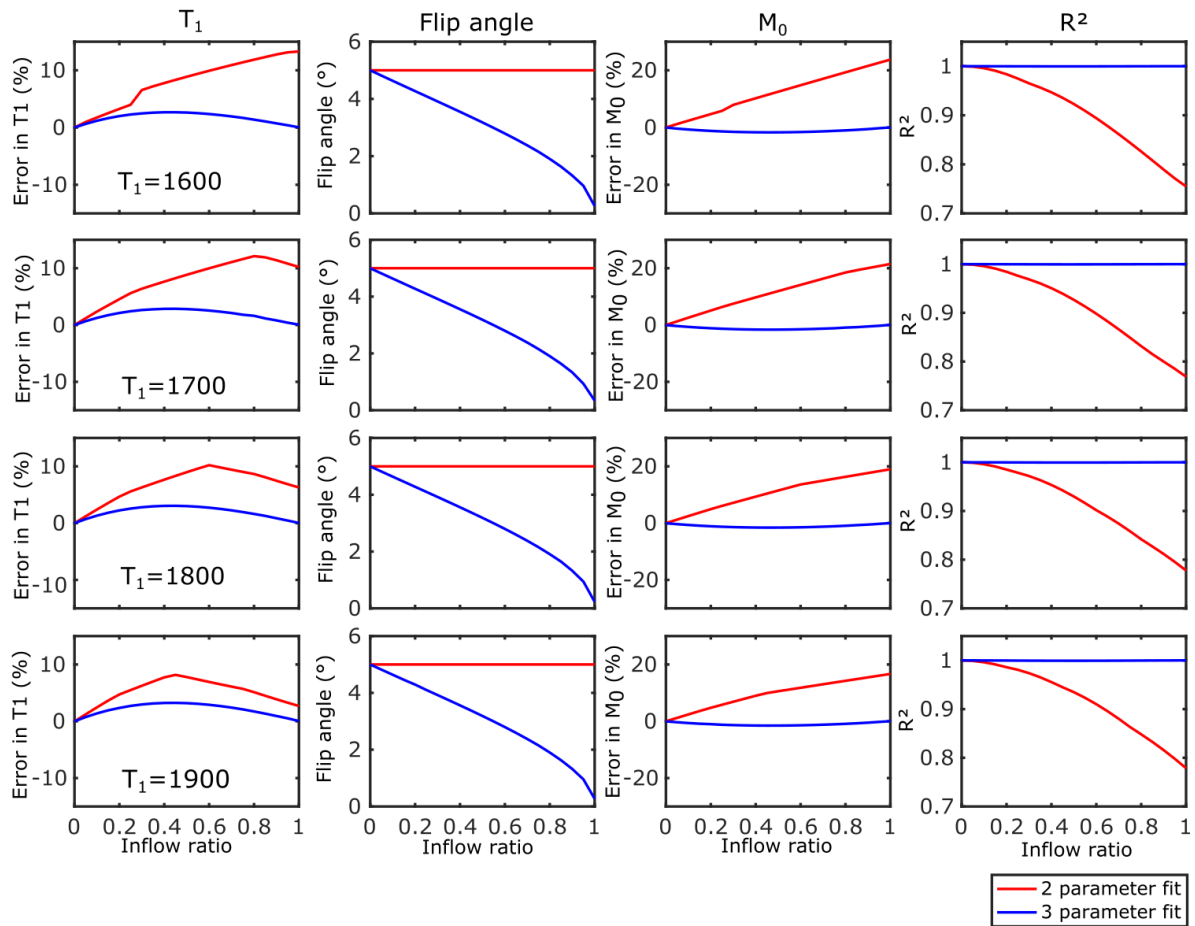


Figure 3.7: Impact of inflowing blood. The three-parameter fit yielded lower errors in T_1 (max. 3.2%) and M_0 compared to the 2-parameter fit, with an error in T_1 of up to 13.3%. The flip angle fit compensates for the inflow of blood.

3.4 Discussion

In numerical simulations, it is shown that T_1 estimation is possible using continuous data acquisition for cardiac applications. The application of multiple inversions during the acquisition improves the T_1 estimation. Through-plane motion and inflow of blood only have a small impact on T_1 accuracy by using a three-parameter fit for T_1 , flip angle and M_0 .

For T_1 fitting, the recovery curve was extended to multiple inversions. The fitting routine takes longer, because of a more complex function, but the extension of the model function has advantages compared to shifting of data points onto an inversion recovery curve with only one inversion, which is done in standard T_1 mapping techniques, such as MOLLI. Right before an inversion, the magnetization is not fully recovered, which is not taken into account in MOLLI. In our approach, however, the full spin history is considered for T_1 fitting, resulting in a more accurate fit.

The T_1 fitting was improved by the application of multiple inversion pulses for a large range of T_1 times, because of better coverage of the recovery curve. The coverage of the relaxation curve still depends on the heart rate. Thus, the optimal implementation would be a T_{ic} interval which is adjusted for each heart rate. However, it was shown that for a wide range of heart rates, the fit was robust using a fixed T_{ic} interval, especially for T_1 times of myocardium.

Saturation recovery (SR) could have been chosen as well instead of IR for T_1 estimation. In IR, the inversion efficiency has to be taken into account, which would be not the case in SR, but IR was chosen because of the higher dynamic range compared to SR [14].

As shown in numerical simulations, through-plane motion has only small impact on the estimated T_1 times. The effective flip angle was reduced which compensates for through-plane motion, with remaining errors in T_1 smaller than 1.3% in diastolic and systolic T_1 mapping. In conventional cardiac T_1 mapping techniques, only two parameters were estimated, assuming an ideal and constant flip angle. Therefore it was investigated if two- or three-parameter fitting is advantageous for cardiac T_1 mapping, wherein blood is flowing through the plane. The inflow of blood increases T_1 values by a maximum of 3.2% using three-parameter fitting. Three-parameter fitting yielded more accurate T_1 estimation than two-parameter fitting. Using two-parameter fitting, M_0 and T_1 were overestimated and the fit quality was decreased for increasing inflow, which can be seen in a reduced R^2 . Therefore, a three-parameter fit should be used for cardiac applications.

However, both simulations have limitations. Through-plane motion was simulated with two motion states only – either the tissue experienced excitation rf-pulses or not. Continuous motion of the myocardium was neglected as well as the Gaussian shaped slice profile. Therefore, the simulations provided only a first estimation of the influence of through-plane motion and inflow of blood on T_1 mapping. Both have only small impact on T_1 estimation using a three-parameter fit and for in vivo experiments, the impact depends on the volunteer and the slice position. Especially in patients with cardiomyopathies, motion is complex and thus through-plane motion is difficult to be described by the exponential fitting model. Therefore, these effects were neglected in T_1 mapping throughout the studies.

3.5 Conclusion

In this chapter, it was shown that T_1 estimation is possible using continuous data acquisition for cardiac applications. The application of multiple inversions during the acquisition improved the T_1 estimation, because of better coverage of the recovery curve for a large range of T_1 times and heart rates. A three-parameter fit for T_1 , flip angle and M_0 was advantageous over a two-parameter fit for T_1 and M_0 only in cardiac T_1 mapping. Therefore, this three-parameter fit is used throughout the thesis. Through-plane motion and inflow of blood could be compensated by the effective flip angle estimation and had only small impact on T_1 estimation (up to 3.2%). Here, only one-dimensional simulations for T_1 estimation were performed, but data acquisition and reconstruction of the data during limited scan time due to breath holding was not yet considered. Furthermore, the main aim of the thesis was to integrate cine reconstruction from the same data for increasing scan efficiency. Therefore, a model-based reconstruction is introduced for 2D- T_1 mapping, dealing with highly undersampled data and cine reconstruction from the same data.

4

Simultaneous T_1 Mapping and Cine imaging using iterative model-based Reconstruction

Parts of this chapter have been presented in [J2]: Becker et al., Simultaneous high-resolution cardiac T_1 mapping and cine imaging using model-based iterative image reconstruction, Magnetic Resonance in Medicine, 2019; vol. 81, pp. 1080–1091, which has been published in final form at <https://doi.org/10.1002/mrm.27474>.

4.1 Introduction

Cardiovascular magnetic resonance provides a range of diagnostic parameters which allow for diagnosis and monitoring of different cardiac diseases and to identify even subtle pathological changes of the heart [4, 2]. Cine imaging is performed for cardiac wall motion abnormalities and to quantify cardiac function [83]. Quantitative native T_1 mapping is becoming an important technique to detect fibrosis and diffuse cardiomyopathies [84, 85, 86]. Commonly, the different diagnostic and prognostic parameters are obtained in separate scans, including multiple breath-holds, leading to long examination times.

In MOLLI and SASHA, the recovery of the longitudinal magnetization is measured, by acquiring one image per cardiac cycle in single shot mode at different TIs after inversion or saturation pulse [46, 87, 47]. In order to perform a robust exponential fit, a number of images over multiple cardiac cycles and different initial delays are applied during a single breath-hold. Therefore, the spatial resolution of these images is strongly limited by time constraints due to cardiac and respiratory motion. To identify small myocardial structures, such as small changes in the myocardium or the myocardial wall of the right ventricle, enhanced spatial resolution would be necessary, but currently, high-resolution T_1 mapping is not possible in a clinically feasible scan time [70].

4. SIMULTANEOUS T_1 MAPPING AND CINE IMAGING USING ITERATIVE MODEL-BASED RECONSTRUCTION

The data acquisition for T_1 mapping is inefficient, since data is obtained during one cardiac phase, e.g. diastole, only. In MOLLI, additional recovery periods of several heart cycles without any data acquisition are required after each preparation pulse to guarantee full recovery of longitudinal magnetization before the application of the next inversion pulse. If the duration of the recovery periods varies, e.g. due to changes in the heart rate, the obtained data does not necessarily follow the assumed exponential signal model which can lead to errors in the T_1 maps [46, 14]. In SASHA, additional rest periods are not required, but the dynamic range of the magnetization recovery is reduced resulting in less precise fit values compared to MOLLI. Another disadvantage of MOLLI and SASHA is the requirement for triggering to diastole, which can lead to artifacts in the T_1 maps due to heart rate variabilities [88].

In order to improve the acquisition efficiency of T_1 mapping approaches, the combination of T_1 mapping and cine imaging has been proposed [72, 71, 73]. Data is acquired continuously during the cardiac cycle and T_1 maps and functional images are reconstructed from the same scan. However, these techniques suffer from prolonged scan times or low spatial resolution.

Model-based image reconstruction techniques have become popular to recover images from incoherently undersampled k-space data. They do not require a complete single-shot image for each time point along the magnetization recovery curve and hence can achieve higher spatial resolution and shorter scan times. Initial results with these techniques have been shown for quantitative brain, liver and spinal cord imaging [89, 76, 90, 77, 91, 92, 93], but not yet for cardiac imaging.

In this study, we present a novel golden-ratio-based radial acquisition technique, that combines high-resolution cardiac T_1 mapping and cine imaging for increased acquisition efficiency. Data acquisition was applied continuously using inversion pulses at fixed time intervals over multiple cardiac cycles during 16 s. Reconstruction of T_1 maps was carried out using an iterative model-based approach of the longitudinal magnetization recovery at different cardiac phases (i.e. diastole and systole). Cine reconstruction with 30 cardiac phases and consistent dark-blood contrast were reconstructed as well. The new method was evaluated in a T_1 phantom and in 10 healthy subjects. T_1 maps and cine images were compared to MOLLI and functional analysis of standard Cartesian cine scans.

4.2 Methods

4.2.1 Data acquisition

The pulse sequence was based on IR with a continuous spoiled gradient echo readout that was modified to a golden-ratio-based radial acquisition (Figure 4.1ab). The golden angle of 111.25° between successive projections allows for flexible reordering of k-space data retrospectively [93, 75], which was used for reconstruction of cine images and T_1 maps (Figure 4.1cd). Multiple nonselective adiabatic inversion pulses were applied at a constant T_{ic} . Data was acquired for a predefined number of seconds.

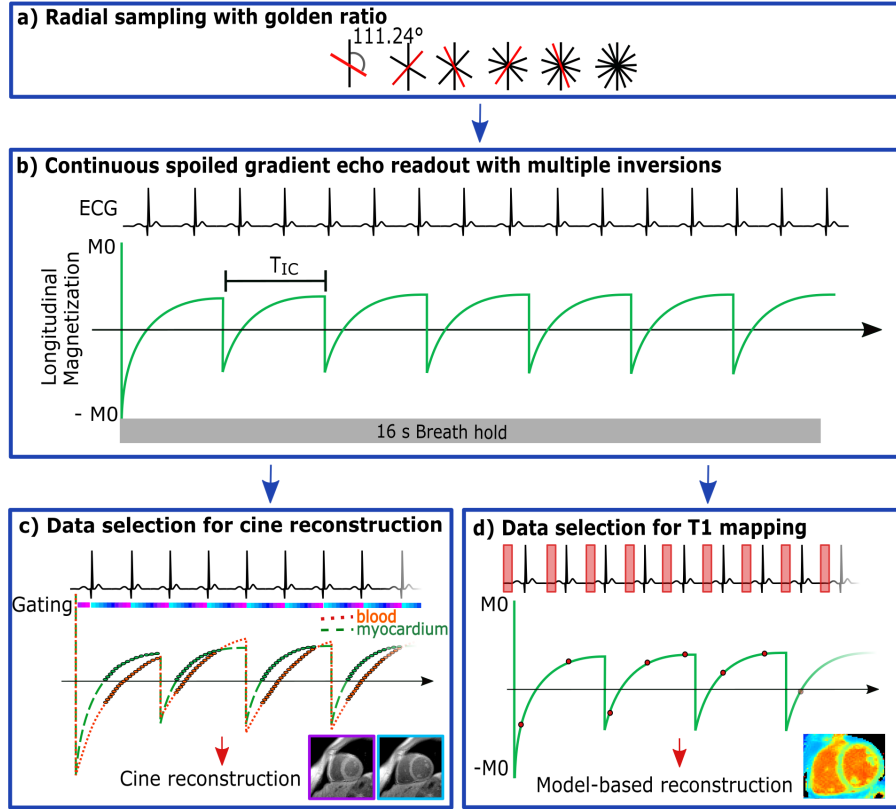


Figure 4.1: Data acquisition and selection. a) Data is acquired with golden-ratio-based radial sampling. b) Scheme of continuous data acquisition. Inversion pulses are applied at T_{ic} . c) For cine reconstruction, k-space data is gated for 30 cardiac phases. Only data with positive signal for healthy myocardium is included (circles). d) For T_1 mapping, data of a specific cardiac phase (e.g. mid-diastole or mid-systole) is selected [J2].

4.2.2 Iterative T_1 reconstruction

T_1 estimation was carried out iteratively during model-based image reconstruction. For this, initial images were reconstructed from resorted data allowing for the calculation of parameters T_1 , M_0 and the flip angle from the image data. The model 3.5 was used to calculate the temporal behavior of the magnetization, from which k-space data of the model was determined and data consistency between the acquired and the model k-space was ensured. The iterative reconstruction technique was first introduced by Tran-Gia et. al for T_1 mapping of the brain using a single saturation pulse [76]. Here we extended this approach to cardiac imaging, by incorporating multiple inversion pulses and extending the used model accordingly. In addition, we added the flip angle as a model parameter in the reconstruction. In particular, the iterative reconstruction consists of the following steps (Figure 4.2):

1. The k-space data was retrospectively gated to select a specific cardiac phase (Figure 4.1d).
2. The selected radial spokes of all n cardiac cycles were interpolated onto n Cartesian grids using self-calibrating GRAPPA operator gridding (GROG) (Figure 4.2a) [94].
3. Coil sensitivities were estimated from all data combined [95].

4. SIMULTANEOUS T_1 MAPPING AND CINE IMAGING USING ITERATIVE MODEL-BASED RECONSTRUCTION

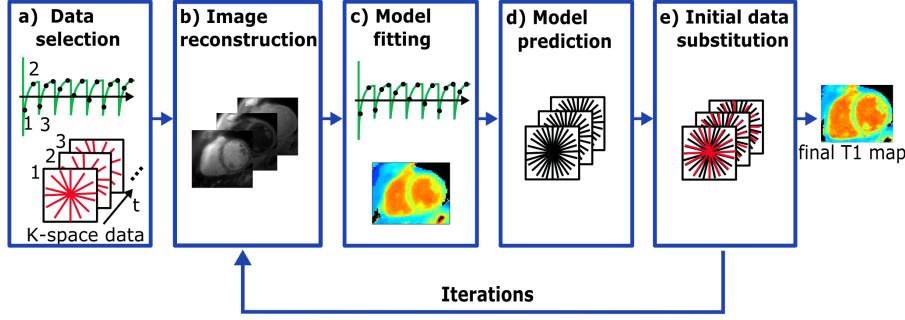


Figure 4.2: Iterative model-based image reconstruction. Data of a specific cardiac phase is selected and T_1 is estimated iteratively for a fixed number of iterations [J2].

4. Images were reconstructed with an inverse fast fourier transformation (FFT). A coil combination was carried out using a weighted sum of squares (Figure 4.2b).
5. The magnitude images with different inversion times were fitted voxel-wise to the magnitude of the described model function 3.5 in section 3.2.1 (Figure 4.2c). A three-parameter nonlinear least-squares fitting was implemented, yielding T_1 , M_0 and the flip angle of each voxel.
6. Based on T_1 , M_0 and the flip angle, for each of the n time points, image intensities were calculated voxel-wise using the model function. The images were multiplied by each coil sensitivity to account for the intensity variations. The resulting images were used to calculate n model k-spaces by applying a FFT (Figure 4.2d).
7. Data consistency was ensured by substitution of the model predictions with the acquired k-space data (Figure 4.2e). No minimization criterion was included in the reconstruction. The consistent k-spaces serve as input for the next iteration.

Steps 4 to 7 were repeated until a stopping criterion was fulfilled. The stopping criterion was set to a fixed number of iterations in our study, for which the change in averaged T_1 times over a region of interest (ROI) in the heart was less than 1 ms. This was fulfilled for the same number of iterations in all volunteers. No spatial or temporal filtering was applied during reconstruction.

4.2.3 Cine reconstruction

Cine images were reconstructed using the same data as for the T_1 mapping but binning the k-space data to different cardiac phases. To ensure a high contrast between blood and myocardium, only those data was used if the signal from myocardium was positive and the magnitude of the myocardial signal is higher than the signal of blood (Figure 4.1c). Since the T_1 time of blood is longer than T_1 of myocardium, the blood signal in the chosen window is smaller and partly negative, resulting in small and partial cancellation of image intensities for blood. Therefore, in the cine images blood appears darker than myocardium, resulting in a dark-blood contrast.

4.2.4 Experiments

All measurements were performed on a 3 T MRI scanner (Verio, Siemens Healthineers, Erlangen). To synchronize data acquisition retrospectively, ECG gating was utilized. Image reconstruction and all data evaluation were carried out offline using MATLAB (The MathWorks, Inc., Natick, USA). Statistical analysis was performed in GraphPad Prism 6.0 (La Jolla, USA) and a p-value less than 0.05 was considered to be significant in all statistical tests.

4.2.5 Numerical simulations

The iterative model-based T_1 mapping algorithm was evaluated in a numerical phantom. Based on the numerical phantoms XCAT and MRXCAT [96, 97], the phantom was extended for T_1 times and proton densities for the heart and surrounding tissues and the phantom was transformed to SAX. 2D data acquisition was simulated using the magnetization description 3.5 and the same parameter as used for the phantom and in vivo measurements: acquisition time: 16 s, T_{ic} : 2276 ms, M_0 : 1.5, flip angle: 5° , TR: 4.93 ms, field of view (FOV): 320×320 mm² and in-plane resolution: 1.3×1.3 mm². Four coils surrounding the chest were simulated. A heart rate of 60 bpm was simulated and 34 diastolic k-space lines were used per cardiac cycle. Data sampling was 2-fold oversampled in radial direction. Iterative T_1 mapping was performed and T_1 times were assessed in a septal ROI and in the blood pool of the LV.

4.2.6 Phantom experiments

Data acquisition

For evaluation of the T_1 fitting accuracy, a commercially available phantom (Eurospin, Diagnostic Sonar LTD, UK) consisting of twelve vials with T_1 times ranging from 315 to 1770 ms was scanned using a 16-channel head coil. A 2D slice was acquired in 16 s (T_{ic} : 2276 ms, flip angle: 5° , echo time (TE): 2.03 ms, TR: 4.93 ms, FOV: 320×320 mm², in-plane resolution: 1.3×1.3 mm², slice thickness: 8 mm and 2-fold oversampling in radial direction).

Reference T_1 times were determined by a Cartesian SE sequence, using an inversion rf-pulse as preparation, with seven TIs (TI: 25 - 4800ms, TE/TR: 12/8000 ms, in-plane resolution: 1.3×1.3 mm², slice thickness: 8.0 mm, FOV: 320×320 mm²). A two-parameter non-linear least squares fitting algorithm was used to determine the reference T_1 times and M_0 .

As T_1 mapping reference, T_1 maps were obtained by a standard 3(3)3(3)5 MOLLI sequence [46] implementation with the following settings: FOV: 360×307 mm², slice thickness: 8.0 mm and in-plane resolution: 2.1×1.4 mm². Post-processing and T_1 fitting were carried out automatically including motion correction and inversion efficacy correction [14].

T_1 reconstruction

The ECG was simulated with heart rates between 50 and 120 bpm to assess the influence of heart rate on the accuracy of the T_1 mapping. Data was retrospectively gated to a simulated mid-diastole and for each heart cycle, 34 radial projections were selected, yielding a nearly optimal uniform distribution in k-space, because of a Fibonacci number of spokes [93]. T_1 maps were reconstructed for eight different heart rates using the above described iterative

4. SIMULTANEOUS T_1 MAPPING AND CINE IMAGING USING ITERATIVE MODEL-BASED RECONSTRUCTION

model-based approach.

Evaluation of T_1 accuracy

T_1 times were averaged within ROIs in each compartment. The accuracy of the novel T_1 mapping approach was assessed by comparing the computed T_1 times to the IR-SE T_1 references using Pearson's linear correlation. The accuracy evaluation was performed for all simulated heart rates. The dependence of the heart rate on T_1 was evaluated by linear correlation in all compartments for the proposed approach and the MOLLI sequence.

4.2.7 In vivo study

Data acquisition

Data was obtained in ten healthy subjects (6 males, aged 31.3 ± 8.4 years). All subjects gave written informed consent before participation, in accordance with the institutions ethical committee. Imaging was performed using a spine coil and a 16-channel anterior coil array. 2D slices were acquired during a 16 s breath-hold with the same parameter as for the phantom experiment. Images were acquired in a four-chamber view (4ChV) and a midventricular SAX of the heart. The SAX acquisition was repeated in eight subjects to assess reproducibility of the proposed approach within the same session and without table repositioning. MOLLI images were acquired in mid-diastole at the same 4ChV and SAX slice positions.

To validate the reconstructed cine images, standard bright blood 2D Cartesian cine scans were acquired as well at the same slice positions. These cine scans were based on a spoiled-GRE sequence with retrospective gating for 30 cardiac phases and the following parameters: FOV: 320×320 mm², in-plane resolution 1.7×1.7 mm², slice thickness: 8.0 mm, TE/TR: 2.48/5.2ms and flip angle: 12°. Cine images were acquired during 12 cardiac cycles.

T_1 reconstruction

T_1 maps were reconstructed for mid-diastole and mid-systole. 34 diastolic and 34 systolic radial spokes were selected per cardiac cycle, resulting in an acquisition window of 167.6 ms (Figure 4.1c). Diastolic T_1 reconstruction was performed with the iterative approach described above. Systolic T_1 reconstruction was applied in the same way, with information of estimated M_0 in diastole used as input for systolic T_1 mapping to improve robustness of the fitting algorithm for systolic M_0 estimation. In two subjects, T_1 maps for 30 cardiac phases were reconstructed, yielding dynamic T_1 maps.

T_1 analysis

In SAX T_1 maps acquired with our method and the MOLLI sequence, T_1 times of the myocardium were measured according to the six mid-ventricular myocardial segments adapted from the American Heart Association [98]. In 4ChV, a mid-ventricular ROI was segmented at the septal intersection of 4ChV and SAX slices. Diastolic T_1 times determined with our approach in all segments were compared to two different T_1 maps. Diastolic T_1 times were compared to T_1 times obtained by MOLLI. Additionally, a second comparison was performed

between diastolic T_1 times and our systolic T_1 times. Therefore, a multiple measure Friedman test with Dunn's multiple comparison correction was used.

For evaluation of inter-subject variability, precision and repeatability, a septal ROI in SAX was chosen. The inter-subject variability of septal T_1 times is given in diastolic images and corresponds to the STD of T_1 over the 10 subjects.

The precision, defined as the STD of T_1 times obtained within the septal ROI in each subject, was compared between MOLLI and our approach and differences in precision were tested by a Wilcoxon rank-sum test.

To test the robustness of the T_1 mapping method, repeatability was assessed by comparing the computed T_1 times of the two repeated SAX acquisitions by a Wilcoxon rank-sum test.

Cine reconstruction

Cine images were reconstructed from the same acquired data in SAX and 4ChV. To exclude negative myocardial data, the mean myocardial T_1 time of all reconstructed T_1 maps were used to determine the zero crossing of the myocardial longitudinal magnetization. Positive myocardial signal was obtained for $1175 < t < T_{ic}$ ms after the first inversion and for $400 < t < 1755$ ms after all other inversions. This can be seen in Figure 4.1c, marked with green and red circles. The k-space data was retrospectively gated and cine images with 30 cardiac phases were reconstructed with a k-t sensitivity encoding (k-t SENSE) reconstruction approach [99].

Functional analysis

Left-ventricular functional assessment is performed to validate the cine images reconstructed with our approach. The volume of the left ventricle V_{LV} was calculated by the hemi-cylindrical hemi-ellipsoidal model, based on the cine images in 4ChV and SAX [100]:

$$V_{LV} = 5/6AL, \quad (4.1)$$

where A is the cross-sectional area of the left ventricle in the mid-ventricular SAX slice and L is the length of the left ventricle, measured in the 4ChV. The EDV and ESV of the LV were determined and the EF was calculated by

$$EF = (EDV - ESV)/EDV. \quad (4.2)$$

These measures were also calculated for the standard Cartesian cine scan. Functional analysis was repeated three times by one observer. EDV, ESV and EF determined by our approach and the Cartesian cine scan were compared by a Student's t-test.

4.3 Results

4.3.1 Numerical simulations

Data acquisition was simulated using the numerical XCAT phantom. Images of all four coils for an arbitrary TI image are shown in Figure 4.3. 16 TI images were simulated (Figure 4.4). Reconstructed TI images using iterative model-based image reconstruction were comparable to

4. SIMULTANEOUS T_1 MAPPING AND CINE IMAGING USING ITERATIVE MODEL-BASED RECONSTRUCTION

the reference TI images, but undersampling artefacts were still present and image intensities were slightly lower compared to the reference. In Figure 4.5, the behaviour of the iterative process is shown. Over the iterations, the k-space is filled and TI images gained sharpness. In T_1 maps, more details became visible. In the flip angle map, streaking artefacts became present over the iterations. The T_1 map showed a convergence behaviour with accurate T_1 estimation in the septum (iteration 40: 1351.0 ± 59.2 ms, reference: 1350 ms) and slightly longer T_1 in the blood pool of the LV compared to the ground truth, but within the STD (iteration 40: 1770.0 ± 108.1 ms, reference: 1750 ms, Figure 4.6).

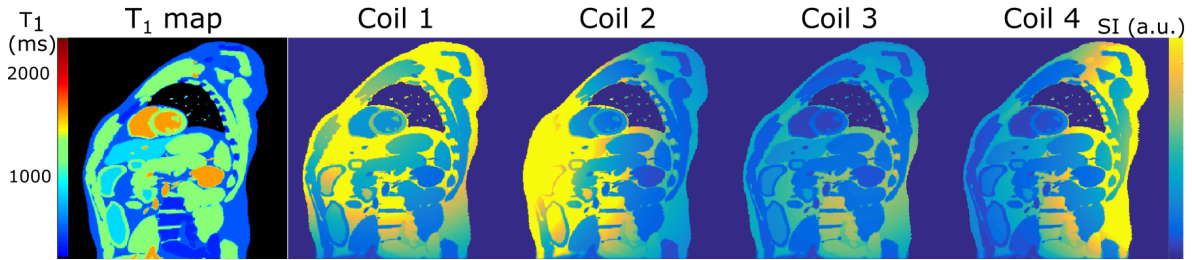


Figure 4.3: Simulated T_1 map and qualitative TI images of all coils.

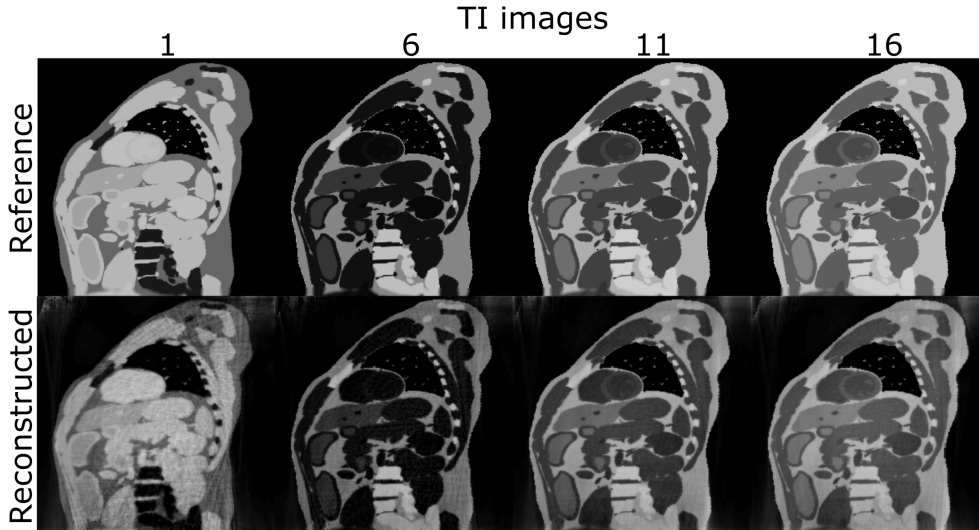


Figure 4.4: Reference and reconstructed TI images. TI images obtained by model-based image reconstruction show good agreement with simulated TI images.

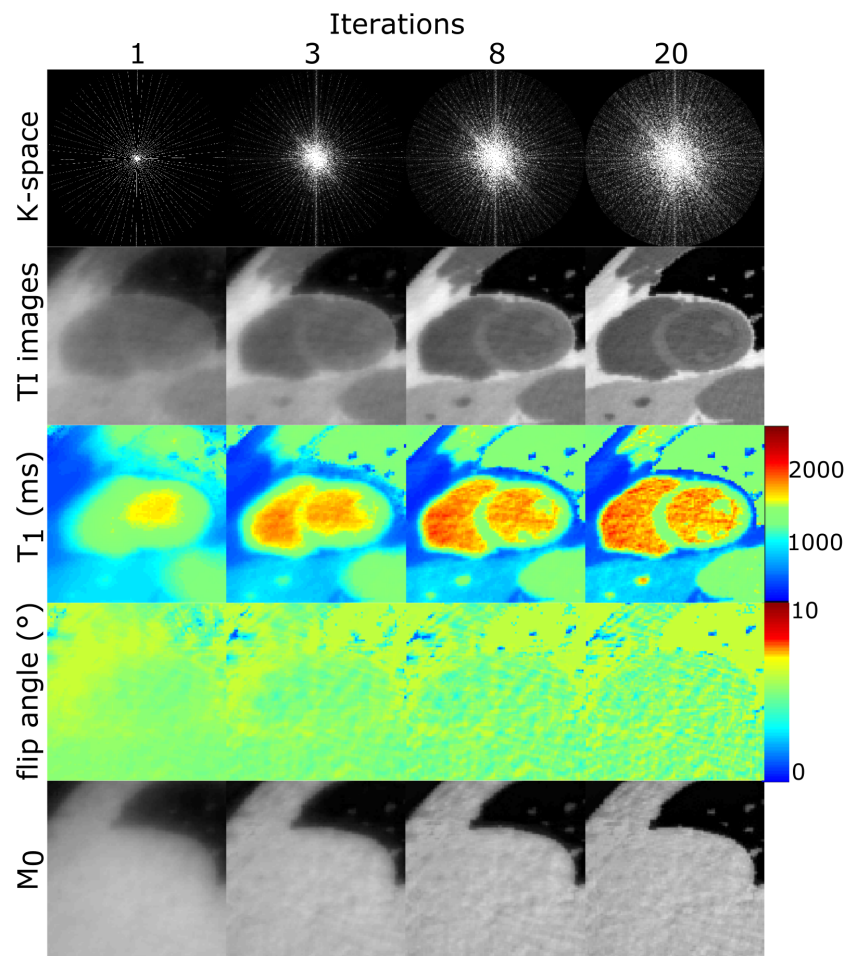


Figure 4.5: Evolution of k-space and images during the iterative process in numerical phantom. The k-space is filled and images of all fit parameter gain more and more details over the iterations. Undersampling artefacts and noise are still present in all maps.

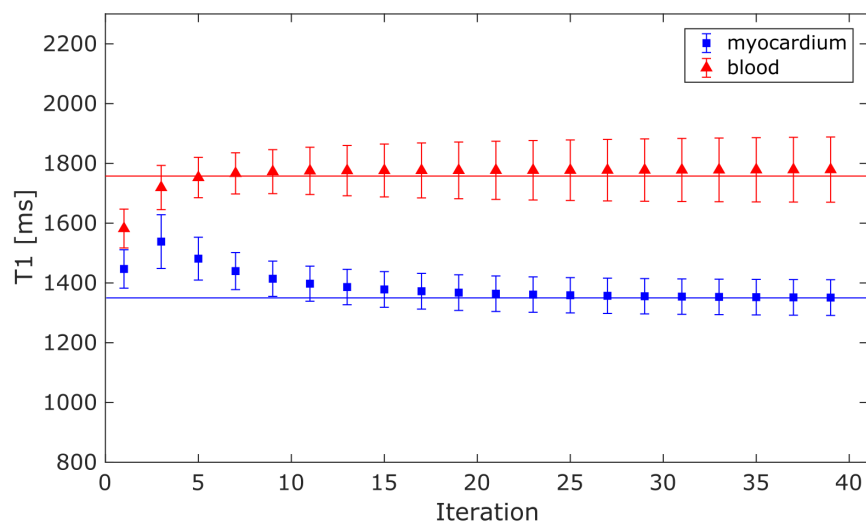


Figure 4.6: Convergence behaviour of estimated T_1 in blood and myocardium over iterations in numerical phantom.

4. SIMULTANEOUS T_1 MAPPING AND CINE IMAGING USING ITERATIVE MODEL-BASED RECONSTRUCTION

4.3.2 Phantom experiments

Evaluation of T_1 accuracy

Figure 4.7 compares the T_1 times estimated by the proposed technique to the T_1 times determined by the reference IR-SE sequence. Linear correlation indicates strong agreement between the two methods, with a R^2 of > 0.99 for all simulated heart rates (50 – 120 bpm) (Figure 4.7a). The relative difference over all T_1 times and all simulated heart rates between the proposed approach and IR-SE sequence was $-0.3 \% \pm 2.5 \%$ (mean \pm STD), with a normalized root mean square error of 2.5 % (Figure 4.7b,c). No significant correlation was found between T_1 and the heart rate for all T_1 times ($R^2 < 0.38$, $P > 0.1$) for the proposed method. T_1 times obtained by MOLLI were inversely correlated to the heart rate for $T_1 \geq 830$ ms (Figure 4.7c).

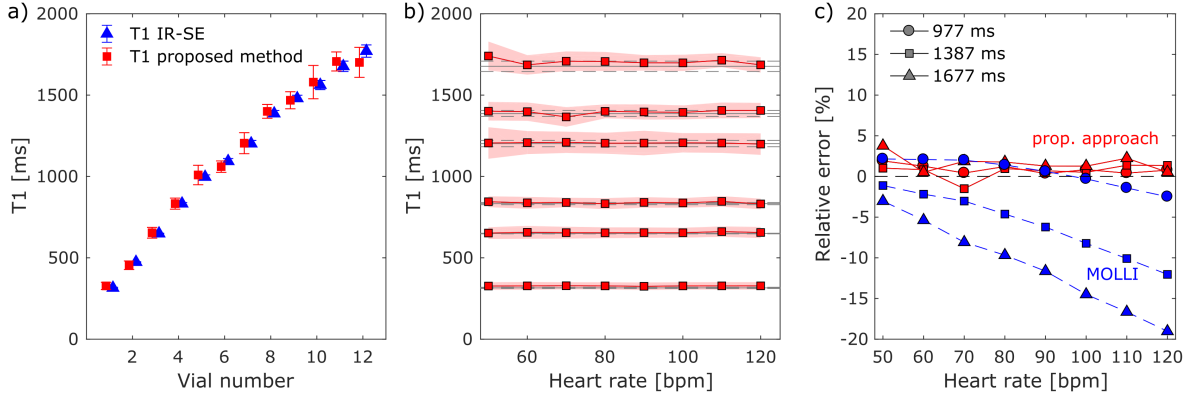


Figure 4.7: Phantom evaluation. a) T_1 mapping accuracy in a phantom with a simulated heart rate of 70 bpm. Error bars indicate T_1 values (mean \pm STD) measured using the proposed method (red squares) and the IR-SE reference (blue triangles) in each vial. b) Heart rate dependence in T_1 mapping of the proposed method, represented as mean \pm STD. Gray lines correspond to the mean T_1 values (solid line) and STD (dashed lines) measured on the IR-SE sequence. T_1 mapping was consistent across different heart rates. c) Heart rate dependence in T_1 mapping accuracy of the proposed method and MOLLI (red and blue, respectively), represented as relative difference to the IR-SE experiment for two relevant T_1 values. No significant correlation of T_1 and the heart rate was found in our method, whereas MOLLI showed an inverse correlation with the heart rate for $T_1 \leq 830$ ms [J2].

4.3.3 In vivo study

T_1 reconstruction

The evolution of maps of all fitted parameters (T_1 , flip angle and M_0) over 18 iterations of the model-based reconstruction is shown in Figure 4.8. T_1 and M_0 maps became sharper over the iterations. The estimated flip angle was lower compared to myocardium. Figure 4.9 shows the T_1 evolution over the iterations in a septal ROI and the blood pool of the left ventricle in one subject (mean \pm STD). T_1 times of myocardium, as well as T_1 of blood, converged after as few as 10 to 15 iterations, with even lower spatial variation and faster convergence compared to the numerical phantom experiment. This convergence was found in all subjects, with recorded heart rates between 44 and 82 bpm, so the stopping criteria was set as a fixed number of 16 iterations. Representative T_1 maps of healthy subjects in SAX and in 4ChV

orientation are shown in Figure 4.10 and 4.11, respectively. In addition to the diastolic T_1 maps, systolic T_1 maps were reconstructed from the same k-space data (Figure 4.10).

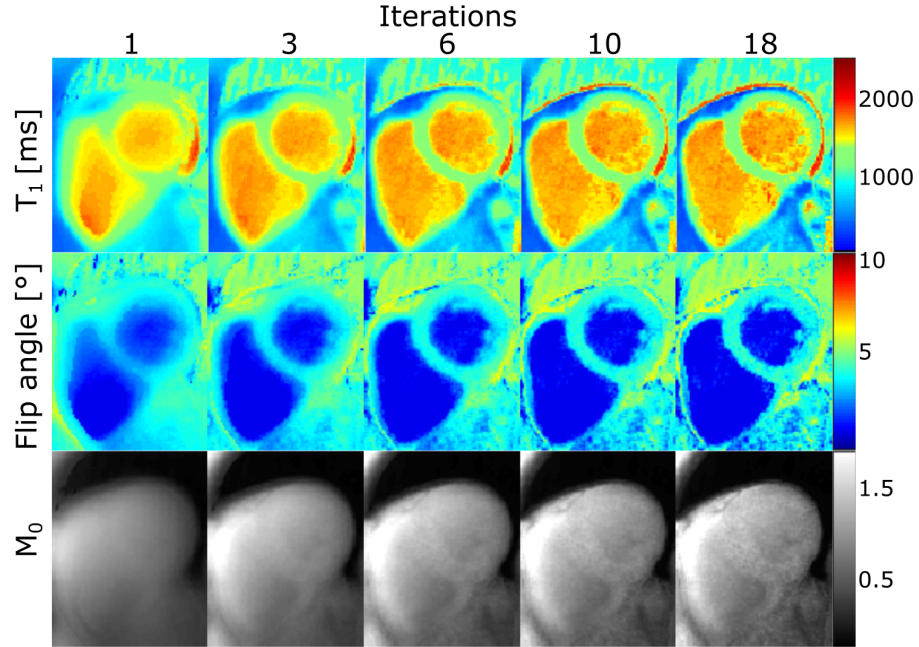


Figure 4.8: Evolution of all fitted parameter over 18 iterations in a healthy subject. T_1 , flip angle and M_0 show a convergence behavior.

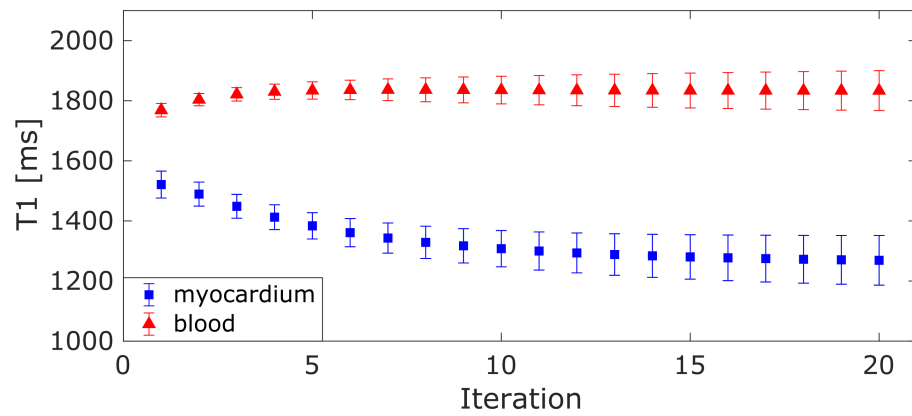


Figure 4.9: Evolution of in vivo T_1 times over the iterations in one volunteer. The error bars represent the T_1 values within a septal ROI and a ROI in the blood pool of the left ventricle (mean \pm STD). The iterative reconstruction shows a convergence behavior [J2].

4. SIMULTANEOUS T_1 MAPPING AND CINE IMAGING USING ITERATIVE MODEL-BASED RECONSTRUCTION

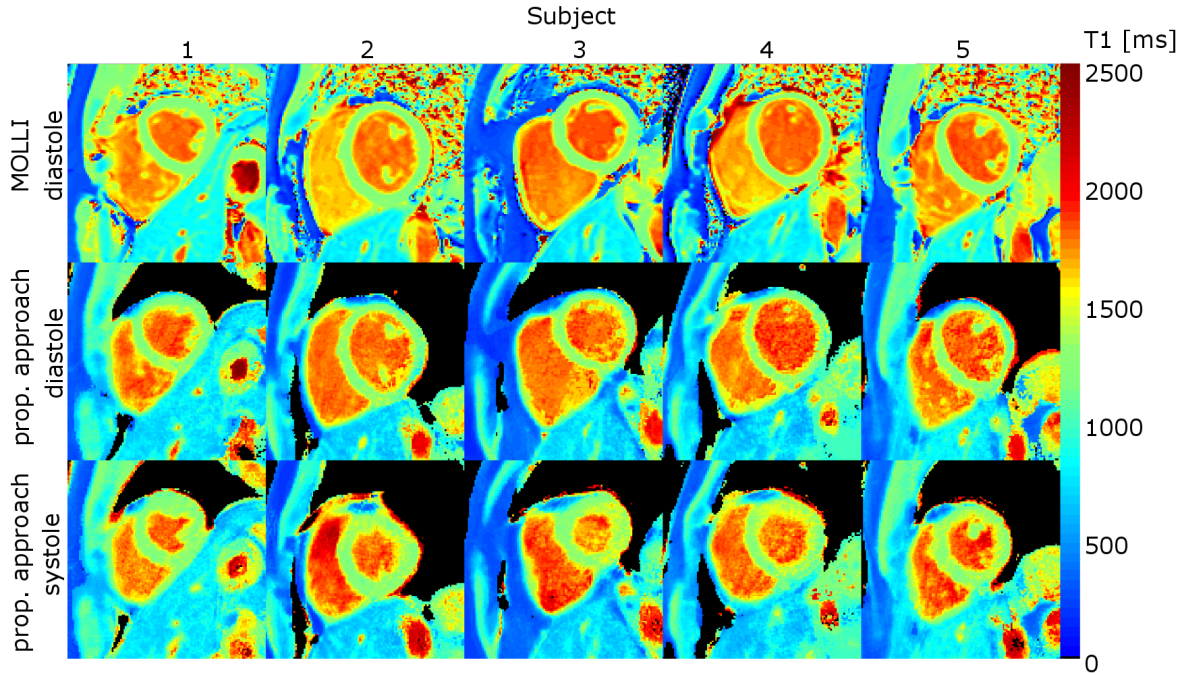


Figure 4.10: T_1 maps of five healthy volunteers in SAX view: Reconstructed diastolic T_1 maps (second row) are comparable to T_1 maps acquired by MOLLI (first row). Additionally, systolic T_1 maps were obtained by our approach (third row) [J2].

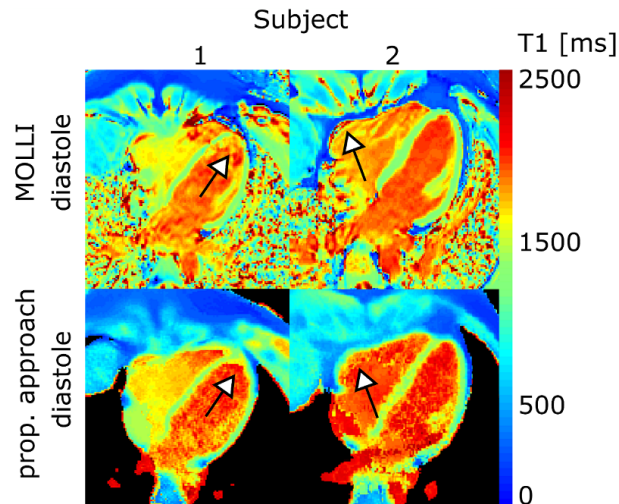


Figure 4.11: T_1 maps of two healthy volunteers in 4ChV: Diastolic T_1 maps of our approach (second row) are comparable to T_1 maps acquired by a MOLLI sequence (first row). Note that the apex and the right ventricle are better visible in the T_1 maps reconstructed with our approach than in the MOLLI T_1 maps (arrows), adapted from [J2].

T_1 analysis

Diastolic T_1 maps reconstructed with our approach were visually comparable to T_1 maps obtained by the 3(3)3(3)5 MOLLI sequence. The apex and the right ventricle were better visible than in MOLLI T_1 maps (Figure 4.11). T_1 times of all evaluated segments averaged over the ten subjects are shown in table 4.1. No significant differences were found between diastolic and systolic T_1 times obtained by our approach in SAX segments as well as in the 4ChV segment, except for the anterolateral SAX segment, with significant shorter T_1 times in diastole compared to systole, possibly because of partial volume effects with surrounding pericardium and lung tissue, that have short T_1 times. During diastole, this effect is more pronounced than during systole due to a thinner myocardial wall. Diastolic MOLLI T_1 times were significant shorter than corresponding diastolic T_1 times obtained by our approach in anterior, septal and inferior segments. In lateral segments, differences in T_1 between MOLLI and our approach were not significant.

Segments	MOLLI	Proposed approach	
	T_1 diastole	T_1 diastole	T_1 systole
SAX anterior	$1227 \pm 61^*$	1287 ± 32	1341 ± 73
SAX anteroseptal	$1250 \pm 35^\#$	1328 ± 72	1335 ± 87
SAX inferoseptal	$1248 \pm 51^\#$	1314 ± 62	1300 ± 97
SAX inferior	$1204 \pm 64^\#$	1303 ± 55	1347 ± 99
SAX inferolateral	1195 ± 60	1252 ± 54	1330 ± 91
SAX anterolateral	1231 ± 48	1248 ± 51	$1332 \pm 94^*$
4ChV midventricular septal	$1257 \pm 39^\#$	1328 ± 60	1324 ± 70

Table 4.1: T_1 times across ten healthy subjects. T_1 relaxation times are represented as mean \pm STD across the ten subjects. Diastolic T_1 relaxation times of our method were longer compared to MOLLI in all segments except for two lateral segments (*: $P < 0.05$, #: $P < 0.01$). Systolic and diastolic T_1 values obtained with our approach did not differ significantly, except for the anterolateral SAX segment, possibly because of partial volume effects with surrounding pericardium and lung tissue during diastole.

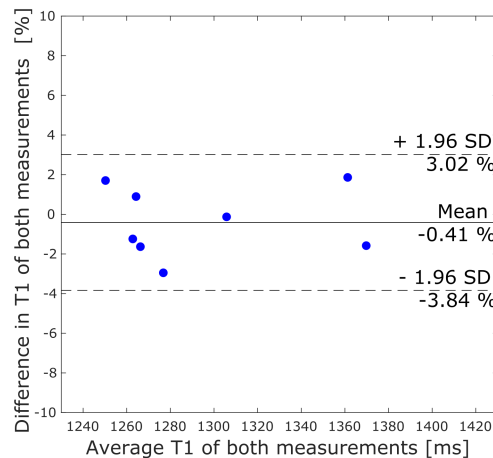


Figure 4.12: Reproducibility of T_1 mapping. T_1 quantification differences between the two repeated scans. The reproducibility experiment shows no differences between the two independent acquisitions ($P = 0.58$) [J2].

4. SIMULTANEOUS T_1 MAPPING AND CINE IMAGING USING ITERATIVE MODEL-BASED RECONSTRUCTION

The inter-subject variability, corresponding to the STD of septal T_1 times over the 10 volunteers, was 2.8 % (35 ms) and 3.7 % (48 ms) in diastolic images obtained by MOLLI and our approach, respectively. The in vivo precision was lower in our approach compared to MOLLI (averaged precision over all subjects: 65 ms and 34 ms, respectively, $P = 0.012$). In systolic T_1 maps, the precision was 57 ms.

The result of the repeatability evaluation is shown in Figure 4.12. The differences between the septal T_1 times were smaller than 3.5%, with a mean difference of $-0.41 \pm 1.75\%$ (mean \pm STD). The difference between the two subsequent measurements was not significant ($P = 0.58$).

T_1 maps of arbitrary cardiac phases were successfully reconstructed. In both cine T_1 maps, the cardiac cycle was visible (Figure 4.13). Myocardial T_1 mapping was robust over the cardiac phases. Blood T_1 showed a higher STD in mid-systole (Figure 4.13, phase 6). T_1 of static tissue did not differ visually.

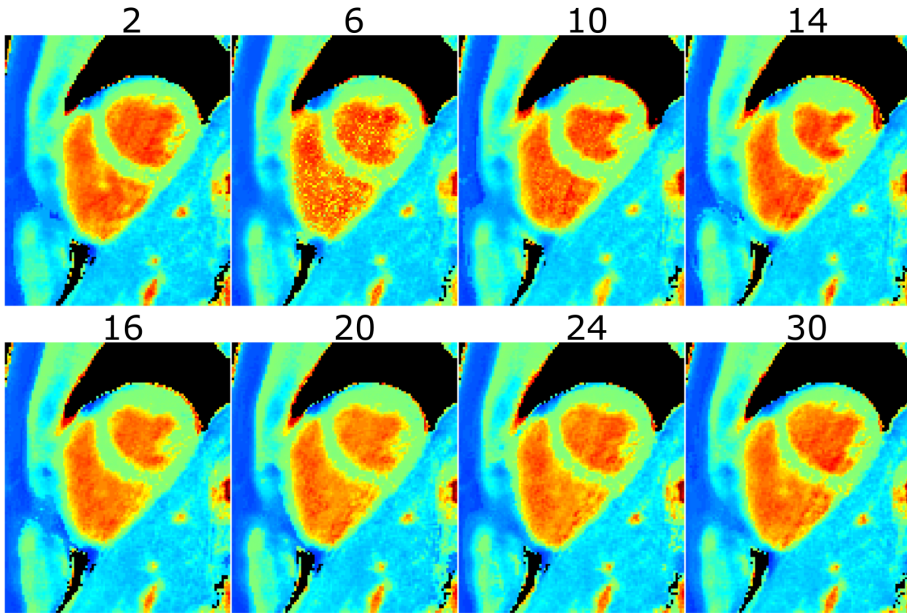


Figure 4.13: Cine T_1 mapping. Selection of the cardiac phase is arbitrary. Therefore, T_1 maps of each cardiac phase can be reconstructed, yielding a dynamic T_1 map. Here, eight out of the 30 cardiac phases are shown.

Cine reconstruction

Functional cine images could be reconstructed from the same k-space data as well. The images depict the anatomy as good as the Cartesian cine scan (Figure 4.14). The 30 cardiac phases obtained with the proposed technique have a consistent dark-blood contrast over the whole cardiac cycle. This can be seen in the temporal profile in Figure 4.14c.

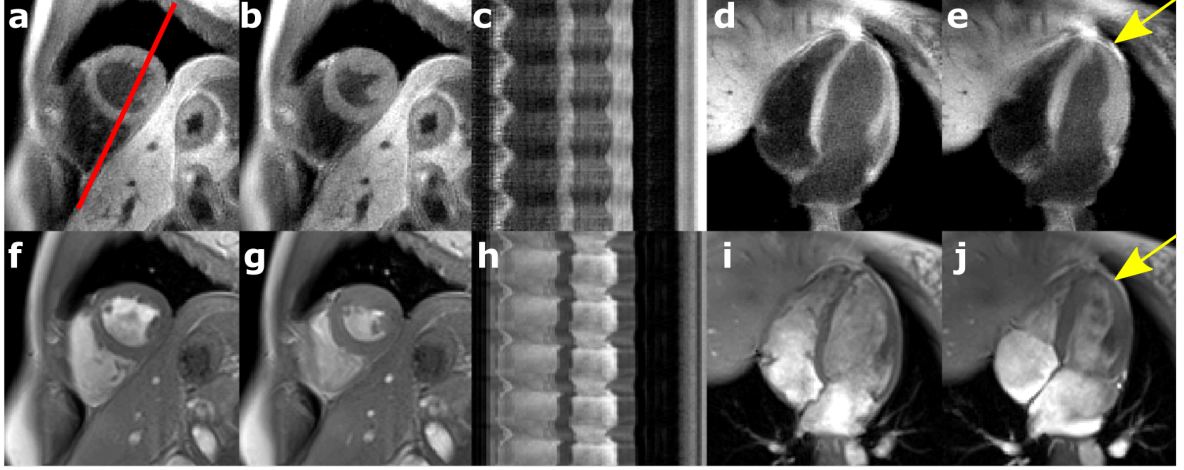


Figure 4.14: Cine images obtained with the proposed approach (a-e) and standard Cartesian cine scan (f-j). The temporal slice profiles in SAX (a and b, red line) are shown in c). Cine images in 4ChV are shown in d) and e). In f) to j), the same slices of the reference cine scan are shown. The dark-blood contrast provides a high contrast between myocardium and blood in the apical region (yellow arrow) [J2].

Functional analysis

The functional analysis of the cine images yielded the EDV, ESV and the EF for all subjects. Functional outcome of our approach and the standard Cartesian cine scan were in good agreement. The comparison between the functional analysis based on the Cartesian scan and our method is visualized as Bland-Altman plot in Figure 4.15. For all parameter, the mean differences between reference method and our approach were less than 1 %, with standard deviations of 5.63 %, 7.52 % and 2.65 % for EDV, ESV and EF, respectively. The differences between the two methods were not significant (EDV: $P = 0.97$, ESV: $P = 0.94$, EF: $P = 0.65$).

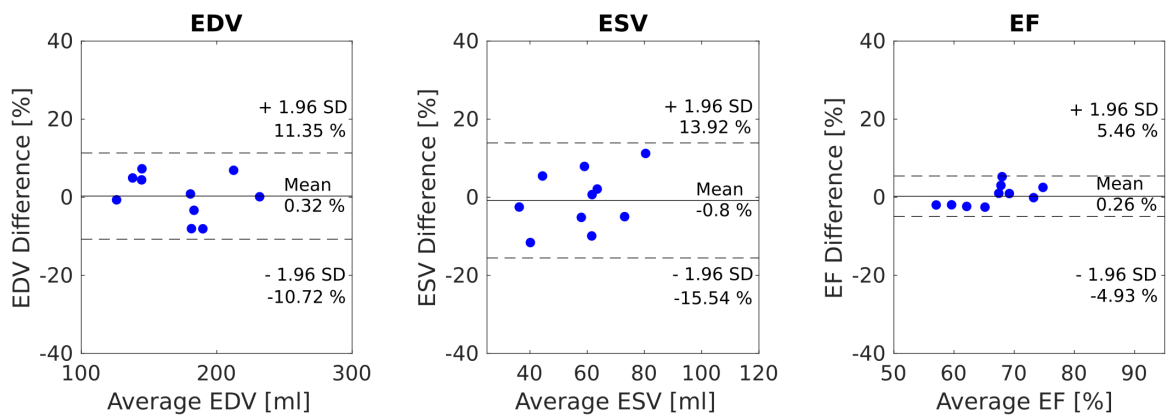


Figure 4.15: Functional analysis of the cine images. Bland Altman plot of functional parameter differences between the reference scan and the proposed cine reconstruction. The validation experiment showed good agreement between the two methods [J2].

4.4 Discussion

We proposed a novel acquisition and reconstruction approach which allows for simultaneous acquisition of native T_1 mapping and cine imaging. Using model-based iterative reconstruction, accurate and heart rate independent T_1 maps were obtained within 16 s. Robustness of T_1 mapping was demonstrated in numerical simulations, a T_1 phantom and in in-vivo experiments. Continuous data acquisition allowed for T_1 mapping for multiple cardiac phases from the same data set by retrospective data selection. Functional assessment based on reconstructed cine images was demonstrated to be as accurate as determination of functional parameter based on a standard Cartesian cine images.

In the T_1 phantom, T_1 times obtained by our approach showed accurate T_1 quantification over a wide range of T_1 times. Diastolic myocardial T_1 relaxation times obtained with the 3(3)3(3)5 MOLLI sequence were significantly shorter compared to our methods, except for lateral segments, where T_1 times showed a trend to be shorter in MOLLI, but differences were not significant. Differences between lateral and septal T_1 times can also be seen in other T_1 mapping techniques, such as multitasking [73] and could be caused by partial volume effects with surrounding pericardium or difficulties in segmenting the thin myocardium when selecting the diastolic ROIs for evaluation. Systolic T_1 times were more homogeneous across segments, possibly because of a thicker myocardium, which is easier to segment and less partial volume effect of surrounding blood (septum) or pericardium (lateral wall) occurs.

The difference in T_1 obtained by MOLLI and our approach was expected because of previously reported underestimation of MOLLI T_1 times [101, 14, 53, 61, 102].

The in vivo precision of our approach was lower compared to MOLLI (65 ms and 34 ms, respectively). In MOLLI, data was obtained with a resolution of $1.4 \times 2.1 \times 8.0 \text{ mm}^3$ compared to a resolution of $1.3 \times 1.3 \times 8.0 \text{ mm}^3$ in our approach. Additionally, a bSSFP readout was used in MOLLI. Differences in readout and a lower resolution in MOLLI could result in a higher SNR, which could possibly explain the differences in precision. Nevertheless, the precision of our method was better than for another dynamic T_1 mapping technique using a continuous spoiled gradient echo readout as proposed by Weingaertner et. al, that reported a precision between 90 and 150 ms, despite a lower resolution of $1.9 \times 1.9 \times 10.0 \text{ mm}^3$ [71]. The inter-subject variability of T_1 times was 2.8 % in MOLLI and 3.7 % in our approach, respectively. Both variabilities are in line with other studies in healthy subjects [103, 53, 71].

In vivo experiments demonstrated no differences in repeated T_1 mapping for heart rates between 44 and 82 bpm, suggesting robustness of the approach. The advantage of our approach was, that the spoiled gradient echo readout was less sensitive to B_0 inhomogeneities than a bSSFP readout and motion artifacts were minimized by radial data acquisition [104]. Especially in 4ChV, that led to a better depiction of the apex and small structures, such as the myocardial wall of the right ventricle, compared to MOLLI.

In MOLLI, heart rate dependence of T_1 has been shown, which is in line with previous studies [101, 49, 102]. No correlation was found between heart rate and T_1 in the phantom study using the proposed approach, including heart rates between 50 and 120 bpm. In MOLLI, the timing of inversion pulses is based on a fixed number of heart cycles, assuming full recovery of longitudinal magnetization before the application of the next inversion pulse.

This assumption is not true for high heart rates and therefore T_1 is underestimated. The model underlying our T_1 reconstruction algorithm takes the exact temporal evolution of the signal into account and thus the proposed technique is suggested to provide accurate T_1 maps independent of the heart rate.

The numerical simulations demonstrated a convergence behaviour of T_1 estimation over the iterations using iterative model-based image reconstruction for highly undersampled data, with an undersampling factor of 11 per image, without the need for temporal or spatial filtering. The in vivo data showed the same convergence behaviour as the numerical simulations (Figure 4.6 and 4.9) and the obtained in vivo precisions of diastolic and systolic T_1 in the myocardium were comparable to the numerical simulations (65 ms, 57 ms and 59 ms, respectively).

As shown in the numerical simulations in chapter 3, through-plane motion reduced the effective flip angle for diastole and systole. In the in vivo flip angle map, a smaller effective flip angle was fitted compared to the adjusted flip angle, which is in line with the numerical simulation in chapter 3. In blood, a low flip angle was fitted, which is also in line with the inflow simulation in chapter 3. Therefore, it is assumed that T_1 of blood can also be estimated in vivo.

Radial sampling with golden-ratio-based readout provided nearly optimal k-space coverage for flexible selection of the data and continuous acquisition allows for T_1 reconstruction of any cardiac phase. Thus, reconstruction of dynamic T_1 maps was possible. The stopping criterion was set to a fixed number of iterations. In our study, this stopping criterion was sufficient because of the convergence behavior of the T_1 maps over the iterations, which was similar in all volunteers. However, other stopping criteria could have been chosen. For example, the algorithm could have been stopped if the difference in quantitative T_1 map of two subsequent iterations was below a certain threshold as suggested previously [76]. During iterative T_1 reconstruction, data consistency is only ensured by substitution of acquired data. Using substitution, also initial noise in the data will be included again during each iteration. To improve the reconstruction, the reconstruction problem could be reformulated to a least square minimization term. This might allow for additional regularization terms to further improve the achievable parameter estimation [90, 92].

Reconstructed cine images had a consistent dark-blood contrast over all cardiac phases. The contrast between blood and myocardium in our cine images was caused by the global inversion and thus depended on the difference in T_1 times. That ensured a homogeneous contrast over the entire heart independent of the scan orientation. For the standard bright-blood cine images on the other hand, the contrast was based on the inflow of blood. In 4ChV, blood was partly saturated leading to reduced contrast in the apical region.

Ventricular volumes were determined based on one SAX image and one 4ChV image. Functional assessment could also be performed based on other methods for cardiac MRI. In a clinical setting, a stack of SAX images should be considered, which is recommended in patients with cardiac pathologies [105]. Nevertheless, the functional assessment utilized in this study has been shown to be in good agreement with the estimation of EDV and ESV using a stack of SAX images in healthy subjects [106] and thus this method is sufficient for our feasibility study.

4. SIMULTANEOUS T_1 MAPPING AND CINE IMAGING USING ITERATIVE MODEL-BASED RECONSTRUCTION

Simultaneous acquisition of cardiac function and T_1 mapping provides high scan efficiency, because both scans were acquired within one breath-hold. In addition, cine images provide information which could be used for the analysis of T_1 maps. Especially in patients with pathologies, such as epicardial fat or myocardial crypts - structures that hamper the visibility of the blood-myocardial interface [14, 107], contouring of a ROI for T_1 analysis could be done in the cine image, where the contrast between blood and myocardium could be higher than in the reconstructed T_1 map. Compared to obtaining T_1 maps and cine scans in different breath-holds, no further registration must be performed between the two scans.

The cine image could also be used to optimize the temporal location of the window used for the reconstruction of the T_1 maps retrospectively. This could minimize the influence of motion on T_1 mapping, especially for systolic T_1 maps and could be of importance for patients suffering from cardiomyopathies with atypical wall motion.

The acquisition window for T_1 mapping was set to 168 ms in our experiments. That was sufficiently short for mid-diastole, but it was longer than the common duration of mid-systole. We have chosen for the same acquisition window in diastole and systole for better comparison between the two T_1 maps. A shorter acquisition window for systole would be possible as well, obtaining the same image quality and slice profile through both ventricles, as shown in Figure 4.16. Additionally, motion correction techniques could be implemented to further reduce the acquisition window, as shown in chapter 6 for diastolic T_1 mapping. Additionally, radial data acquisition is less sensitive to motion than Cartesian sampling, providing systolic T_1 maps with negligible motion artifacts in our images. Furthermore, the window size was comparable or even shorter than in other studies investigating systolic T_1 mapping with Cartesian sampling [108, 52].

Systolic T_1 maps provide additional diagnostic information in conjunction with diastolic T_1 maps. In patients with thin myocardium, such as in dilated cardiomyopathies, high partial volume effects can occur between the blood pool and the myocardium [108, 52, 51] and quantitative measures are suggested to be sensitive to myocardial thickness [109]. Systolic and diastolic T_1 times did not differ significantly in our study. In literature, controversial findings about systolic T_1 times were made. In Reiter et al., T_1 times in systole were shorter than in diastole. Weingärtner et al., Ferreira et al. and Tessa et al. found no differences in diastolic and systolic T_1 times, which is in line with our study [52, 51, 71]. Having T_1 maps of diastole

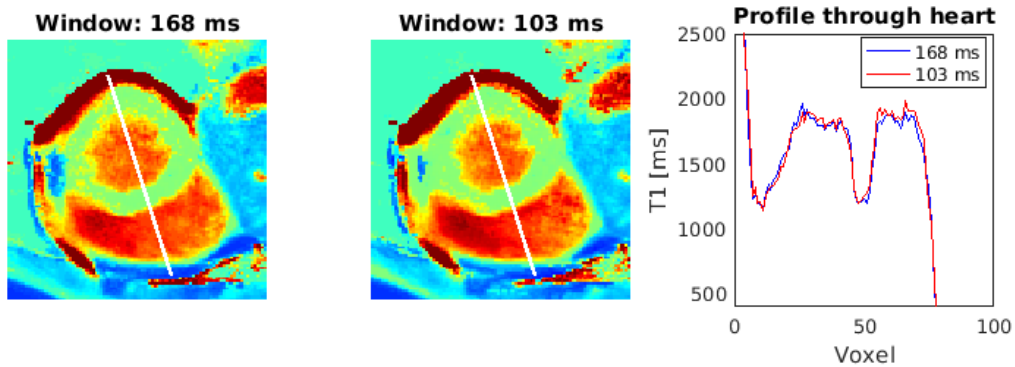


Figure 4.16: Systolic T_1 maps with different acquisition windows and slice profiles. Reduction of the acquisition window to 61% of the initial used window do not impact T_1 mapping quality.

and systole enables diagnosis to be made with more certainty without prolonging the total scan time using our approach. Reconstructed cine T_1 maps could further help to correlate myocardial viability directly to cardiac function by visual inspection of just the cine T_1 map instead of cine images and T_1 maps.

4.5 Conclusion

This study has shown the feasibility of simultaneous acquisition for native T_1 mapping of multiple cardiac phases and cine imaging, which could strongly improve the scan efficiency. Within 16 s, cine images and T_1 maps of diastole and systole could be obtained using continuous data acquisition model-based iterative image reconstruction. Additionally, functional assessment based on reconstructed cine images could be performed. In this chapter, T_1 mapping has been shown only for the left ventricle, but fibrosis is considered to play a role in cardiomyopathies with atrial and RV involvement, such as arrhythmias [110]. T_1 mapping in atria and RV is challenging using conventional approaches because of the thin myocardial wall. Here, it was shown that T_1 mapping was possible with a higher spatial resolution compared to conventional T_1 mapping techniques. Therefore, feasibility for T_1 mapping using model-based reconstruction in atria and RV is proposed in the next chapter.

5

High-resolution T_1 Mapping of all four Chambers

This chapter has been presented in [C4]: Becker et al., In vivo myocardial tissue characterization of all four chambers using high-resolution quantitative MRI, Current Directions in Biomedical Engineering, 2018, vol. 4(1), pp. 263-266, which has been published in final form at <http://doi.org/10.1515/cdbme-2018-0064>.

5.1 Introduction

In chapter 4, T_1 mapping is shown for the left ventricle. Fibrosis is considered to play a role in various cardiomyopathies, with atrial and RV involvement, such as arrhythmias [110]. Qualitative CMR is used in clinical routine to detect fibrosis by LGE in the ventricles and atria [111], but is limited to focal fibrosis, whereas quantitative MRI (T_1 , T_2 and T_2^* mapping) has become an important modality for myocardial tissue characterization [85, 86]. T_1 mapping offers a method to assess focal and diffuse fibrotic tissue and post-contrast T_1 times are suggested to be associated with atrial and ventricular fibrosis in arrhythmic patients [112, 113, 114]. However, contrast agents are required and observed T_1 times are strongly depend on the contrast dose and delay time between contrast administration and measurement.

Native T_1 mapping overcomes these limitations. Its main challenge is cardiac motion which strongly limits the achievable in-plane spatial resolution to approximately $1.3 \times 1.3 \text{ mm}^2$ (chapter 4) and therefore the iterative model-based T_1 mapping technique was only evaluated in the left ventricle. For imaging of smaller structures, such as the right ventricle or the atria, with a thickness of less than 3 mm [21], this spatial resolution is not sufficient and due to the small thickness of the atrial and right ventricular wall, even small cardiac motion can strongly impair the reconstructed T_1 maps. The correct beginning and duration of data acquisition has to be set prior to the data acquisition and hence can only be estimated prospectively.

5. HIGH-RESOLUTION T_1 MAPPING OF ALL FOUR CHAMBERS

Here we demonstrate the feasibility of a native T_1 mapping technique with an in-plane resolution of $1.0 \times 1.0 \text{ mm}^2$, that allows for mapping of all four chambers non-invasively. Cine images are obtained from the same data prior to T_1 reconstruction, comparable to chapter 4. The motion information is utilized to select only data with minimal cardiac motion for T_1 mapping specifically for each subject and scan. This personalized approach minimizes motion-induced blurring and optimizes the amount of data available for T_1 mapping. The model-based iterative reconstruction technique is used to obtain accurate T_1 maps obtained directly from the MRI raw data. This ensures high quality T_1 maps even from highly undersampled MRI data.

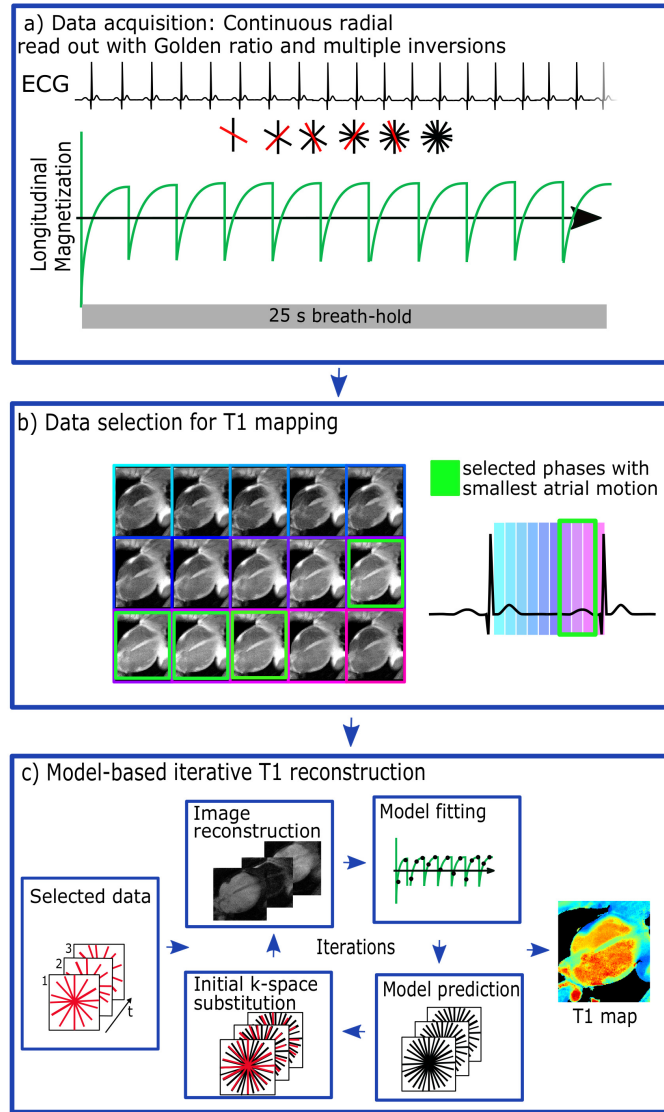


Figure 5.1: T_1 mapping of all four chambers. a) Data acquisition during a 25 s breath-hold. b) Data selection for high-resolution T_1 mapping. Based on the cine image of the same acquisition, data for T_1 mapping within a window with minimal cardiac motion was selected. c) T_1 was estimated using model-based iterative reconstruction.

5.2 Methods

5.2.1 T_1 mapping

2D data acquisition was performed as described in chapter 3 and 4 (Figure 5.1a). In order to be able to select data with minimal atrial motion, dark blood functional cine images showing the changes of the heart during the cardiac cycle were reconstructed prior to T_1 mapping from the same raw data (Figure 5.1) [115]. Cine reconstruction was performed using an iterative kt-SENSE approach [99]. Based on the cine images, a time interval for T_1 mapping was selected, where cardiac motion was minimal (Figure 5.1a). The length of this interval is flexible and can be optimized retrospectively for each subject. T_1 maps of the selected data were reconstructed by model-based iterative reconstruction of the data as introduced in chapter 4 (Figure 5.1c) [115, 76].

5.2.2 In vivo imaging

The proposed approach was evaluated in three healthy volunteers (3 males, aged 29.7 ± 3.5 years). Within a 25 s breath-hold, 2D slices were acquired with the following settings: in-plane resolution: $1.0 \times 1.0 \text{ mm}^2$, FOV: $320 \times 320 \text{ mm}^2$ with 2-fold oversampling in radial direction, slice thickness: 8.0 mm, flip angle: 5° , TE/TR: 2.03/5.3 ms and T_{ic} : 2276 ms. Slices were oriented in 4ChV and an apical short axis (ASAX), which is oriented through both atria.

Cine images were reconstructed with 15 cardiac phases. Data for T_1 mapping were selected in a window between 300 and 360 ms per cardiac cycle, depending on cardiac motion. For comparison purpose, T_1 mapping was also performed by a common T_1 mapping technique for mapping of the left ventricle, a 3(3)3(3)5 MOLLI [46] in ASAX orientation in one of the subjects with the following settings: FOV: $360 \times 307 \text{ mm}^2$, slice thickness: 8.0 mm, in-plane resolution: $2.1 \times 1.4 \text{ mm}^2$ and integrated motion compensation. T_1 values were assessed manually drawn ROIs in the septum, LA, RA and RV in 4ChV.

5.3 Results

High-resolution T_1 maps of the four chambers could be reconstructed for all subjects. T_1 values in the three subjects are shown in table 5.1. T_1 maps obtained by our approach and the MOLLI sequence are presented in Figure 5.2 and 5.3. The result of the voxel-wise fit is shown in Figure 5.4. R^2 of the fit was larger than 0.9 in all voxels within the heart. In Figure 5.5, a T_1 map is shown in 4ChV, together with a qualitative anatomical image from the same raw data and same cardiac phase and the overlay of the two images.

Subject	T_1 septum	T_1 right ventricle	T_1 left atrium	T_1 right atrium
1	1230 ± 84	1288 ± 91	1263 ± 89	1272 ± 143
2	1287 ± 73	1258 ± 85	1281 ± 90	1234 ± 126
3	1260 ± 76	1287 ± 67	1290 ± 76	1291 ± 135

Table 5.1: T_1 values obtained by our approach in all chambers in the three subjects (mean \pm STD within the ROI in ms).

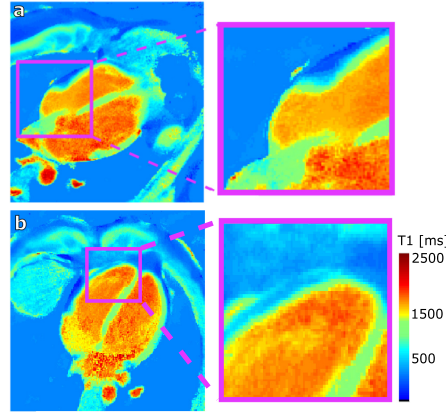


Figure 5.2: T_1 maps of two subjects in 4ChV. The myocardium of the right atrium can be visualized (a), as well as the myocardial wall of the right ventricle (b).

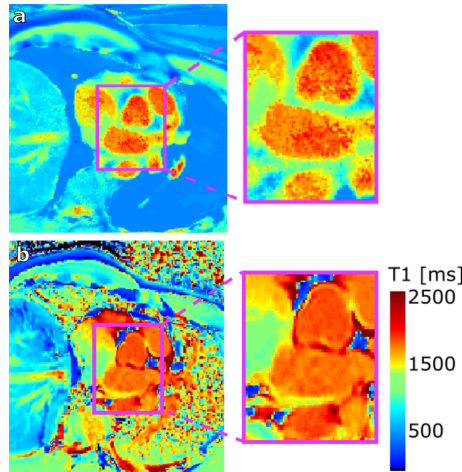


Figure 5.3: T_1 map through both atria. In this orientation, the myocardium of the left atrium can be visualized (a). b) T_1 map of the same subject obtained by a MOLLI sequence. Here, the myocardium of the left atrium cannot be fully distinguished.

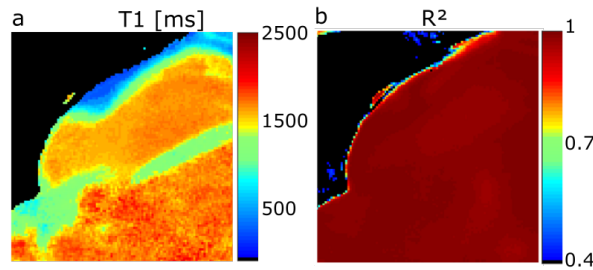


Figure 5.4: Result of the voxel-wise T_1 fitting. a) The T_1 map is masked by its R^2 map (b). Only T_1 values with a R^2 of larger than 0.9 are visualized. R^2 is larger than 0.9 in the entire heart.

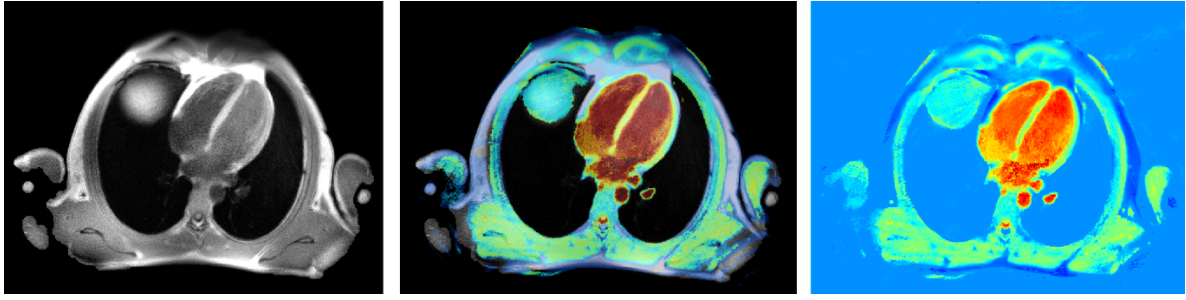


Figure 5.5: Overlay of T_1 and anatomy. Qualitative anatomical scan, anatomical scan overlaid with the T_1 map of the same acquisition and the T_1 map (left to right).

5.4 Discussion

Small structures, such as the myocardium of the RV and both atria can be seen in the T_1 maps. In ASAX orientation, myocardium of the LA can be visualized by our T_1 mapping approach, whereas the myocardial wall of the LA cannot be identified in the standard MOLLI T_1 map, which could possibly be explained by lower resolution and residual cardiac motion within data acquisition (Figure 5.3b). T_1 values of the chambers were in the range of septal T_1 in the same subjects and large R^2 values for all myocardial voxels suggest a robust fit. The STD within the atrial ROI is larger than in the septum. This could be explained by the smaller number of voxels in the right atrial ROI and larger partial volume effects because of the thinner myocardial wall. The overlay of T_1 map and structural image allows to immediately relate the T_1 values to its underlying anatomy without any misregistration errors due to varying breath-hold positions and could be used for further analysis of the T_1 map. Evaluation in patients with atrial and ventricular fibrosis has to be performed in future research.

5.5 Conclusion

Feasibility of T_1 mapping in both ventricles and atria was demonstrated for the first time. This was achieved by utilization of functional information for personalized selection of the quiescent phase of the heart. Motion artifacts were minimized while increasing the acquisition window individually. For further increase of the acquisition window, cine images could also be used for cardiac motion estimation and correction. Cardiac motion correction is implemented in T_1 mapping in the next chapter to further increase of scan efficiency and to reduce the scan time to a clinical feasible duration.

6

Native T_1 Mapping using cardiac motion correction

Parts of this chapter have been presented in [J1]: Becker et al., Fast myocardial T_1 mapping using cardiac motion correction, Magnetic Resonance in Medicine, 2020; vol. 83, pp. 438-451, which has been published in final form at <https://doi.org/10.1002/mrm.27935>.

6.1 Introduction

In chapter 4, a novel approach combining continuous data acquisition of chapter 3 and a model-based image reconstruction technique was presented, allowing for T_1 mapping and cine imaging simultaneously. In this chapter, functional information of the cine images were utilized to correct for cardiac motion, yielding a higher acquisition efficiency and a reduction of the acquisition time for cardiac T_1 mapping.

While respiratory motion may be largely suppressed by holding the breath during a 2D MR scan, cardiac motion is always present during data acquisition. Common myocardial T_1 mapping techniques therefore utilize ECG-triggering, where TI images are only acquired at one specific cardiac motion state, such as mid-diastole, after an inversion or saturation recovery preparation. However, such ECG-triggered acquisitions limit the amount of data used for image reconstruction to 10% - 20% per cardiac cycle, leading to low scan efficiencies [46, 47, 14]. This is especially challenging for T_1 mapping because multiple TI images need to be obtained for the calculation of one quantitative T_1 map. In order to ensure clinically feasible breath hold times, cardiac T_1 mapping is commonly limited in terms of spatial resolution. In addition, ECG-triggering requires reproducible detection of each cardiac cycle during data acquisition. Heart rate variations or arrhythmia can lead to TI images, which are obtained in different cardiac phases and the mismatch between these images could lead to errors in voxel-based T_1 mapping [14, 50].

6. NATIVE T_1 MAPPING USING CARDIAC MOTION CORRECTION

Continuous data acquisition with retrospective cardiac motion correction has been proposed for 3D anatomical CMR in order to improve scan efficiencies and make data acquisition not reliant on accurate ECG-triggering [116, 117]. For quantitative CMR, so far only respiratory motion correction has been explored to improve parameter map quality [57, 118, 56, 58, 70, 119]. These techniques correct for small residual respiratory motion in breath-held and free breathing acquisitions. Cardiac motion leads to a much more complex deformation of the heart than respiratory motion. Therefore, accurate cardiac motion estimation requires high quality cardiac motion resolved images with constant and high contrast between myocardium and blood.

In this chapter, a cardiac motion corrected T_1 mapping approach with an increased T_1 mapping efficiency is presented. This is done by continuous acquisition (chapter 3) allowing reconstruction of cine MRI and TI images from the same data. Nonrigid cardiac motion estimation was integrated to correct for motion before carrying out voxel-based T_1 mapping. Scan efficiency was increased by a factor of 5 compared to the model-based T_1 mapping approach of chapter 4, using 80% of the acquired data for T_1 mapping instead of 168 ms per cardiac cycle. The approach was applied to 10 healthy volunteers for native T_1 mapping. The impact of scan time and repeatability was evaluated in terms of accuracy and precision.

6.2 Methods

The proposed motion corrected T_1 mapping approach can be separated into three steps. First, cine images are reconstructed from the acquired 2D golden-ratio-based radial data. In a second step, these images are registered to obtain nonrigid motion fields describing the cardiac movement of each voxel during the cardiac cycle. Lastly, cardiac phase resolved images are reconstructed for different inversion times from the same data. Each cardiac phase is transformed to a reference phase using the motion fields obtained in step 2. Systolic cardiac phases were excluded due to through-plane motion allowing for 80% of the total scan time to be used for T_1 mapping. A voxel-wise 3-parameter T_1 fit is applied to obtain the final quantitative cardiac motion corrected T_1 maps.

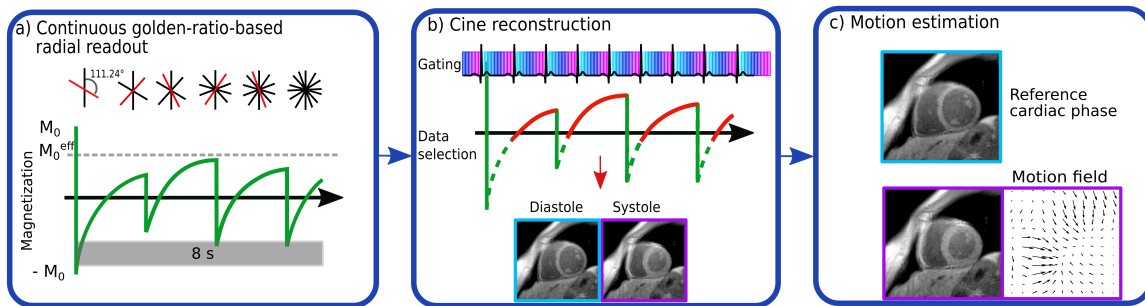


Figure 6.1: Data acquisition and cardiac motion estimation. a) Data is continuously acquired with golden-ratio-based radial read out. Multiple inversion rf-pulses were applied. b) Cine images with 15 cardiac phases were reconstructed prior to T_1 mapping. Only part of the data (red) is used for cine reconstruction to guarantee a constant contrast over all cardiac phases. Negative signal associated with healthy myocardium is rejected (dashed line). c) For each cardiac phase, a cardiac motion field is obtained.

6.2.1 Data acquisition

The same image acquisition was performed as in chapter 4. 2D slices were acquired continuously by a low flip angle spoiled-gradient echo sequence with golden-ratio-based radial sampling [93] and employing adiabatic IR-preparation at constant time intervals (Figure 6.1). Data was acquired within a breath hold on 3 T (Verio, Siemens Healthineers): flip angle: 5° , TE/TR: 2.03/4.93 ms, FOV: $320 \times 320 \text{ mm}^2$, with 2-fold oversampling in radial direction, resolution: $1.3 \times 1.3 \times 8.0 \text{ mm}^3$ and non-selective inversion rf-pulses were applied every 2276 ms. The ECG was recorded for retrospective cardiac gating and data selection. Total acquisition time per slice was 16 s.

6.2.2 Cine reconstruction

Data was retrospectively binned into 15 cardiac motion states using the ECG signal providing cardiac motion resolved images (I_{Cine}^{1-15} , Figure 6.1b). The contrast over the entire scan is not constant, because of the application of multiple inversion pulses. Nevertheless, each image I_{Cine} is reconstructed from data at various time points after the inversion pulses. This leads to an average contrast for I_{Cine}^{1-15} which is constant over all reconstructed cardiac motion states. In order to enhance the contrast between blood and myocardium, data was only used for cine reconstruction if the signal intensity of myocardium was positive. Data acquired immediately after all inversions was therefore excluded for reconstruction, depending on the T_1 times associated with healthy myocardium. Data taken 1175 ms after the first inversion and 400 ms after all other inversions were excluded (Figure 6.1b). Thus, only the positive signal of myocardium is used. Blood has a longer native T_1 time, so the signal from blood is lower and partly negative resulting in dark blood images (Figure 4.1). The acceleration factor of native cine images was 5.0. I_{Cine}^{1-15} were reconstructed iteratively using spatial and temporal total variation regularization (10 iterations, $\lambda_{\text{spatial}} : 10^{-6}$, $\lambda_{\text{temporal}} : 5 \cdot 10^{-6}$) [120]. All image reconstruction was performed offline in MATLAB (The MathWorks, Inc., Natick, USA).

6.2.3 Motion estimation

Nonrigid cardiac motion estimation was performed on the cine images. As reference cardiac phase, the mid-diastolic phase was used. For image registration, a Free-Form Deformation algorithm [121] was used, composed of a cubic B-Spline interpolation scheme as deformation model, normalized mutual information as similarity metric and bending energy as penalty term (NiftyReg) [122]. A rectangular ROI covering both ventricles was selected in a first step to accelerate motion estimation. No segmentation of myocardial contours was needed. Motion estimation yielded one cardiac deformation field per cardiac motion state describing the transformation from each cardiac phase to the reference motion state (Figure 6.1c, MF^{1-15}). In order to test motion estimation, these motion fields are applied to each cardiac phase, i.e. $\text{MF}^{1-15} \circ I_{\text{Cine}}^{1-15}$, transforming all cardiac phases to the same motion state and thus providing a motion corrected image sequence.

6.2.4 Motion corrected T_1 mapping

Cardiac motion corrected T_1 mapping (T_1^{moco}) contains the following steps (Figure 6.2a):

1. *Gating*: Data was retrospectively gated yielding exactly the same 15 cardiac motion states as in cine reconstruction. In contrast to the cine reconstruction before, 15 phases for each cardiac cycle are obtained rather than retrospectively combining data from multiple cardiac cycles.
2. *Data selection*: Based on the reconstructed cine images of the same acquisition, three systolic cardiac phases were excluded in each cardiac cycle to minimize through-plane motion artifacts in the T_1 maps, which cannot be corrected for in a 2D acquisition.
3. *Image reconstruction*: In each cardiac cycle (C_1 to C_n), 12 highly-undersampled TI images (TI^{1-12}) were reconstructed of the same cardiac motion states as selected for cine reconstruction (TI_{C1-Cn}^{1-12}). TI images were reconstructed using non-Cartesian iterative SENSE [123] without temporal or spatial filtering of the data. The total data window for T_1 mapping was 80% per cardiac cycle, divided into 12 TI images.
4. *Motion correction*: Prior to T_1 mapping, corresponding deformation fields MF^{1-12} were applied to all TI images TI_{C1-Cn}^{1-12} . Thus, 12 motion corrected TI images were obtained for each cardiac cycle:

$$mcTI_{C1-Cn}^{1-12} = MF^{1-12} \circ TI_{C1-Cn}^{1-12}. \quad (6.1)$$

5. *T_1 estimation*: T_1 , M_0 and the flip angle were estimated by a voxel-wise fit of the magnitude $mcTI_{C1-Cn}^{1-12}$ images to the signal model (3.5) introduced in chapter 3.

Three additional T_1 maps were calculated based on the same raw data. To verify the influence of motion correction on T_1 estimation, the same TI images were selected as above, but no motion correction step was performed prior to T_1 mapping, yielding T_1^{uncorr} maps. Besides this, motion-uncorrected T_1 maps were calculated without exclusion of three systolic phases, reconstructing TI images of all 15 cardiac phases (TI_{C1-Cn}^{1-15}), yielding $T_1^{15uncorr}$ maps. The influence of the increased amount of k-space lines compared to standard cardiac triggered T_1 mapping approaches was evaluated (Figure 6.2b). For this, data during mid-diastole was selected within a single window per cardiac cycle with a duration of 168 ms, as performed in chapter 4. Here, the quality of each TI image is better because of the larger window length and hence more available k-space data per TI image, but total amount of data used for T_1 mapping is lower. These T_1 maps are called T_1^{1phase} maps throughout the study.

6.2.5 Phantom experiments

To evaluate the proposed approach, imaging was performed with the above described scan parameter in a phantom with nine different T_1 times, investigated for cardiac applications [124]. Furthermore an IR-SE method was applied for reference with seven inversion times between 25 and 4800 ms, TE/TR: 12/8000 ms, FOV: 130×160 mm² and spatial resolution:

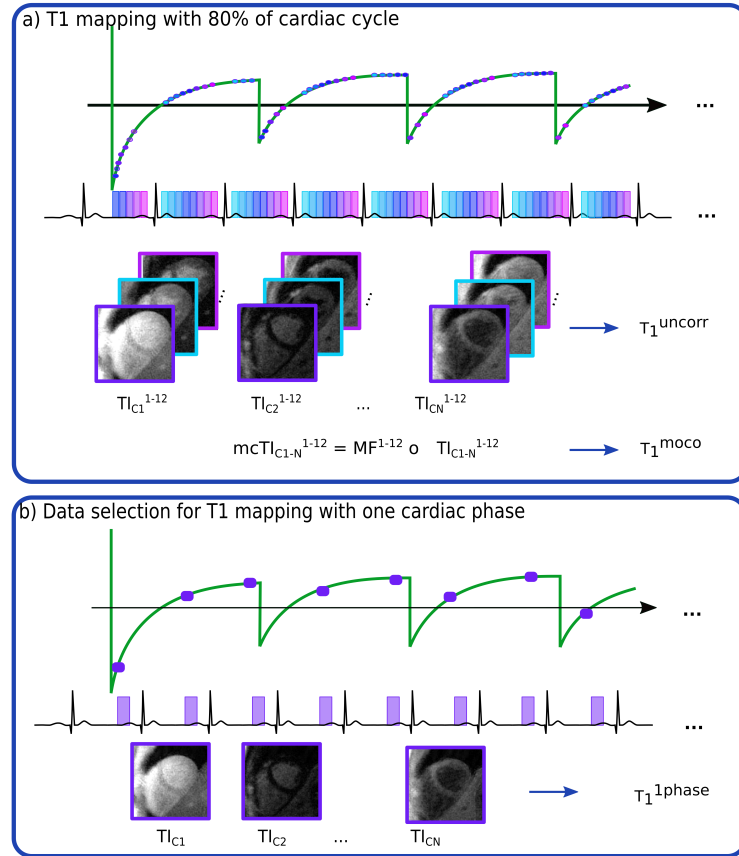


Figure 6.2: T_1 mapping using 80% of the cardiac cycle. The cardiac cycle is split into the same cardiac phases as for cine reconstruction, leading to 15 qualitative images per cardiac cycle and three mid-systolic images were excluded. Cardiac motion is corrected in TI images and T_1 is fitted, leading to T_1^{moco} . Furthermore, T_1 is also fitted on motion-uncorrected TI images (T_1^{uncorr}). b) For comparison purpose, T_1 mapping is performed using reconstructed TI images of only one cardiac phase of the same data acquired as in a) (T_1^{1phase}). The window length was 168 ms per cardiac cycle, comparable to a standard T_1 mapping approach.

$1.3 \times 1.3 \times 8 \text{ mm}^3$. Reference T_1 times were estimated based on voxel-wise fit. Additionally, a 5(3)3 MOLLI was applied with the following scan parameter: FOV: $360 \times 306 \text{ mm}^2$, TE/TR: 1.12/2.70 ms, flip angle: 35° and spatial resolution: $2.1 \times 1.4 \times 8.0 \text{ mm}^3$.

6.2.6 In vivo experiments

The approach was applied in 10 healthy subjects (6 males/ 4 females, aged 31.3 ± 8.4 years) in a mid-ventricular SAX orientation. A stack of 9 SAX images was obtained in one healthy volunteer (male, 34 years) with the approach and 5(3)3 MOLLI. In accordance with the institutions' ethical committees, all participants gave written informed consent before examination. In order to study potential effects on different scan orientation, additional images were obtained in four chamber view in two of the subjects. T_1^{moco} , T_1^{1phase} and T_1^{uncorr} maps were calculated for each acquisition. In short-axis orientation, images were acquired twice in eight subjects to test repeatability.

6. NATIVE T_1 MAPPING USING CARDIAC MOTION CORRECTION

Cine images and T_1 maps were obtained with two different acquisition times. First, data of the entire 16 s acquisition was utilized. Additionally, for evaluation of reducing the scan time, only the first 8 s were used for cine reconstruction as well as T_1 mapping.

6.2.7 Analysis

In the phantom, T_1 times were averaged over each tube. Pearson’s linear correlation was tested to test accuracy of the approach and differences in T_1 time between reference and the proposed approach as well as reference and MOLLI were calculated and averaged over all tubes.

In vivo analysis was performed in mid-ventricular SAX images. Six mid-ventricular myocardial segments of the LV, adapted from the American Heart Association consensus statement, and the left-ventricular blood pool were segmented [98]. Segmentation and evaluation were performed using in-house software in MATLAB (The MathWorks, Inc., Natick, USA) and GraphPad Prism 6 (La Jolla, USA).

Motion estimation

Motion fields (MF^{1-15}) were applied to the cine images ($MF^{1-15} \circ I_{Cine}^{1-15}$), in order to visually assess motion correction. To investigate the amplitudes of estimated motion, the deformation fields of each cardiac motion state were quantified. For the quantification, the norm of the 2D deformation vectors in each voxel was determined for all cardiac phases and averaged in each segment. The cardiac phase with maximum deformation over all six segments was determined in each subject and averaged over all volunteers. After exclusion of three systolic phases, the remaining maximum deformation was averaged over all volunteers.

Additionally, the deformation of 8 s cine images was obtained over the 10% of the voxels with highest deformation in each segment and cardiac phase and subsequently, the highest deformation was averaged over all volunteers. To test accuracy and robustness of the motion estimation, an additional test was performed on the motion fields. Estimated inverse motion fields of the 12 included cardiac phases were applied to the reference cine images ($iMF^{1-12} \circ I_{Cine}^{ref}$). In a second step, these obtained cine images were again registered to I_{Cine}^{ref} , obtaining new cardiac motion fields. This was done for all ten healthy subjects. Differences between both motion fields were calculated for each cardiac phase and each segment.

T_1 mapping method

T_1 times were assessed in all myocardial and blood segments. Normal distribution of T_1 times was tested by a Shapiro-Wilk test. To verify overall effects of the T_1 mapping method on T_1 times, T_1 times of T_1^{moco} , T_1^{phase} and T_1^{uncorr} maps obtained in 8 s were averaged over the six segments and compared using a Friedman test with Dunn’s multiple comparison correction.

In this study, STD of T_1 times across a segment (spatial variability) was used to quantify the precision of the measurement in healthy subjects because in healthy volunteers the T_1 times of the myocardium can be assumed to be constant.

The STD of native T_1 was determined in each segment. Normal distribution of STDs was tested by a Shapiro-Wilk test. Overall differences in STD between the three methods were

assessed by a comparison of the STD over the whole myocardium between T_1^{moco} , T_1^{1phase} and T_1^{uncorr} maps by ANOVA with Tukey’s multiple comparison correction across the 10 healthy volunteers.

For comparison to MOLLI, T_1 times were assessed segment-wise in basal, midventricular and apical slices and averaged. Spatial variation was averaged over all segments for analysis of precision.

Impact of scan time

Estimated deformation of the left ventricle was compared for cine images obtained from 16 s and 8 s of the acquired data. T_1^{moco} maps obtained in 8 s were compared with 16 s T_1^{moco} maps in terms of accuracy and precision. T_1 times and STDs were obtained in all myocardial segments. For statistical analysis, T_1 times and STD were averaged over the whole myocardium in each subject. Normal distribution of T_1 times and STDs within the myocardium were both tested by a Shapiro-Wilk test. Student’s paired t-tests were utilized to test differences in T_1 and STD between both T_1 maps.

Repeatability

To evaluate the robustness of the motion corrected T_1 mapping approach, T_1^{moco} mapping in 8 s and SAX was repeated. Estimated deformations in all six segments were obtained for both acquisitions and the maximum deformation of the whole myocardium was calculated.

T_1 times of the whole left ventricle STD over the whole left ventricle were compared between both T_1 maps by a Wilcoxon matched-pairs signed rank test. For visual investigation, a Bland-Altman analysis was performed for myocardial T_1 times as well as STD.

6.3 Results

6.3.1 Phantom experiments

Cardiac motion corrected T_1 mapping and MOLLI showed good correlation with the IR-SE reference scan ($R^2 > 0.99$). Relative differences between reference and both techniques averaged over all tubes were $0.28\% \pm 3.70\%$ (range: -5.42% to 3.88%) using our approach and $1.43\% \pm 1.99\%$ (range: -1.42% to 4.61%) using 5(3)3 MOLLI. A comparison between reference and our approach can be found in Figure 6.3.

6.3.2 Cine reconstruction

Cine images resulted in a dark-blood contrast (Figure 6.4, 6.5 and 6.6) and had a consistent contrast over all 15 cardiac phases, which can be observed in the temporal profile (Figure 6.6). Cine reconstruction worked for SAX as well as 4ChV orientation. The temporal resolution of each cardiac phase was between 55 and 87 ms in SAX, depending on the heart rate (46 - 73 bpm) and only few streaking artefacts were present in cine images. No differences were depicted between cine images reconstructed from 16 s and the first 8 s of the acquisition (Figure 6.4 and 6.5). In 16 s and 8 s cine reconstruction, different temporal regularization factors had to be set. However, the regularization factors were independent of the slice orientation.

6. NATIVE T_1 MAPPING USING CARDIAC MOTION CORRECTION

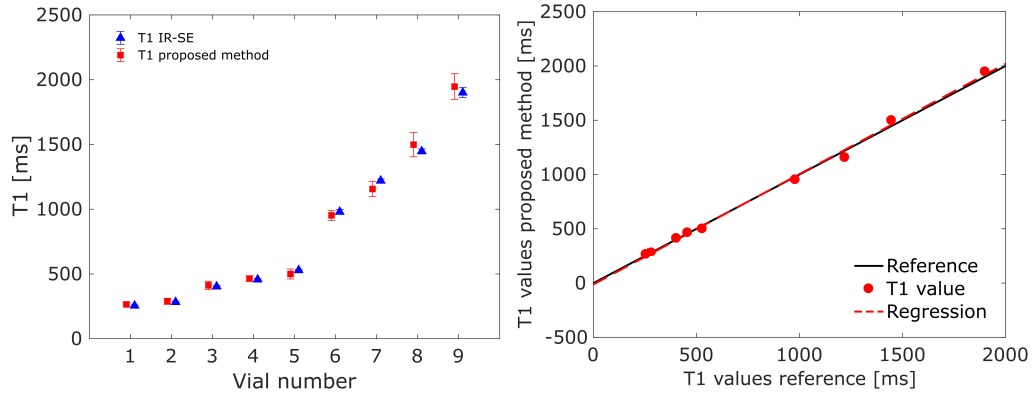


Figure 6.3: Phantom validation of motion corrected T_1 mapping. T_1 times showed good correlation with the reference IR-SE T_1 times ($R^2 > 0.99$). Differences were $0.28\% \pm 3.70\%$ over all 9 vials.

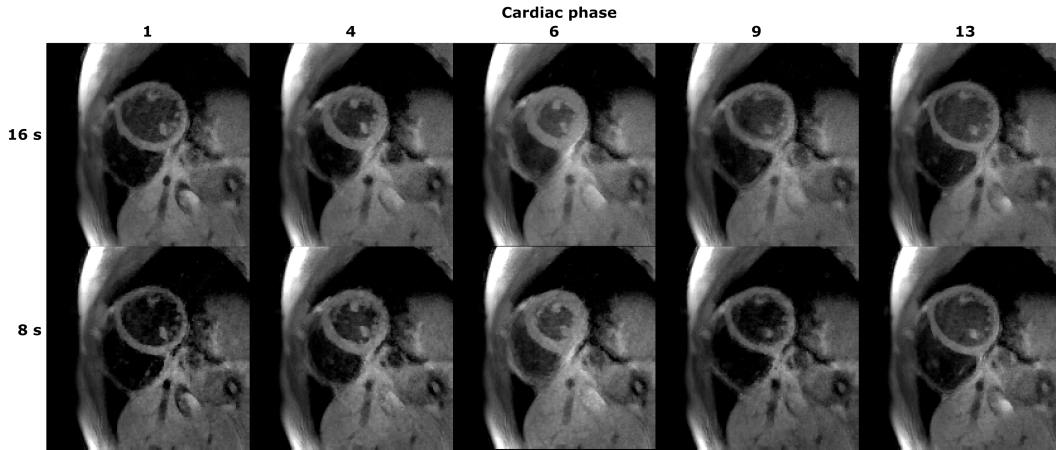


Figure 6.4: SAX cine images. Images were reconstructed from 16 s (upper row) and the first 8 s of the acquisition (lower row). Here, 5 of 15 cardiac phases are shown. Images have a consistent dark-blood contrast and no difference between 16 s and 8 s can be found.

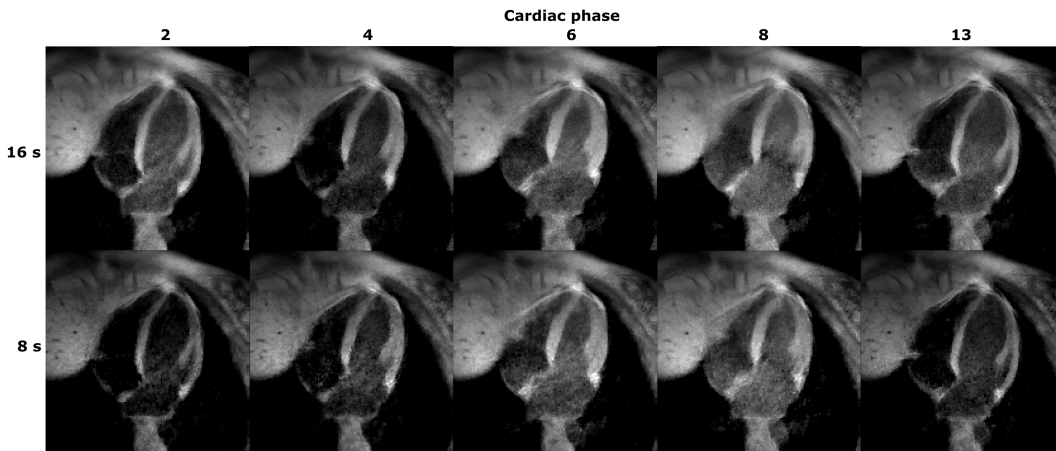


Figure 6.5: 4ChV cine images. Images were reconstructed from 16 s (upper row) and the first 8 s of the acquisition (lower row). Here, 5 of 15 cardiac phases are shown. Images have a consistent dark-blood contrast and no difference between 16 s and 8 s can be found.

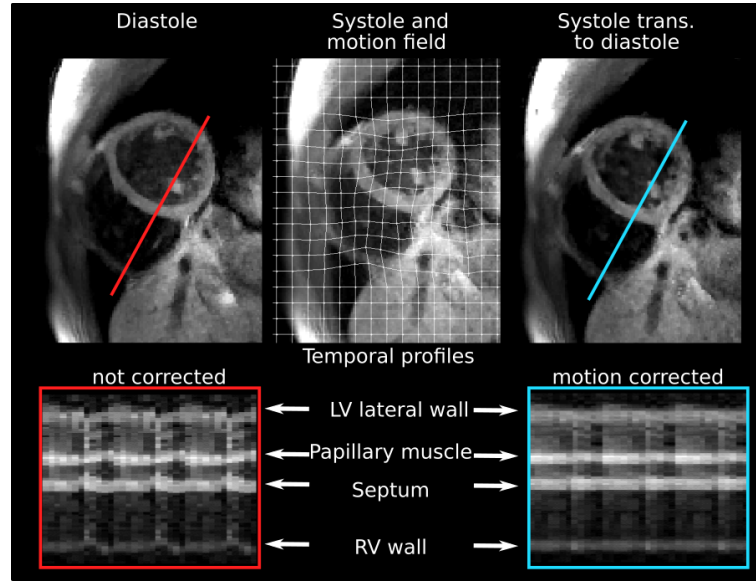


Figure 6.6: Motion correction on 8 s cine images. The deformation of the heart is estimated for each cardiac phase (middle) and motion is corrected (right) to match the reference mid-diastolic phase (left). The temporal slice profiles of cine images excluding three systolic phases are shown in the lower row (red line), adapted from [J1].

6.3.3 Motion estimation

Motion estimation succeeded in all volunteers, with the same motion estimation settings for all volunteers, but different parameter settings for SAX and 4ChV orientations. The deformation of the whole myocardium in two subjects can be found in Figure 6.7. The error bars indicate the STD over the six segments. The deformation per cardiac phase is strongly dependent on the subject and a similar deformation pattern can be found for 16 s and 8 s reconstructions. Furthermore, segment-wise evaluation shows different deformation per segment, averaged over the ten subjects (Figure 6.8). Highest deformation was found in anterior and inferior segments, which was consistent between 16 s and 8 s.

The highest deformation over all healthy subjects was 5.28 ± 1.50 mm in systole. Excluding three systolic motion states, as in T_1 mapping, the remaining highest deformation was still 3.98 ± 0.86 mm. When reducing the acquisition time to 8 s, the highest deformation over all healthy subjects was 4.51 ± 0.98 mm in systole and 3.30 ± 0.88 mm, when excluding three systolic motion states. This averaged deformation underestimates the maximum deformation of the myocardium because of large variations over the myocardium. The highest deformation in healthy subjects was 7.54 ± 1.89 mm.

Only small residual motion in cardiac motion corrected cine images ($MF^{1-15} \circ I_{Cine}^{1-15}$) are visible (Figure 6.6, in 8 s reconstruction). The effect of motion correction can also be seen in the temporal slice profiles of the cine images. The estimated motion per cardiac phase depended strongly on the heart rate, with an averaged motion of more than a voxel length of 1.3 mm in only 5 of 15 cardiac phases for a very low heart rate (46 bpm) and 9 cardiac phases for a higher heart rate (66 bpm, Figure 6.9).

The repeatability experiment showed small differences between motion estimations. Differences between both motion estimations were $0.25 \text{ mm} \pm 0.17 \text{ mm}$ [0.04 – 1.32 mm],

6. NATIVE T_1 MAPPING USING CARDIAC MOTION CORRECTION

averaged over all 15 cardiac phases, segments and volunteers. Only in one systolic cardiac phase of one healthy volunteer, the error was in the range of the voxel size (1.32 mm).

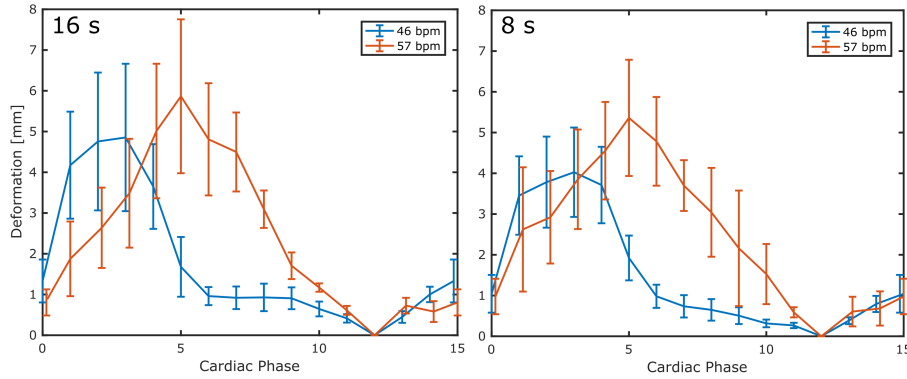


Figure 6.7: Estimated motion of two subjects in 16 s (left) and 8 s (right). Motion is averaged over the six segments; the error bars represent the STD of the deformation norm over the segments. The deformation depends strongly on the subject, with peak deformation in the fifth cardiac phase and nearly no quiescent phase in subject 1 (red, 57 bpm) and a peak deformation in phase three and a longer quiescent phase in subject 2 (blue, 46 bpm). The similar deformation evolution was found in 16 s and 8 s.

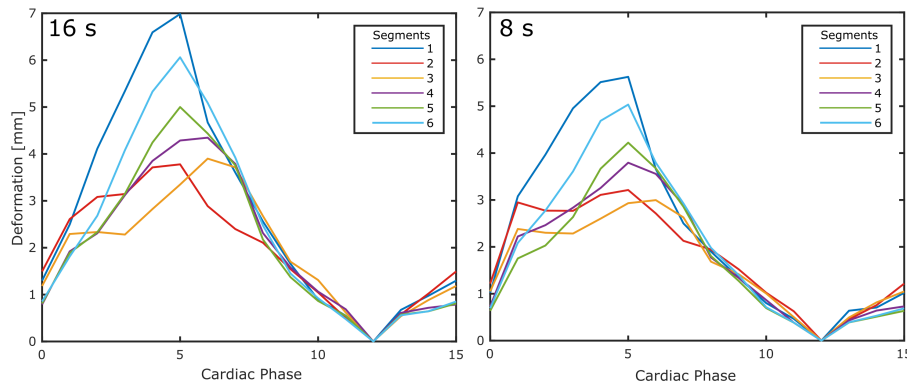


Figure 6.8: Deformation in each myocardial segment for 16 s (left) and 8 s (right). Deformation per cardiac phase was averaged over ten volunteers. Anterior and inferior segments showed highest deformation (1,6) and septal segments lowest (2,3). The trend was comparable between 16 s and 8 s, with higher detected deformation in 16 s compared to 8 s.

6.3.4 Native T_1 mapping

Motion corrected T_1 maps were compared to motion uncorrected T_1 maps and T_1 maps obtained with only one cardiac phase in 8 s. In SAX orientation as well as four chamber view, T_1^{moco} maps had less blurring and partial volume effects compared to $T_1^{15uncorr}$ and T_1^{uncorr} maps (Figure 6.10, 6.11 and 6.12). The myocardium and papillary muscles can be well distinguished in the T_1^{moco} maps. Excluding three systolic cardiac phases improved T_1 mapping quality compared to T_1 maps obtained with all 15 cardiac phases, but inhomogeneities were still present (Figure 6.10). The undersampling factor was 22.2 - 34.3 for each TI image, dependent on the heart rate. Maps of all fitted parameters can be found in Figure 6.13.

T_1 maps obtained with 80% of the cardiac cycle (T_1^{uncorr} and T_1^{moco}) showed lower STD in blood and myocardium than T_1^{1phase} maps (Figure 6.11 and 6.12). The total amount of data

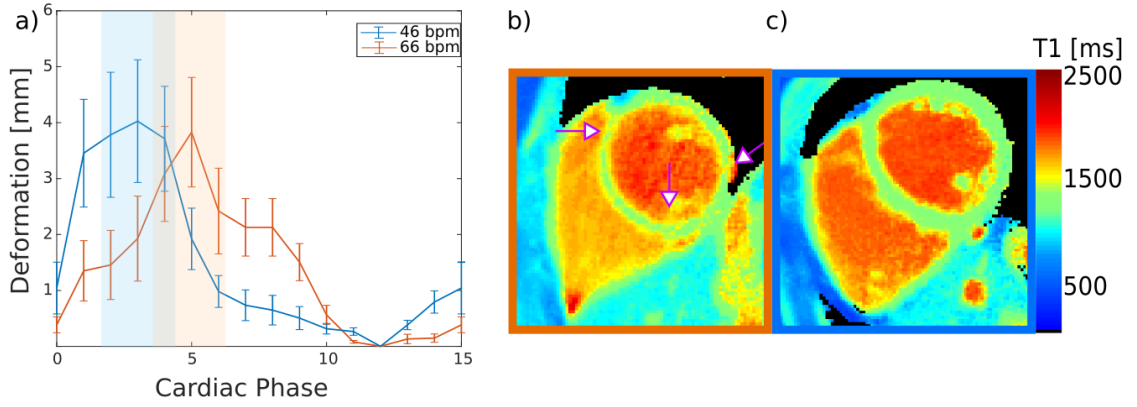


Figure 6.9: Impact of motion on uncorrected T_1 map at different heart rates. a) Estimated cardiac motion averaged over all six segments per cardiac phase (mean \pm STD). For low heart rates, only a few cardiac phases show motion amplitudes larger than the voxel size (blue) and no motion artifacts are visible in the corresponding T_1^{uncorr} map after exclusion of three systolic phases (c). For normal heart rates, even after excluding systolic phases, motion amplitudes are larger than the spatial resolution of 1.3 mm for most cardiac phases (orange). In the corresponding T_1^{uncorr} map, motion led to wrong T_1 estimation (b) [J1].

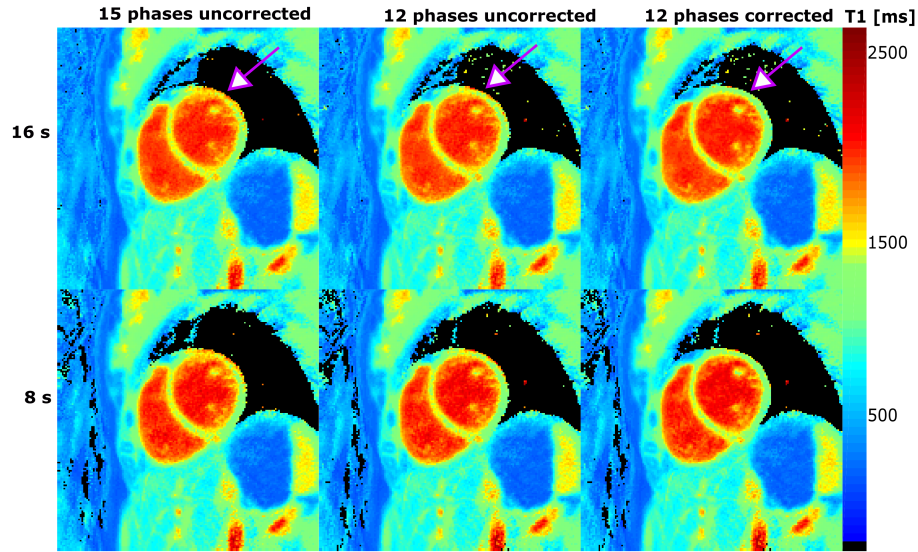


Figure 6.10: Impact of motion correction on T_1 maps. In T_1 maps obtained without excluding three systolic images ($T_1^{15uncorr}$, left), motion led to blurring of the myocardium. Excluding three systolic images ($T_1^{12uncorr}$, middle), less blurring was present, but still visible. In motion corrected T_1 maps, the T_1 times over the whole myocardium were homogeneous (T_1^{12corr} , right). No differences were found between 16 s and 8 s T_1 maps (upper and lower row, respectively).

used for T_1^{moco} and T_1^{uncorr} mapping was on average 5.2 (4.3 - 6.8) times higher compared to T_1^{1phase} mapping. In Figure 6.9, the influence of cardiac motion on T_1^{uncorr} maps is shown for different heart rates. The main difference between high and low heart rate was, that after leaving out three systolic phases (marked as blue area) only two cardiac phases show a deformation larger than a voxel length of 1.3 mm for a low heart rate (46 bpm). For the higher heart rate (66 bpm), six remaining cardiac phases show a deformation larger than 1.3 mm. Therefore, the impact of cardiac motion on the final image quality is higher for the high heart-rate case than

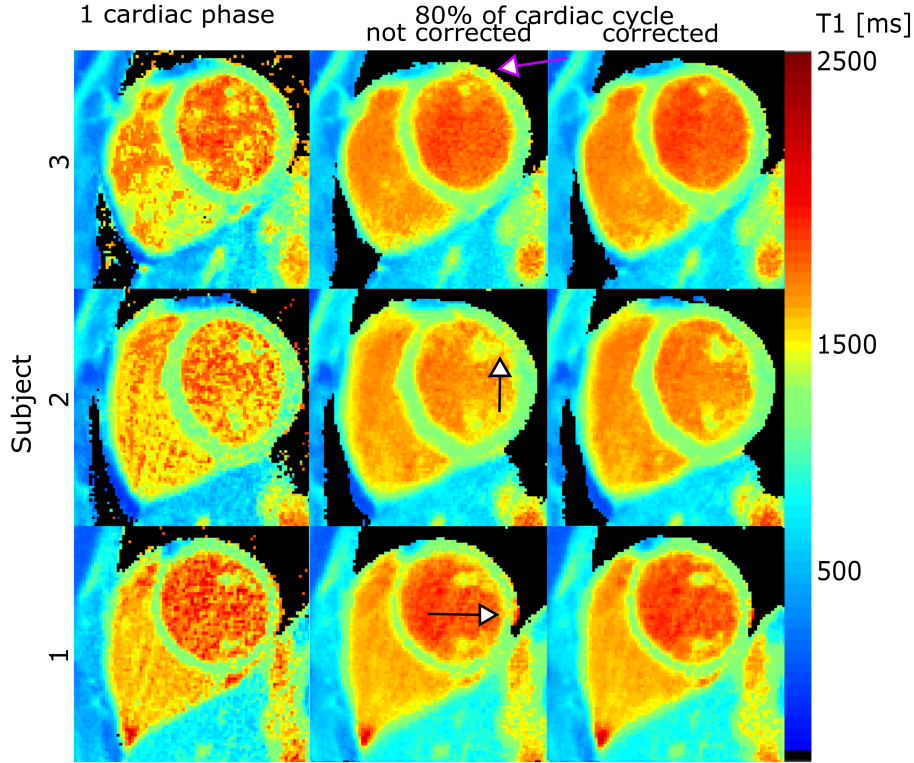


Figure 6.11: Native T_1 maps in 8 s of three healthy subjects. T_1 maps estimated using one cardiac phase (T_1^{1phase} , left) showed higher standard deviation compared to T_1 maps calculated from images covering 80% of each cardiac cycle. In motion uncorrected T_1 maps (T_1^{uncorr} , middle), motion led to blurring and partial volume effects (arrows), which is not present in motion corrected T_1 maps (T_1^{moco} , right) [J1].

for the low-heart rate case (Figure 6.9b,c). However, for heart rates in the normal range or higher (here shown for 66 bpm), cardiac motion resulted in inaccurate estimation of myocardial T_1^{uncorr} , which can be observed by regional prolonged T_1 times, because of a mismatch of motion state in uncorrected TI images (Figure 6.9b).

T_1 times and STDs of all myocardial segments and blood are shown in Figure 6.14. T_1^{1phase} , T_1^{uncorr} and T_1^{moco} times of the whole myocardium across all healthy volunteers were 1259 ± 55 ms, 1298 ± 60 ms and 1288 ± 49 ms respectively (Figure 6.14a). T_1^{uncorr} times were significant longer than T_1^{1phase} times ($P = 0.008$), whereas no significant differences were found between T_1^{moco} and T_1^{1phase} ($P = 0.281$) as well as T_1^{moco} and T_1^{uncorr} ($P = 0.539$).

The STD of T_1 within the myocardium was highest in T_1^{1phase} maps, with 94.8 ± 15.4 ms (Figure 6.14b). T_1^{uncorr} maps had a significant lower STD compared to T_1^{1phase} maps (62.44 ± 10.2 ms, $P < 0.0001$). By the integration of motion correction, the STD was further reduced (57.0 ± 12.5 ms, $P = 0.0356$). T_1^{moco} maps had a 40% lower STD in the myocardium compared to T_1^{1phase} maps across the healthy subjects ($P < 0.0001$). In blood, the STD was 53% lower in T_1^{moco} compared to T_1^{1phase} ($P < 0.0001$). No cardiac motion artefacts were observed in T_1^{1phase} maps. T_1^{moco} maps of the different slice positions of the stack of SAX slices were comparable to MOLLI (Figure 6.15). Basal, mid-ventricular, apical and blood T_1 times were 1217 ± 17 ms, 1196 ± 37 , 1224 ± 43 ms and 1898 ms in MOLLI. In T_1^{moco} maps, T_1 times were 1272 ± 40 ms, 1267 ± 35 ms, 1312 ± 20 ms and 1776 ms, respectively. Spatial variation was 46.5 ± 17.21 ms for MOLLI and 55.68 ± 17.71 ms for our approach.

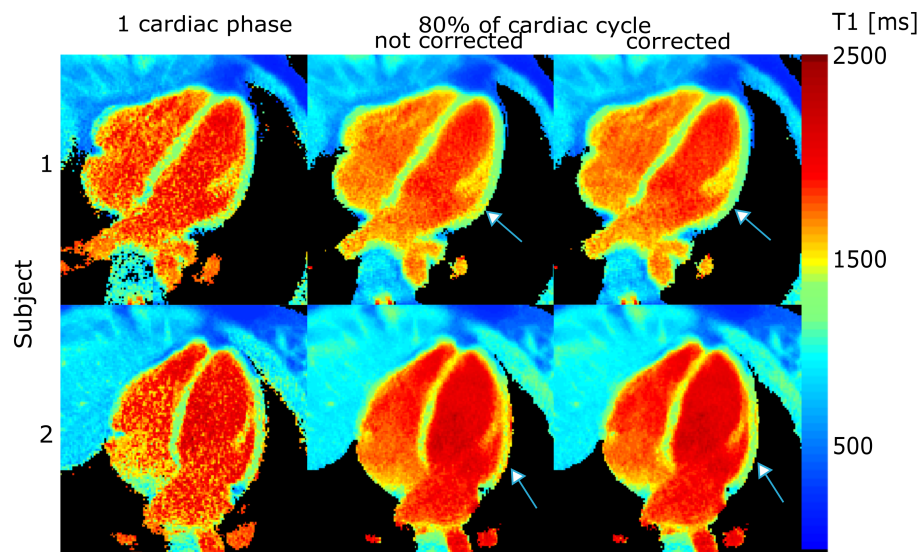


Figure 6.12: Native T_1 maps in 8 s and 4ChV. Cardiac motion corrected T_1 mapping is not restricted to short axis orientation. Motion corrected T_1 maps showed better T_1 mapping quality than uncorrected T_1 maps, especially in the lateral wall of the left ventricle (arrows). T_1 maps using 80% of the cardiac cycle showed visually a lower spatial variation of T_1 times compared to T_1^{1phase} mapping [J1].

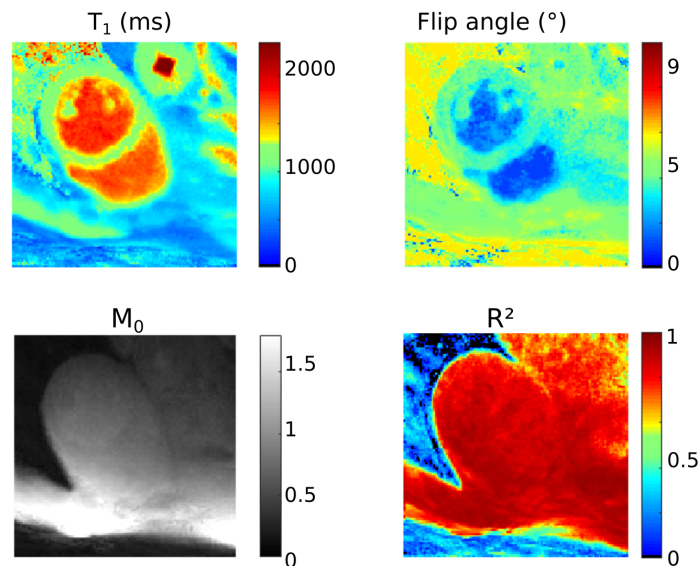


Figure 6.13: Maps of all estimated parameter. The flip angle in blood was smaller compared to myocardium, possibly because of compensation for inflow effects of spins which have not experienced rf-pulses before.

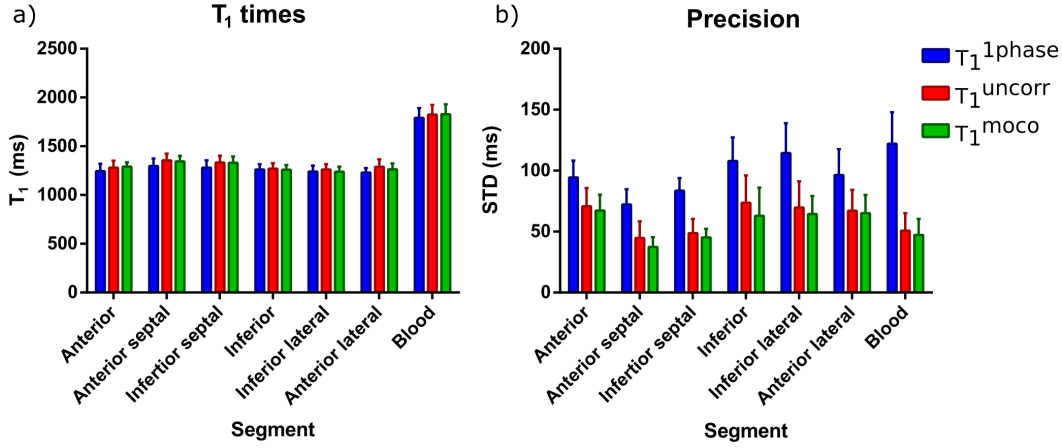


Figure 6.14: T_1 times and spatial variation of T_1 (STD) in 8 s. The error bars represent the mean values across the healthy subject and the intersubject variability. a) T_1 times in six myocardial segments and in the left ventricular blood pool of each segment. No significant differences in T_1 were found between the methods. b) The T_1 STD of the motion corrected T_1 (corresponding to the precision) was significantly lower in all segments compared to T_1 maps obtained with only one cardiac phase and motion uncorrected T_1 ($P < 0.0001$ and $P = 0.036$, respectively) [J1].

6.3.5 Impact of scan time on T_1 mapping

8 s T_1 maps were similar to 16 s T_1 maps (Figure 6.10). T_1 times of all segments averaged over all volunteers are shown in Figure 6.13a. No significant differences were found between 16 s T_1 times and 8 s T_1 times (1280 ± 50.61 ms and 1288 ± 48.68 ms, respectively, $P = 0.15$, Figure 6.13a,c). The STD of T_1^{moco} maps obtained in 16 s was lower than in T_1^{moco} maps obtained in 8 s (54.35 ± 6.31 ms and 57.05 ± 6.45 ms, respectively, $P = 0.026$, Figure 6.16b,d).

6.3.6 Repeatability of T_1 mapping

Two repeated T_1^{moco} maps in SAX were evaluated. Estimated deformation in each segment was comparable, with highest deformation in anterior and inferior segments (Figure 6.17) for both measurements. The highest deformation over all healthy subjects in the second measurement was 5.78 ± 1.49 mm in systole and 4.27 ± 1.24 mm, when excluding three systolic motion states. T_1 times of the whole myocardium did not differ significantly between the two measurements (1287 ± 49.98 ms and 1292 ± 50.50 ms, respectively, $P = 0.398$, Figure 6.18a). In spatial variation within the myocardium, no significant differences were found (58.57 ± 5.74 ms and 59.05 ± 6.90 ms, respectively, $P = 0.742$, Figure 6.18b).

6.4 Discussion

In this study, a novel cardiac motion corrected T_1 mapping approach was presented that provides robust high-resolution T_1 maps in a 8 s. Scan efficiency was increased by continuous data acquisition and correction for cardiac motion. Hereby, it was possible to use 80% of the total scan time for T_1 mapping instead of only about 20%. Thus, the amount of data used for T_1 mapping was increased by a factor of 5 compared to a cardiac-triggered T_1 mapping

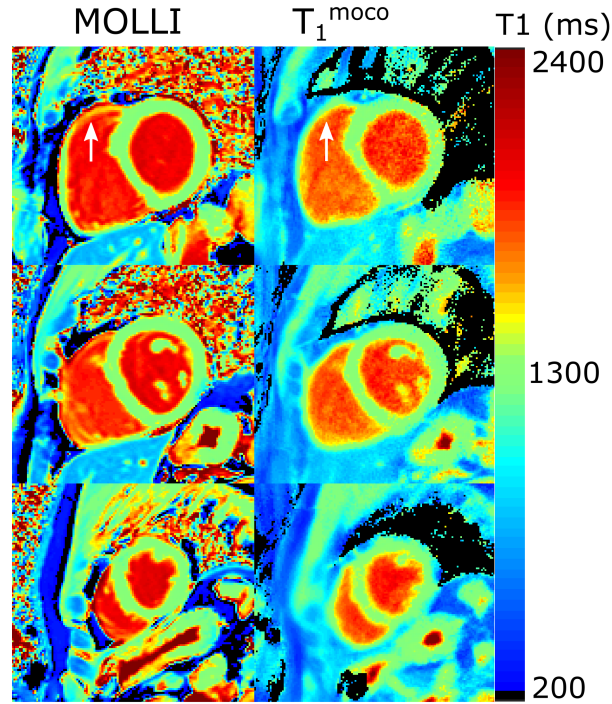


Figure 6.15: Stack of SAX slices. Comparison of MOLLI and motion corrected T_1 maps in a basal (upper row), mid-ventricular (middle) and apical (lower row) SAX slices. T_1^{moco} mapping was possible for all slices and visually comparable to MOLLI. The right ventricle was better defined in T_1^{moco} maps compared to MOLLI for all slices (arrows) [J1].

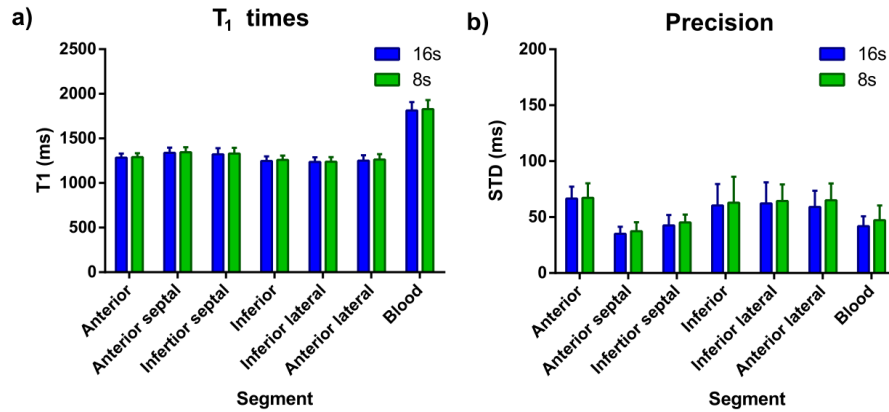


Figure 6.16: Impact of scan time on T_1 times (accuracy) and spatial variations of T_1 across the myocardium (precision). The error bars represent the mean across the healthy subjects and the intersubject variability. a) T_1 times in six myocardial segments and in the left ventricular blood pool of each segment for 16 s and 8 s. No significant differences were found. b) T_1 STD across healthy volunteers in six myocardial segments and in blood (mean \pm STD) for 16 s and 8 s. STD was significantly lower for 16 s compared to 8 s (54.35 ± 6.31 ms and 57.05 ± 6.45 ms, respectively).

6. NATIVE T_1 MAPPING USING CARDIAC MOTION CORRECTION

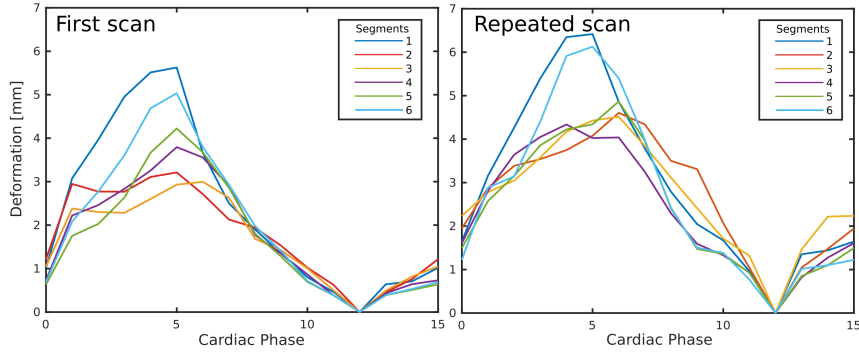


Figure 6.17: Repeatability of myocardial motion estimation. Deformation in each myocardial segment for both 8 s measurements. Deformation per cardiac phase was averaged over the volunteers. The trend was comparable between both measurements, with highest deformation in anterior and interior segments and maximum deformation in phase 5.

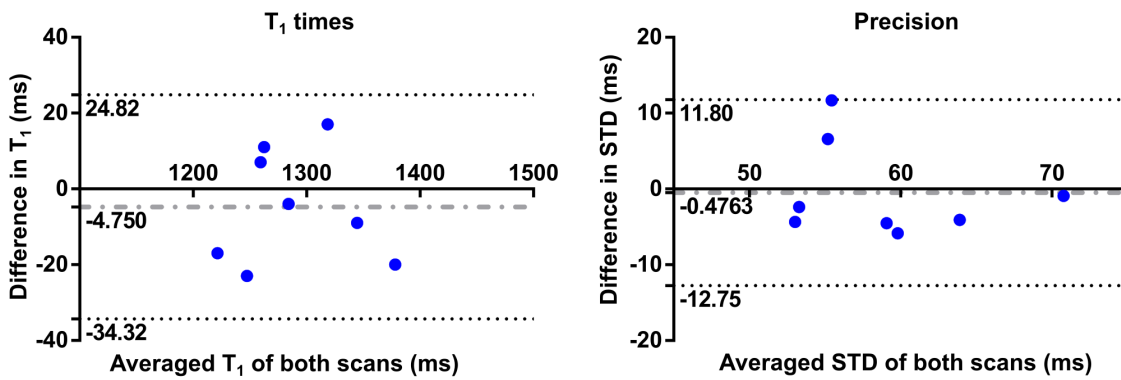


Figure 6.18: Repeatability of motion corrected T_1 mapping in 8 s, shown as Bland-Altman plot. Left: T_1 times, right: STD. Differences between both measurements in 8 volunteers, averaged over the whole myocardium were plotted against mean values of both measurements.

approach. Cardiac motion estimation was carried out from the same raw data used for T_1 mapping. An increase in precision compared to a cardiac triggered approach using only one specific motion state was demonstrated.

The STD of T_1 times in healthy myocardium is related to the precision of the measurement. By integration of motion correction, the precision of T_1 mapping was improved compared to T_1^{uncorr} mapping, which could be explained by less blurring in T_1^{moco} maps. Improved sharpness could be important for the detection of small epi- or endocardial fibrosis. T_1^{moco} mapping was robust, which can be seen by the repeatability study.

The individual TI images of T_1^{moco} and T_1^{uncorr} were reconstructed from data acquired in a 55 - 87 ms window compared to the 3 times longer window used for T_1^{1phase} mapping. Therefore, the TI images of T_1^{moco} and T_1^{uncorr} showed higher undersampling artifacts. Nevertheless, for the voxel-wise T_1 fit, 12 TI images per cardiac cycle were used for T_1^{moco} and T_1^{uncorr} rather than one for T_1^{1phase} . This led on average to 5.2 (4.3 - 6.8) times more data being utilized for the T_1^{moco} fitting. Due to the proposed golden-ratio-based radial acquisition, the undersampling artifacts between different TI images were incoherent along the recovery curve [75] and hence a robust T_1 fit was achieved leading to more reproducible T_1 times and an increase in precision by 34% compared to the standard T_1^{1phase} mapping.

In the phantom, our approach and MOLLI both estimated T_1 accurately. T_1 times obtained with T_1^{uncorr} , T_1^{moco} and T_1^{1phase} varied slightly but they were all within the range of previously published native T_1 times at 3 T. Compared to those studies, T_1 times were longer than MOLLI, which we also observed in our study, Shortened MOLLI and multitasking [125, 103, 73], but shorter than SASHA and SAPHIRE [15]. A study evaluating the precision of different T_1 mapping approaches showed a comparable precision in MOLLI and SAPHIRE (54.0 and 58.6 ms, respectively) and lower precision of SASHA compared to our approach (68.2 vs. 57.0 ms) [15]. However, comparison to other studies is difficult because of differences in acquisition and reconstruction settings as well as post-processing procedures, such as spatial filtering and the number of fit parameters, strongly affecting the precision [14].

Radial sampling is very robust in the presence of physiological motion. Therefore, good quality T_1 maps can also be obtained for T_1^{uncorr} mapping, especially for subjects with low heart rates. Figure 6.9 shows that for a volunteer with a heart rate of 46 bpm, removing 20% of the data in systole leads to TI images where the residual cardiac motion is below the spatial resolution of the images in more than 80% of the remaining cardiac phases. Therefore, the T_1 fit is mainly determined by these 80%, leading to a high quality T_1 map. For a volunteer with a heart rate in the normal range (66 bpm), removing 20% of data still leaves 60% of data with residual cardiac motion larger than the voxel size. In that case, T_1 fitting is impaired by cardiac motion and the obtained T_1 map shows severe motion artifacts because of motion state mismatches in TI images.

The separation of data into different cardiac phases both for the cine reconstruction and T_1 mapping was carried out retrospectively. The selection of the systolic phases to be removed prior to motion corrected T_1 fitting was done based on the results of the image registration rather than using a pre-defined delay time. Having the flexibility to retrospectively optimize the data selection can be especially important for arrhythmic patients in order to minimize errors due to ECG mistriggering [50].

6. NATIVE T_1 MAPPING USING CARDIAC MOTION CORRECTION

T_1^{moco} mapping has some limitations. In T_1 estimation, the inversion efficiency is not included in the signal model, which could lead to errors in T_1 [14]. Furthermore, through-plane motion occurs during the systolic phase of the cardiac cycle, which is not considered in the signal model for continuous acquisition (3.5) used for T_1 fitting (see chapter 3). Further investigation has to be performed on the influence of through-plane motion effects on the longitudinal magnetization during continuous acquisition. The time between inversions was fixed to 2276 ms for simplicity, which was optimized in chapter 3. A different time or varying intervals would possibly work as well, because of the dense sampling by using more TI images. For analysis, we have not carried out a blinded review of the image quality between uncorrected and corrected T_1 maps.

The T_1^{moco} mapping workflow is not fully automated yet. Two steps were performed manually. Firstly, for exclusion of three systolic cardiac phases, systole has to be selected. In this study, selection was based on the determined deformation vectors, averaged over the manually drawn myocardial segments. For automatization, a quantitative quality measure, such as the Quality Index proposed by Wang and Bovik [126] could be applied to cine images. This Quality index showed good preliminary results to detect systolic phases in our cine images. Secondly, a range around the heart was selected prior to motion estimation, to prevent motion estimation of static tissue and save computational time. Nevertheless, for automatization, the spatial range could possibly be increased to suit all subjects.

Estimated cardiac contraction during systole was 4.51 ± 0.98 mm averaged over the whole myocardium of the left ventricle in the 8 s acquisition, which is in the range of published deformations of the left ventricle (4.6 - 5.5 mm in a midventricular section) [81]. Small differences between repeated motion estimations suggest robustness of the estimation. While analyzing 16 s deformation fields of the same acquisition and the repeated 8 s measurement, systolic deformation was 5.28 ± 1.50 mm and 5.78 ± 1.49 mm, respectively. For deformation analysis, only the norm per voxel was investigated, but not the direction. Thus, the heart could move completely different, although showing the same deformation norm. Furthermore, myocardial segmentation has to be adjusted for the repeated scan, because of different breath hold positions. Therefore, the deformation vector norms are difficult to compare, but T_1^{moco} maps were similar between 16 s and 8 s as well as repeated 8 s measurement.

Motion estimation with this technique is not only restricted to cine images obtained in short axis orientation. Motion corrected T_1 mapping was also successful carried out in four chamber view. Here, especially visualization of the lateral wall was strongly improved using motion correction, which can be seen by more homogeneous T_1 times in the lateral wall than in T_1 mapping without motion correction. Also different software or techniques could be used for motion estimation in the future. For example, feature tracking could be implemented, which seems to be promising for the detection of cardiac motion [127]. However, the myocardium has to be contoured in this approach, which is not the case in NiftyReg. So far, motion transformation is performed in image space requiring interpolation which could lead to partial volume effects and residual blurring of image data. Nevertheless, cardiac motion correction could possibly be integrated in TI image reconstruction to further increase sharpness of the anatomy by iterative optimization of image quality [116].

Cine images showed constant contrast over all cardiac phases, although the contrast changed during magnetization recovery. The radial data acquisition ensures that combining raw data with different image contrasts leads to a high image quality with only small artifacts due to the inconsistencies in k-space caused by the contrast change.

In this study, motion was estimated in 2D, but the motion estimation algorithm can also be used for a 3D acquisition. This could be beneficial for structures with a high degree of through-plane motion, such as the papillary muscles and basal segments of the heart [81]. Therefore, a 3D acquisition could improve to detect complex cardiac motion. It could also help to reduce the scan time of a 3D T_1 mapping acquisition by improving the scan efficiency compared to proposed 3D T_1 mapping techniques [61, 63] and eventually allow for T_1 mapping of the entire heart in a clinically feasible scan time. Respiratory motion would have to be accounted as well, since a 3D acquisition would be too long for a breath hold. For that, a rigid motion correction could possibly be integrated where the k-space center could serve as navigator signal. Using a 3D acquisition, through-plane motion could be detected, and systolic cardiac phases would not have to be excluded, which would further increase scan efficiency.

T_1 maps obtained in 8 s did not show large differences in T_1 estimation compared to T_1 maps obtained in 16 s. For cine reconstruction, temporal regularization had to be adjusted, which can be easily implemented. T_1 times did not differ and the precision of 16 s T_1 maps is only 2.7 ± 3.2 ms higher compared to 8 s T_1 maps. Clinically, it is possibly more important to reduce the scan duration by 50% than increasing the spatial variation by only 2.7 ms. Therefore, it is not advantageous to choose the 16 s acquisition over the 8 s acquisition in clinical routine. The small differences in precision between 16 and 8 s show that the number of TI images (12 per cardiac cycle) is sufficient for T_1 mapping. To further increase the precision, the quality of TI images could be improved. TI images were reconstructed with iterative SENSE, without spatial or temporal filtering of the data. These images have severe streaking artifacts. Other advanced reconstruction techniques could have also been applied, such as compressed sensing, model-based reconstruction or low-rank methods to further improve image quality [116, 73, 65, 77, 66]. By integration of motion correction in image reconstruction, maybe 6 or 3 images could possibly be reconstructed per cardiac cycle instead of 12. This could be still enough to cover the relaxation curve and additionally, less streaking artefacts would be present in TI images, possibly positively influencing the spatial variation of T_1 times.

In only 8 s, an image resolution of 1.3×1.3 mm² was achieved. This short scan duration has the potential for the acquisition of two slices within a single breath hold, which would allow for the number of breath holds to be reduced in the clinical routine. In addition, the acquisition time could possibly also be further reduced. To investigate the impact of scan time, T_1 mapping was performed for acquisition times between 2 and 16 s of the same scan in one healthy subject. T_1 maps and T_1 times for myocardium and blood are shown in Figure 6.19. T_1 maps obtained in 16, 8, 6, 4 and 3 s were comparable, with nearly the same myocardial T_1 times (1300 - 1306 ms) and precision (38 - 43 ms). Visually, small details, such as the papillary muscles, could be depicted for all acquisition times between 3 s and 16 s. For 2 s, T_1 mapping was still possible, but precision was lower and thus, depiction of small details failed.

For all scan times, the same motion fields, estimated from a 16 s cine scan, were utilized. Therefore, the differences in T_1 maps were purely caused by data fitting. Usually, cine

6. NATIVE T_1 MAPPING USING CARDIAC MOTION CORRECTION

reconstruction and motion estimation are performed on exactly the same data as used for T_1 mapping. The main challenge in our motion estimation approach is the need for a constant contrast between the tissues. This constant contrast can only be achieved when data of multiple TIs are combined for each cardiac phase, because contrast is changing over the entire scan. A constant contrast cannot be guaranteed for short a scan duration. We also tested the minimal scan duration for cine reconstruction and motion estimation with the settings used in this work. For scan durations of 4 s or shorter, the contrast changes per cardiac phase and motion estimation was too strong for accurate motion estimation. This limits the applicability of our technique for shorter cardiac T_1 mapping acquisitions. Nevertheless, advanced motion estimation dealing with varying contrasts exist [57]. These techniques could be implemented in a future project and eventually, a complete workflow of cardiac motion corrected T_1 mapping in a scan time as short as 2 s could perhaps be feasible.

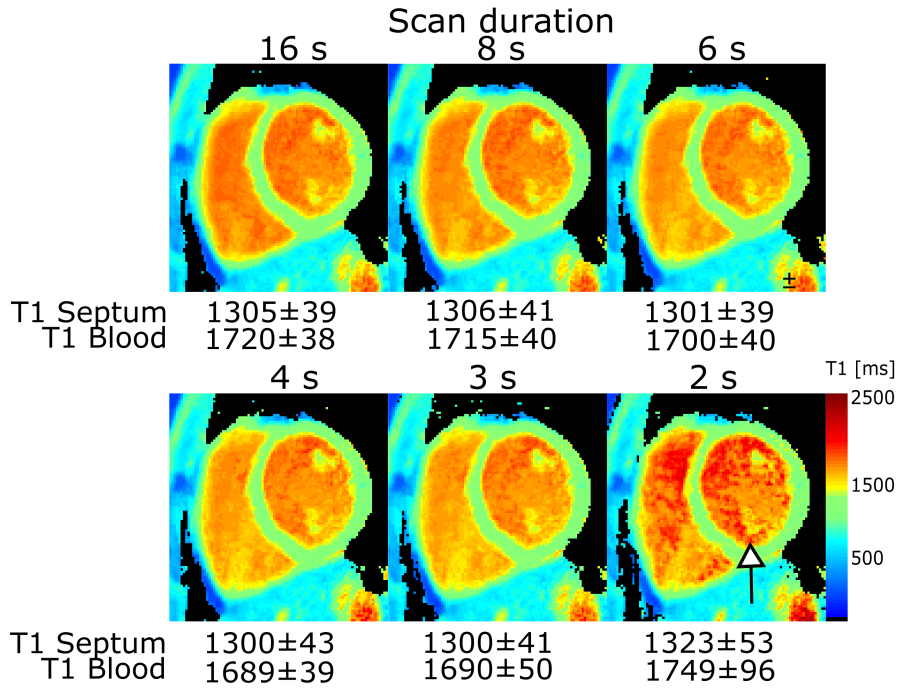


Figure 6.19: Impact of scan time on motion corrected T_1 mapping. For 3 – 16 s, T_1 times and precision within septum as well as blood were comparable. T_1 mapping quality was reduced for 2 s.

T_1 mapping was also possible for higher spatial resolutions, up to $0.8 \times 0.8 \text{ mm}^2$ in-plane and thus lower SNR (Figure 6.20), with an acquisition time of 16 s. For a SNR of 38% and 22% of the initial acquisition, small details were well visible in the T_1 maps, such as the inferior papillary muscle. For even higher resolutions, the myocardial wall of the RV is depicted accurately. Nevertheless, T_1 mapping quality is strongly reduced towards the lateral side of the LV. Precision was reduced in these T_1 maps and T_1 times decreased slightly with increasing spatial resolution. This could be explained by less partial volume effects for higher resolutions. Furthermore, T_1 mapping of the lateral part of the LV was not successful for voxel sizes as small as $0.8 \times 0.8 \times 4 \text{ mm}^3$ and $0.7 \times 0.7 \times 3 \text{ mm}^3$, which is caused by the coil arrangement around the thorax. M_0 is proportional to the distance to the coils. At the lateral site of the LV, M_0 is smallest and therefore, SNR is not high enough for accurate T_1 estimation.

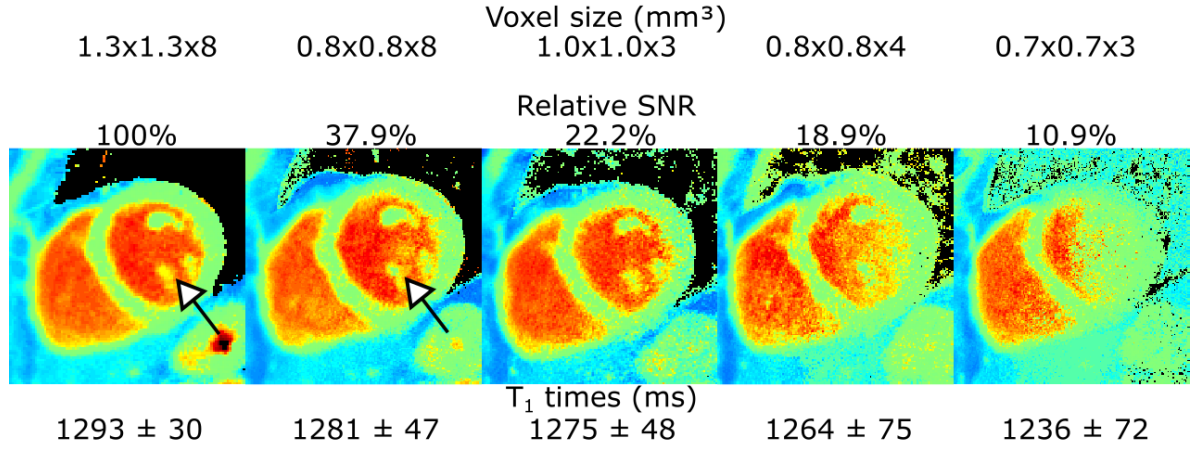


Figure 6.20: Motion corrected T₁ maps for different spatial resolutions. T₁ mapping was possible with reduced voxel size. Small details were better visible for higher resolutions (arrows), but T₁ mapping quality was reduced for voxel sizes of 19% and less of the initial voxel size. The color range is the same as in Figure 6.19. T₁ times and precision, expressed as STD of T₁ times within a ROI, were assessed in a manually drawn ROI over the whole septum.

6.5 Conclusion

Cardiac motion corrected T₁ mapping in 16 s and 8 was shown. Continuous data acquisition and the integration of cardiac motion correction improved the data acquisition efficiency by a factor of 5 compared to standard triggered cardiac T₁ mapping techniques. Scan time could be reduced to 8 s by remaining T₁ mapping quality. The increased efficiency resulted in more precise T₁ maps compared to T₁ mapping using only one cardiac phase (40% lower standard deviation in the myocardium). It was shown that spatial resolution could be increased to a sub-millimeter in-plane resolution of $0.8 \times 0.8 \text{ mm}^2$ and the scan duration could be reduced, because of higher scan efficiency compared to standard techniques. In this chapter, only healthy volunteers were included. However, only healthy subjects were included in this study. To test clinical feasibility, the approach has to be tested in patients with known myocardial pathologies.

Assessment of Myocardial Scar using post-contrast T_1 Mapping

Parts of this chapter have been presented in [J1]: Becker et al., Fast myocardial T1 mapping using cardiac motion correction, Magnetic Resonance in Medicine, 2020; vol. 83, pp. 438-451, which has been published in final form at <https://doi.org/10.1002/mrm.27935>.

7.1 Introduction

In tissue with focal fibrosis, T_1 times are shortened after contrast administration, because of retention of contrast agent within the extracellular space. Therefore, fibrosis can be depicted in post-contrast T_1 maps by lower T_1 times compared to healthy tissue. Furthermore, post-contrast T_1 maps are needed for the quantification of the ECV, which is an additional marker for myocardial tissue remodeling in a wide range of cardiac pathologies [128, 7, 129].

Qualitative LGE plays an important role in the assessment of myocardial viability. It has become the gold standard modality for the visualization of focal fibrosis in various ischaemic and non-ischaemic cardiomyopathies [37, 38, 39, 40]. Based on differences of contrast agent kinetics in non-fibrotic and fibrotic tissue, contrast between these structures is enhanced. Timing of the T_1 -weighted measurement is set such that fibrosis appears as hyperintense region in LGE images by imaging at zero-crossing for non-fibrotic tissue after an inversion.

In this study, model-based T_1 mapping (chapter 4) and cardiac motion corrected T_1 mapping (chapter 6) were applied for post-contrast T_1 mapping to investigate feasibility of our approaches for the detection of focal fibrosis. Both approaches were tested in five patients with suspected myocardial fibrosis after contrast agent administration. Post-contrast T_1 maps were compared with LGE images.

7. ASSESSMENT OF MYOCARDIAL SCAR USING POST-CONTRAST T_1 MAPPING

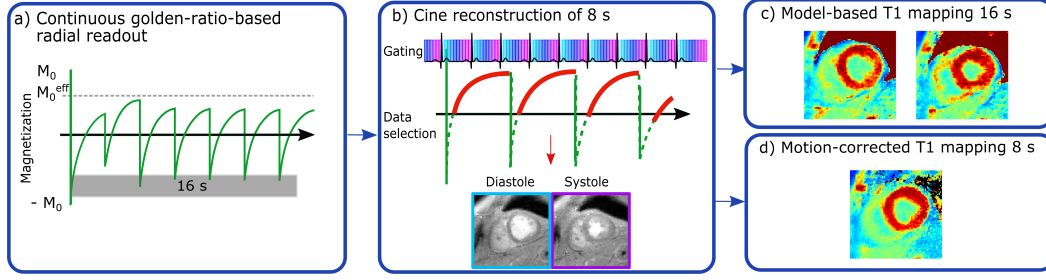


Figure 7.1: Data acquisition, cine imaging and T_1 mapping. a) Data is continuously acquired with radial golden-ratio-based read out. At constant times intervals, inversions were applied. b) Cine images with 15 cardiac phases were reconstructed prior to model-based T_1 mapping and motion corrected T_1 mapping (c and d).

7.2 Methods

7.2.1 Data acquisition and cine reconstruction

2D data acquisition was similar to the acquisition presented in chapter 3 (Figure 7.1a). For cine reconstruction, only the first 8 s of the data acquisition was utilized and the same reconstruction was used as described in chapter 6, yielding I_{Cine}^{1-15} (Figure 7.1b). In contrast enhanced imaging, only 200 ms after each inversion was excluded due to shorter T_1 times. Myocardial T_1 is longer than T_1 of blood because of the application of the contrast agent. Thus, the blood signal is higher than the myocardial signal, resulting in a bright blood contrast in the corresponding cine images. All image reconstruction was performed offline in MATLAB (The MathWorks, Inc., Natick, USA).

7.2.2 Iterative model-based T_1 mapping

Model-based T_1 mapping was performed using the entire 16 s acquisition. Data was binned based on the recorded ECG signal. Per cardiac cycle, a window length of 168 ms (34 lines) was selected for T_1 mapping. Diastolic T_1 maps were reconstructed by selecting end-diastole. For systolic T_1 mapping, delay time of systole was chosen based on the reconstructed cine images instead of a predefined delay time. T_1 maps were reconstructed using the same iterative model-based reconstruction technique as described in chapter 4.

7.2.3 Cardiac motion corrected T_1 mapping

All motion corrected T_1 mapping was performed on the first 8 s of the acquired data. Motion corrected T_1 mapping is explained in detail in chapter 4. Non-rigid motion estimated was performed on the bright-blood cine images obtained from the same measurement using NiftyReg [122], with a mid-diastolic cardiac phase as reference image. Diastolic motion corrected T_1 maps (T_1^{moco}) were obtained.

In this study, two additional T_1 maps were obtained based on the same raw data. To verify the influence of motion correction on post-contrast T_1 estimation, the same TI images were selected as above, but no motion was corrected prior to T_1 mapping, yielding T_1^{uncorr} maps. Besides this, the influence of the increased amount of k-space lines compared to standard

cardiac triggered T_1 mapping approaches was evaluated. For this, the same mid-diastolic data was selected within a single window as used in model-based T_1 mapping (T_1^{1phase}). All TI images were reconstructed with an iterative SENSE approach and quantitative maps were obtained by a 3-parameter fit, yielding M_0 , flip angle and T_1 .

7.2.4 In vivo experiments

To test feasibility of the approaches for the detection of fibrosis, five subjects with suspected focal fibrosis were scanned (3 female/2 male, aged 60.6 ± 8.4 years, height: 168.8 ± 9.7 cm, weight: 76.0 ± 12.1 , body mass index: 26.9 ± 5.2). The patients were included as part of the study Berlin Longterm Observation of Vascular Events (BeLOVE). The study was approved by the local ethic committee (EA1/066/17) and all subjects gave written informed consent. To detect focal fibrosis, a stack of SAX LGE phase-sensitive-IR images were acquired 15 minutes after contrast administration (0.15 mmol/(kg body weight) Gadoteridol) with the following scan parameter: flip angle: 20° , TE/TR: 1.56/4.10 ms, acquisition time: 10 heartbeats, spatial resolution: $2.1 \times 1.4 \times 7.0$ mm³, FOV: 350×263 mm², which was adapted to the patient. Post-contrast T_1 maps were obtained in the same orientation as the LGE image with best visibility of fibrosis when fibrosis was present. In case of no focal fibrosis, a mid-ventricular slice was acquired.

7.2.5 Evaluation of post-contrast T_1 mapping

Six mid-ventricular myocardial segments of the left ventricle, adapted from the American Heart Association consensus statement, and the left-ventricular blood pool were segmented [98]. Segmentation and evaluation were performed in MATLAB (The MathWorks, Inc., Natick, USA) and GraphPad Prism 6 (La Jolla, USA) and $P < 0.05$ was considered to be significant.

Model-based T_1 mapping

Post-contrast T_1 times and spatial variation of T_1 (STD) were assessed in all myocardial segments. The STD of T_1 times across a segment (spatial variability) was used to quantify the precision of the approach in subjects without focal fibrosis. Normal distribution of T_1 times and STDs were tested by a Shapiro-Wilk test. In both patients with visible focal fibrosis post-contrast T_1 times of the fibrotic segment were compared against T_1 times of all healthy segments using a Kruskal-Wallis test. Diastolic and systolic T_1 times and the STD of all healthy segment in all patients were compared by Wilcoxon signed-rank tests. Furthermore, a Bland-Altman analysis was performed for T_1 times and STD for all nonfibrotic subjects of the five patients.

Motion corrected T_1 mapping

To investigate the estimated motion, the deformation fields of each cardiac motion state were quantified in one subject. For the quantification, the norm of the 2D deformation vectors in each voxel were averaged over the six segments for each cardiac phase.

Post-contrast T_1 times and STD were assessed in all myocardial and blood segments. Normal distribution of T_1 times and STDs were tested by a Shapiro-Wilk test. Overall

7. ASSESSMENT OF MYOCARDIAL SCAR USING POST-CONTRAST T_1 MAPPING

differences in T_1 between the three methods were assessed by a comparison of mean T_1 times over all healthy segments of the 5 patients between T_1^{moco} , T_1^{1phase} and T_1^{uncorr} maps by a Friedman test with Dunn's multiple comparison correction.

Overall differences in STD between the three methods were assessed by a comparison of the STD over all healthy segments of the 5 patients between T_1^{moco} , T_1^{1phase} and T_1^{uncorr} maps by ANOVA with Bonferroni's multiple comparison correction. In both post-contrast T_1^{moco} maps with visible focal fibrosis, T_1^{moco} values of the fibrotic segment were compared against T_1 values of all healthy segments using a Kruskal-Wallis test.

7.3 Results

In post-contrast T_1 mapping, slices were oriented in basal and mid-ventricular short-axis orientations. In the LGE images, focal fibrosis was visible in two patients. In patient 2, focal fibrosis was depicted in a lateral segment and even small focal fibrotic spots were detected in the anterior segment of patient 3. Cine images had a consistent contrast over all cardiac phases. Cine images showed a bright-blood contrast (Figure 7.2), because of longer myocardial post-contrast T_1 times compared to blood. The window length of each cardiac bin was between 55 and 71 ms, depending on the heart rate (56 - 72 bpm).

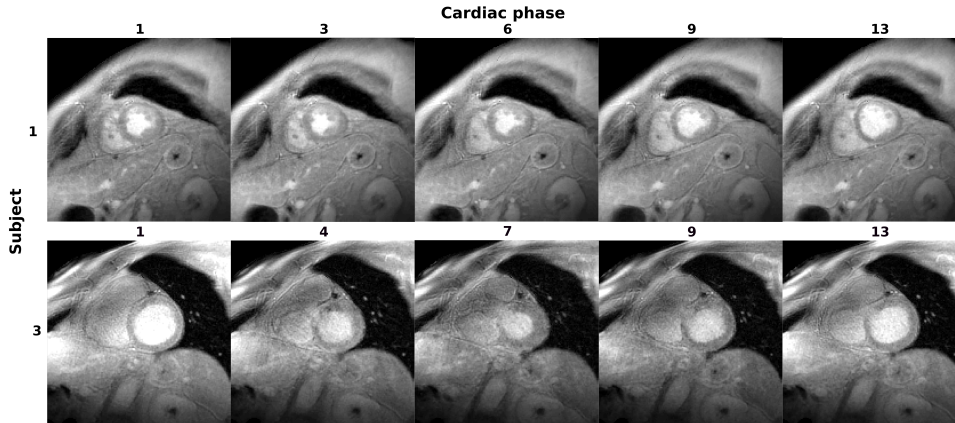


Figure 7.2: Post-contrast cine images from 8 s acquisition. Cine images showed a constant contrast bright-blood contrast over the cardiac cycle. a) Midventricular SAX orientation in a patient without fibrosis. b) Basal SAX orientation in a patient with focal fibrosis in the anterior segment. The left ventricular outflow tract is intersecting the slice in most of the cardiac phases.

7.3.1 Iterative model-based T_1 mapping

Model-based post-contrast T_1 mapping was successful for diastolic and systolic mapping (Figure 7.3). Focal fibrosis could be detected at the same location as in the LGE images. In segments with myocardial focal fibrosis, diastolic T_1 times were shorter compared to all segments without focal fibrosis in the same patient (patient 2: -72.00 ± 8.8 ms and patient 3: -68.2 ± 14.2 ms shorter compared to all healthy segments in the same patient ($P < 0.002$ for all segments)).

Differences in T_1 times and STD between diastolic and systolic T_1 maps can be found in the Bland-Altman plots of Figure 7.4. In healthy myocardial segments of all five patients, diastolic T_1 times were significantly shorter compared to systolic T_1 times (552.1 ± 68.0 ms and 592.6 ± 63.6 ms, respectively, $P < 0.001$), Figure 7.4,left). STD of diastolic T_1 maps were significantly lower than STD of systolic T_1 maps (32.4 ± 6.5 ms and 41.9 ± 14.1 ms, respectively, $P < 0.003$, Figure 7.4,right).

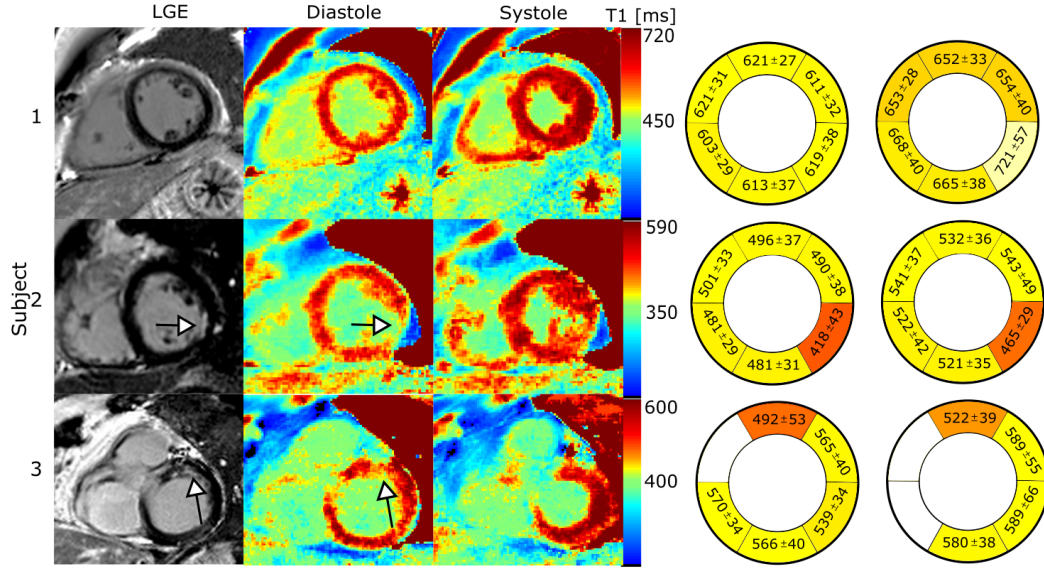


Figure 7.3: LGE images, model-based T_1 maps and bull's eye plots. Model-based reconstruction allowed for diastolic (middle) and systolic T_1 mapping (right). In subject 1, no focal fibrosis is present and T_1 times are homogeneous over the myocardium. In subject 2 and 3, focal fibrosis can be visually depicted in diastolic T_1 maps and fibrosis was confirmed by LGE images obtained at same slice position (arrows), with shortened T_1 times in the fibrotic tissue. Additionally, systolic T_1 times were assessed (right).

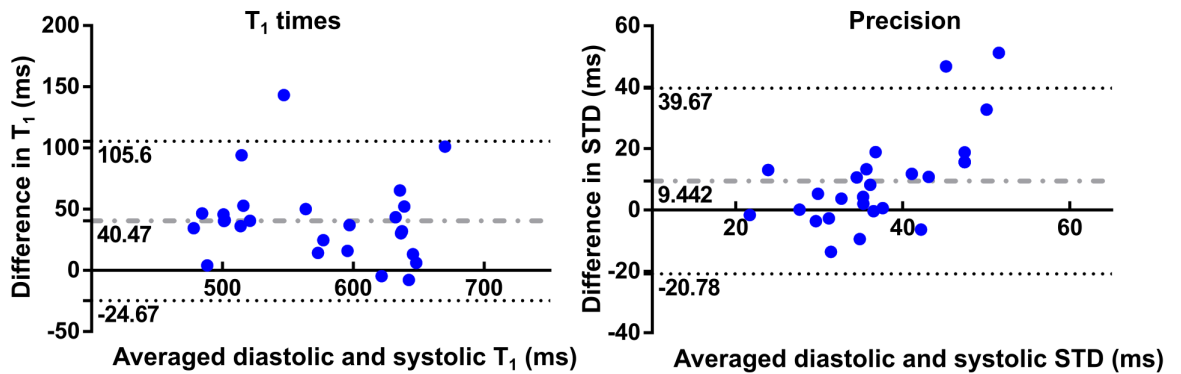


Figure 7.4: Bland-Altman analysis for diastolic and systolic T_1 and spatial variation. Systolic T_1 times were longer compared to diastolic T_1 times (left), with a bias of 40.47 ms, and STD of systolic T_1 maps was higher compared to diastolic T_1 maps leading to a reduced precision.

7.3.2 Motion corrected T_1 mapping

Determined highest deformation over the whole myocardium was 4.14 ± 0.88 mm in a mid-systolic phase (Figure 7.5). The deformation was comparable to estimated deformation in cine images without contrast administration (chapter 6, Figure 6.7). For visual analysis of motion estimation, motion fields (MF^{1-15}) were applied to the cine images ($MF^{1-15} \circ I_{Cine}^{1-15}$) in order to get motion corrected cine images. Motion estimation succeeded in all patients, with only small residual motion in motion corrected cine images (Figure 7.6).

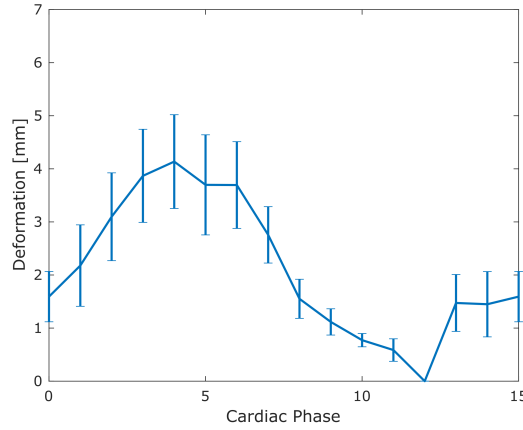


Figure 7.5: Estimated deformation of the left ventricle in post-contrast cine images. Deformation is presented as mean \pm STD value in mm over six segments per cardiac phase. The curve is comparable to deformation estimated in cine images without contrast administration (chapter 6, Figure 6.5).

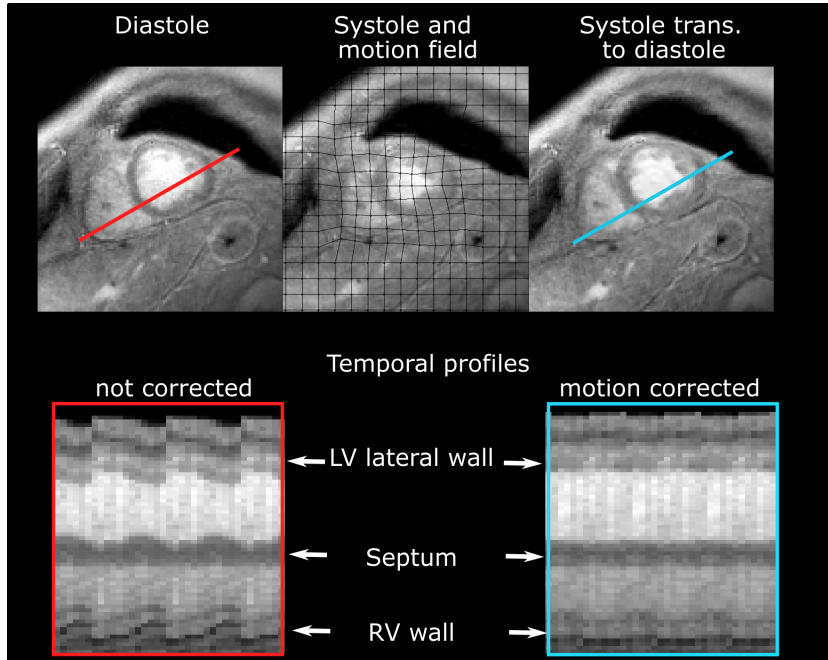


Figure 7.6: Cine images and motion correction after contrast administration. The deformation of the heart is estimated for a systolic image (middle) and motion is corrected (right) to match the reference mid-diastolic phase. The temporal slice profiles of cine images with and without motion correction are shown in the lower row (red and blue lines) [J1].

Post-contrast T_1 mapping was successful with the same acquisition as used in native T_1 mapping. In the subjects without focal fibrosis, T_1 times were homogeneous over the myocardium (7.7, subject 1). In post-contrast T_1^{uncorr} maps, different motion states of the TI images led to blurring of the myocardial border. In T_1^{moco} maps, the border between blood and myocardium was better defined and small fibrotic spots were visible. In T_1^{moco} maps, focal fibrosis could be detected at the same location as in the LGE images. In these spots, T_1 times were shorter compared to surrounding healthy tissue. In the two subjects with focal fibrosis, the averaged T_1^{moco} of the fibrotic segment were -69.5 ± 11.9 ms and -51.8 ± 12.0 ms shorter compared to all healthy segments in the same subject ($P < 0.002$ for all segments).

T_1 times are shown in Figure 7.8. T_1^{1phase} times were significantly longer (541.8 ± 56.5 ms) compared to T_1^{moco} and T_1^{uncorr} times (519.7 ± 60.1 ms, $P = 0.003$ and 511.7 ± 59.0 ms $P < 0.001$, respectively). T_1^{moco} times were longer compared to T_1^{uncorr} ($P = 0.013$). The STD in T_1^{1phase} maps (38.5 ± 7.6 ms) was higher compared to T_1 maps obtained with 80% of the cardiac cycle (T_1^{uncorr} : 24.6 ± 7.4 ms, T_1^{moco} : 21.2 ± 7.1 ms, $P < 0.0001$). STD of T_1^{moco} times were even lower compared to T_1^{uncorr} ($P = 0.008$), so precision was highest in T_1^{moco} maps.

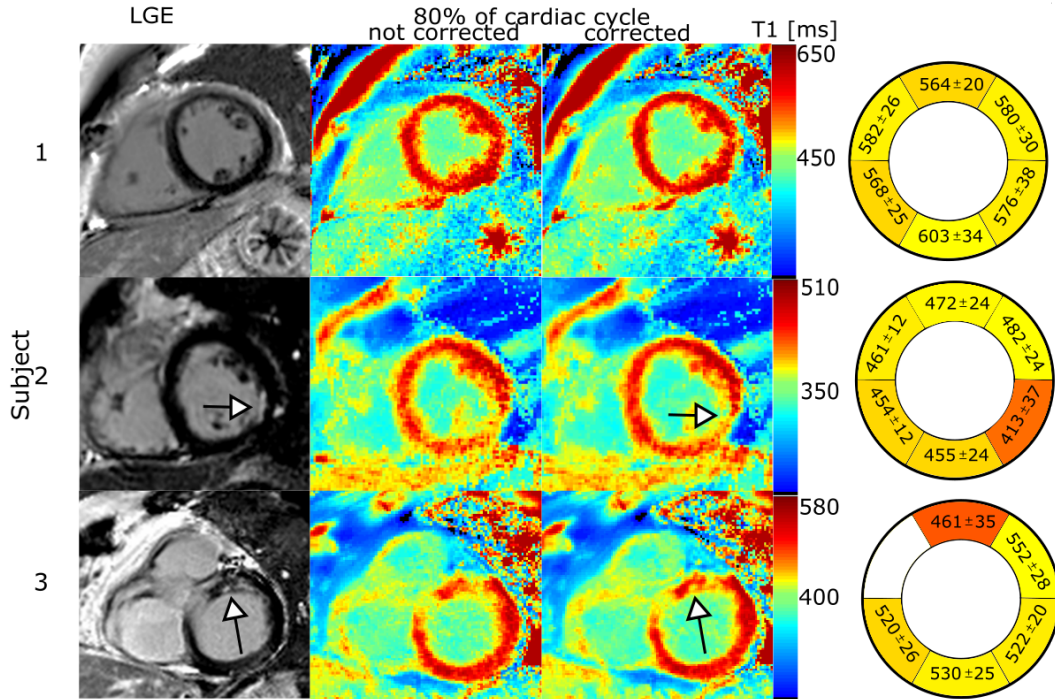


Figure 7.7: LGE images, motion corrected T_1 maps and bull's eye plots. The myocardium was more precisely defined in T_1^{moco} maps (right) compared to uncorrected T_1 maps (T_1^{uncorr} , middle). In subject 1, no focal fibrosis is present and T_1 times are homogeneous over the myocardium. In subject 2 and 3, focal fibrosis can be visually depicted in T_1^{moco} maps and confirmed by LGE images obtained at same slice position (arrows). In subject 2 and 3, T_1 times in the fibrotic segment were shorter compared to all healthy segments of the same subject (subject 2: -69.5 ± 11.9 ms and subject 3: -51.8 ± 12.0 ms, $P < 0.002$). In subject 3, the segment containing the left ventricular outflow tract was excluded in the analysis [J1].

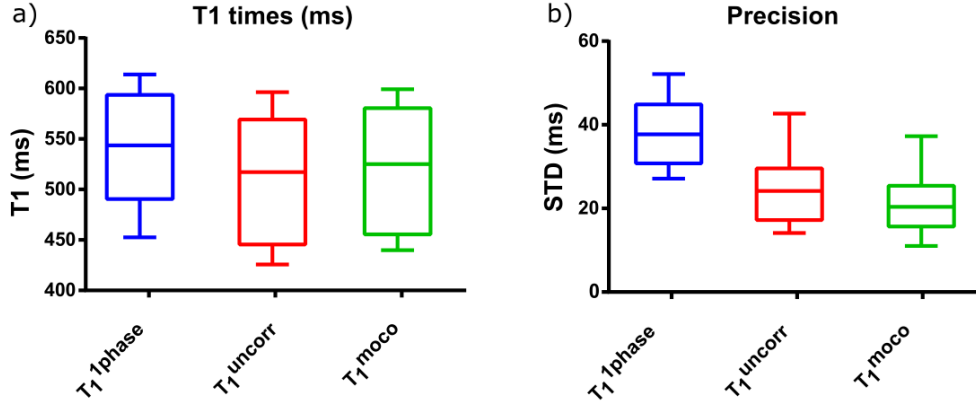


Figure 7.8: Box-Whisker plots of T_1 times and precisions over all patients. a) T_1 times of T_1^{1phase} , T_1^{uncorr} and T_1^{moco} averaged over all healthy segments of all patients. Post-contrast T_1 times have a high intersubject variability, which is demonstrated by the large boxes, due to contrast administration and timing of the measurement. b) STDs of T_1^{1phase} , T_1^{uncorr} and T_1^{moco} over all healthy segments of all patients. Precision of T_1^{1phase} is lower compared to T_1^{uncorr} and T_1^{moco} , comparable to native T_1 mapping presented in chapter 6.

7.4 Discussion

In this study, post-contrast T_1 mapping was shown using continuous data acquisition. Two different T_1 mapping approaches were evaluated. Model-based T_1 mapping yielded diastolic as well as systolic T_1 maps from the same acquisition. Cardiac motion corrected T_1 mapping approach was applied that provides T_1 maps in 8 s. Feasibility for the detection of focal fibrosis was demonstrated successfully.

In post-contrast T_1 maps, precision was improved by increasing the number of k-space lines to include data from 80% of each cardiac cycle and the integration of cardiac motion correction prior to T_1 mapping. Using motion correction, even small fibrotic spots were detectable that were less well defined in T_1^{uncorr} maps. Currently, LGE imaging is the gold standard for the detection of focal fibrosis. Diastolic post-contrast T_1 maps were in good agreement with LGE images in subjects with focal fibrosis. T_1 acquisition was oriented such that fibrotic myocardium was well visible in diastolic cardiac phases. Fibrotic spots were small in both patients and fibrosis was better visible in diastolic T_1 maps compared to systolic T_1 maps probably due to through-plane motion during systole. In model-based as well as motion corrected T_1 mapping, T_1 times in non-fibrotic segments across all five patients showed a high intersubject variability for healthy T_1 times (STD was 12.3% and 11.5%, respectively, error bars in Figure 7.8). This variation could be caused by different contrast agent concentration in the myocardium due to different measurement times after contrast administration.

Systolic T_1 times were longer than diastolic T_1 times. This difference could possibly be explained by a change in intra-myocardial blood volume during the cardiac cycle [130]. During systole, capillaries are contracted, leading to a small intra-myocardial blood volume, whereas in diastole, the myocardium is perfused for supply of nutrients and oxygen. A reduction in intra-myocardial blood volume could lead to an increase in T_1 , because of shorter T_1 in blood compared to myocardium. Furthermore, less partial volume effects could be present, especially in subjects with thin myocardial walls, additionally leading to higher T_1 times. However,

the effect was not found in native T_1 mapping using the same approach, where systolic T_1 times did not differ significantly from diastolic T_1 times in most segments (chapter 4). In native T_1 mapping, systolic T_1 would be shorter compared to diastolic T_1 as a result of lower intra-myocardial blood volume or less partial volume effects. The difference between T_1 in blood and myocardium in native as well as post-contrast T_1 mapping is about 30%, suggesting the same effect in both approaches.

Furthermore, T_1 times estimated by mapping using one cardiac phase were longer compared to T_1 times obtained by 12 cardiac phases, independent on model-based T_1 mapping or image-based T_1 mapping. For short T_1 times, longitudinal magnetization changes quickly after the first inversion. For this reason, it is important to use the contrast immediately after the inversion in order to estimate M_0 without having an additional M_0 image. In T_1 mapping using one cardiac phase, more k-space lines were used per TI image, which means that the contrast is averaged over a larger range of magnetization than in T_1 mapping using 12 TI images with only about 35% of k-space line per image. This difference could lead to variations in M_0 and T_1 estimation and should be further investigated. This could possibly also explain differences in diastolic and systolic T_1 mapping, since the start of the acquisition is triggered to diastole and thus, the first k-space lines were not utilized in systolic T_1 mapping.

Cine images were used for detection of systole in order to reconstruct systolic T_1 maps by model-based T_1 mapping and for cardiac motion estimation in motion compensated T_1 mapping. Cine images showed constant contrast over all cardiac phases, although the contrast changed during magnetization recovery. Unless cine images had a different contrast in comparison to non-contrast enhanced cine images obtained for native T_1 mapping, motion estimation succeeded with the same parameter settings as used for motion estimation based on non-contrast enhanced cine images. Furthermore, one slice was not positioned in mid-ventricular SAX orientation, but in basal orientation intersecting the left ventricular outflow tract. Also here, motion estimation was possible. Thus, motion estimation seems to be robust for a wide range of cine acquisitions, but need further investigation.

Also native T_1 mapping can be used to detect fibrosis. Nevertheless, for this study our T_1 mapping scan was part of a longer scan protocol and therefore only post-contrast T_1 mapping was applied for assessment of fibrosis. Data acquisition was carried out in the same slice location in which fibrosis was best visible in LGE images. This allowed for the best comparison with the gold standard LGE images.

For the calculation of the ECV, both native as well as post-contrast T_1 times are needed. For native T_1 mapping, exactly the same acquisition is applied as in post-contrast T_1 mapping (chapter 4 and 6) without any adjustment of scan settings. So far, in clinical routine different implementations of T_1 mapping methods are used for post-contrast T_1 mapping and native T_1 mapping, i.e. 4(1)3(1)2 and 5(3)3 sampling scheme for MOLLI. Inconsistencies between these implementations could lead to differences in T_1 estimation, since MOLLI is not accurate for a wide range of T_1 times. Eventually, this could result in errors in ECV calculation. By using our acquisition approach for post-contrast and native T_1 mapping no errors occur due to different implementations of T_1 mapping techniques.

7.5 Conclusion

In this study, post-contrast cardiac T_1 mapping within a single breath hold was shown. Model-based T_1 mapping was possible in 16 s for diastole and systole in all patients. Motion corrected T_1 mapping yielded diastolic T_1 maps within 8 s. The integration of cardiac motion correction improved precision of T_1 maps (45% lower standard deviation in the myocardium). Accurate detection of focal fibrosis in post-contrast T_1 maps was feasible using both techniques by decreased T_1 times compared to healthy myocardium. So far, both model-based T_1 mapping and cardiac motion corrected T_1 mapping were applied independently on the same data, but combining both methods could further increase T_1 mapping quality.

8

Combining model-based Reconstruction and cardiac motion corrected T_1 Mapping

8.1 Introduction

In chapter 4 and 6, two different T_1 mapping approaches have been presented. A model-based image reconstruction technique was introduced to reconstruct T_1 maps of highly undersampled data (chapter 4). Cardiac motion corrected T_1 mapping increased the scan efficiency by a factor of 5, yielding a spatial resolution of $1.0 \times 1.0 \times 3 \text{ mm}^3$ or a scan time reduction to 3 - 4 s (chapter 6). In this approach, only iterative SENSE reconstruction is used for the reconstruction of TI images. Model-based T_1 mapping as well as motion corrected T_1 mapping were based on the same data acquisition, so combining both approaches could further improve T_1 mapping quality.

In this chapter, cardiac motion correction and model-based image reconstruction were combined to further improve cardiac T_1 mapping quality and to reduce the scan time. For this, cardiac motion correction was implemented into model-based iterative T_1 reconstruction and evaluated in a healthy volunteer.

8.2 Methods

Motion correction was implemented in model-based iterative image reconstruction to further improve image quality for very short acquisition times. The workflow of the approach is shown in Figure 8.1 and contains the following steps (additional steps compared to the approach in chapter 4 are highlighted):

8. COMBINING MODEL-BASED RECONSTRUCTION AND CARDIAC MOTION CORRECTED T_1 MAPPING

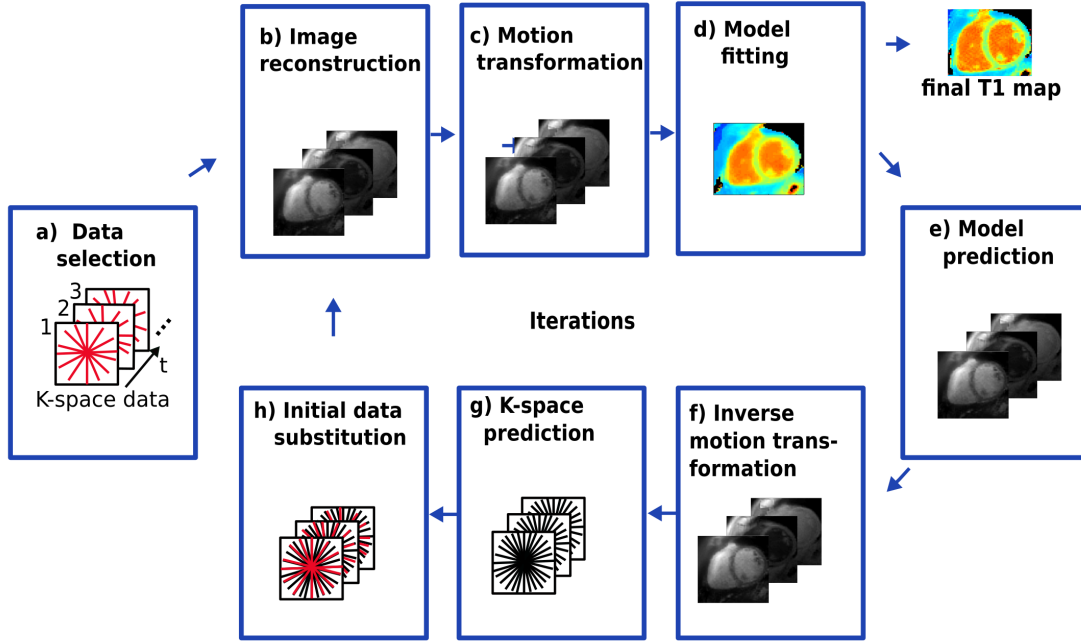


Figure 8.1: Methods of motion corrected model-based T_1 mapping. Motion correction was included into the model-based iterative T_1 reconstruction. Additional steps compared to the model-based reconstruction approach proposed in chapter 4 are shown in c) and f). Motion fields were applied to all TI images (c) prior to T_1 mapping and inverse motion fields were used to match the initial motion states in model TI images (f) before transforming image data back to k-space.

1. The k-space data was retrospectively gated in the same way as for motion corrected T_1 mapping and data of 12 out of 15 cardiac phases per cardiac cycle were used for image reconstruction.
2. The selected radial spokes of all cardiac cycles were interpolated onto Cartesian grids using GROG (Figure 8.1a) [94].
3. Coil sensitivities were estimated from all data combined [95].
4. TI images were reconstructed with an inverse FFT. (Figure 8.1b).
5. **Motion fields were applied to all TI images to match the reference motion state (Figure 8.1c).**
6. The magnitude TI images were fitted voxel-wise to the magnitude of the model function (Figure 8.1d). A three-parameter nonlinear least-squares fitting was implemented, yielding T_1 , M_0 and the flip angle of each voxel.
7. Based on T_1 , M_0 and the flip angle, for each of the time points, model TI images were calculated voxel-wise using the model function (Figure 8.1e).
8. **Inverse motion fields were applied to all model TI images to obtain the initial motion states (Figure 8.1f).**

9. The model T₁ images were multiplied by each coil sensitivity to account for the intensity variations. The resulting images were used to calculate model k-spaces by applying a FFT (Figure 8.1g).
10. Data consistency was ensured by substitution of the model predictions with the acquired k-space data (Figure 8.1h), which then serves as input for the next iteration.

Steps 4 to 10 were repeated until a fixed number of iterations. No spatial or temporal filtering was applied during reconstruction.

To test the approach for in vivo measurements, T₁ maps were reconstructed using the data from 6, with acquisition times of 4, 3 and 2 s. T₁ times and precision, in terms of spatial variation of T₁ times, were assessed in manually drawn ROIs covering the entire septum and the blood pool of the LV.

8.3 Results

T₁ maps obtained from motion corrected model-based T₁ reconstruction are shown in Figure 8.2. T₁ times of blood acquired in 2 to 4 s (1698 – 1724 ms) were comparable to 2 to 4 s motion corrected T₁ mapping without model-based reconstruction, but with an improved precision (21 – 26 ms compared to 39 – 96 ms). Myocardial T₁ times increased with increasing scan times, but differences were small (up to 2.5%). Precision in the myocardium (31 – 44 ms) was higher compared to motion corrected T₁ mapping (41 - 53 ms). Small details were visible in motion corrected model-based T₁ maps for all scan durations as short as 2 s.

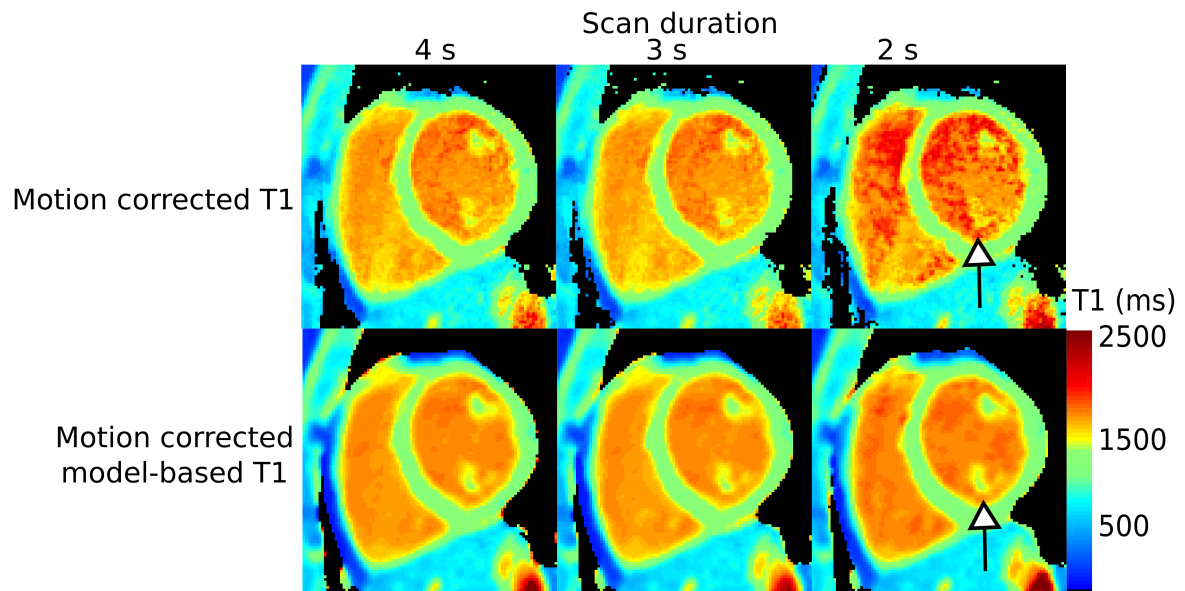


Figure 8.2: Motion corrected model-based T₁ maps. For comparison, T₁ maps using only motion correction are shown. Especially for a scan duration of 2 s, small features were better visible using the combined approach compared to only motion correction (arrows).

8. COMBINING MODEL-BASED RECONSTRUCTION AND CARDIAC MOTION CORRECTED T_1 MAPPING

	Scan duration	4 s	3 s	2 s
T_1 septum	motion corrected	1300	1300	1323
	motion corrected model-based	1299	1288	1267
T_1 blood	motion corrected	1689	1690	1749
	motion corrected model-based	1701	1698	1724
STD septum	motion corrected	43	41	53
	motion corrected model-based	35	31	44
STD blood	motion corrected	39	50	96
	motion corrected model-based	21	22	26

Table 8.1: T_1 times and precision of motion corrected model-based T_1 mapping for different scan durations. For comparison, T_1 times and precisions using only motion correction are shown. Fitted T_1 times were robust against reduction of scan time. Precision was increased by the use of motion corrected model-based T_1 mapping compared to motion correction only.

8.4 Discussion

In this study, a motion corrected model-based T_1 reconstruction method was presented and feasibility was shown in one healthy subject for scan durations of 2, 3 and 4 s. By combination of model-based image reconstruction (chapter 4) and motion corrected T_1 mapping (chapter 6), T_1 mapping was possible in a scan time as short as 2 s with higher precision compared to motion corrected T_1 mapping only.

As shown in chapter 6, Figure 6.19, it was possible to reduce the scan time to 3 s using only motion corrected T_1 mapping, but in T_1 maps obtained in 2 s, depiction of small details failed. Comparing motion corrected T_1 maps of 2 s (Figure 6.19) and 2 s T_1 maps using the combined approach (Figure 8.2), a clear improvement in image quality can be seen. The precision is higher, especially in blood, which is more difficult to fit in a short scan time, due to the longer T_1 times.

Here, for all scan times, the same motion fields, estimated from a 16 s cine scan, were utilized. Therefore, the differences in T_1 maps were purely caused by data fitting. Usually, cine reconstruction and motion estimation are performed on exactly the same data as used for T_1 mapping. This limits the applicability of our technique for shorter cardiac T_1 mapping acquisitions. One of the main limitations for a reduced scan time is the varying contrast in cine images. To overcome this problem, advanced motion estimation dealing with varying contrasts should be integrated [57]. Another possibility would be to integrate the motion-estimation into the iterative reconstruction process, dealing with T_1 recovery as well as deformation estimation. In this approach, motion could possibly be estimated on model TI images that are corrected for T_1 contrast.

For a scan duration of 4 s or shorter, the contrast changes per cardiac phase and motion estimation was too strong for accurate motion estimation.

The motion corrected model-based T_1 map of 2 s showed reasonable image quality with a spatial resolution of $1.3 \times 1.3 \times 8 \text{ mm}^3$. In addition, it was shown that T_1 mapping also worked for a higher spatial resolution using the earlier described methods and an acquisition time of 16 s (Figure 6.20). In future research, data with a high spatial resolution could be

reconstructed with the motion corrected model based T_1 mapping technique to reduce the scan time and to reach the limits of the presented approaches.

In general, a conclusion based on the obtained in vivo T_1 time and precision should not be drawn, because a gold standard is missing. The method should be further validated in phantom experiments. Without T_1 phantom including non-linear motion, arbitrary motion fields could be used to investigate the impact of multiple image deformations during the iterative process. Furthermore, more healthy subjects as well as patients with cardiomyopathies should be included. Data obtained in chapter 6 and 7 could be used for evaluation.

8.5 Conclusion

It was demonstrated that combination of motion corrected T_1 mapping and model-based iterative image reconstruction yielded T_1 maps in 2 s with high precision. Implementation of motion estimation algorithms based on images with varying contrast has to be further investigated, but the approach presented in this chapter could provide the basis for T_1 mapping of the entire heart with high isotropic image resolution, including the right ventricle and atria, within a clinically feasible scan time.

9

Summary

In this thesis, novel techniques have been developed to determine the tissue dependent relaxation time T_1 and to assess cardiac function using MRI in a fast and efficient way. The techniques ensure robust T_1 estimation and cardiac function assessment with high spatial resolution requiring only short acquisition times. In addition, cardiac motion correction was included for T_1 mapping to further reduce scan times by 50% without impairing image quality or quantification accuracy. This multiparametric approach is suitable for native as well as contrast-enhanced T_1 mapping. The approaches have been evaluated in numerical simulations, T_1 phantoms, healthy volunteers and patients with focal myocardial pathologies and were compared to standard cine images and MOLLI T_1 maps, one of the most frequently applied T_1 mapping technique in research and clinical settings.

A 2D acquisition scheme has been presented in chapter 3 for simultaneous acquisition of cardiac function and T_1 mapping. Integrated magnetization preparation pulses allow for robust T_1 estimation for a wide range of heart rates. Flowing blood and through-plane motion of the heart has only low impact on T_1 estimation caused by disruption of the continuous model function (max. 3.2% and 1.2%, respectively).

Model-based iterative image reconstruction for native cardiac T_1 mapping was introduced in chapter 4. This reconstruction approach used a model describing longitudinal magnetization during continuous acquisition and achieved accurate T_1 estimation from strongly undersampled data. Using this reconstruction, T_1 mapping of arbitrary cardiac phases was possible. Furthermore, it was shown that unlike other myocardial T_1 mapping methods, continuous data sampling provides additional information of cardiac function, comparable to standard cine scans. Functional information could be used to better determine the quiescent phase of the heart allowing for more data to be used per heart cycle (about 30%). The additional data enabled T_1 mapping with higher spatial resolution visualizing thin myocardial walls of the right ventricle and both atria in native T_1 maps (chapter 5).

In order to further improve the acquisition efficiency in cardiac T_1 mapping, a second T_1 mapping technique was proposed using cardiac motion correction. Here, functional information was used to estimate cardiac motion and to correct for cardiac motion prior to T_1 mapping of

9. SUMMARY

the same scan (chapter 6). Especially in cardiac T_1 mapping, the multiparametric acquisition has the advantage that no mismatch between cine images and T_1 maps exists which could be caused by different breath-holding positions and thus, no image registration is needed between cine images and TI images. In this approach, native T_1 mapping was performed using 80% of each heart cycle for data acquisition, in contrast to 15% in standard approaches. The improved scan efficiency allowed for high quality T_1 mapping with increased spatial resolution (up to $0.8 \times 0.8 \text{ mm}^2$ in-plane). The integration of motion correction in a model-based reconstruction could strongly reduce scan time (chapter 8), obtaining T_1 with spatial resolution of $1.3 \times 1.3 \times 8.0 \text{ mm}^3$ and high precision in a scan time as short as 2 s.

A pilot study showed first clinical feasibility of both approaches in patients with focal scar with contrast enhanced T_1 mapping. Although the contrast between blood and myocardium is changing compared to non-contrast enhanced cine images, motion could be estimated, and focal scar could be depicted by contrast-enhanced T_1 mapping (chapter 7).

One of the main challenges of the presented approaches is reconstruction time. All data is acquired using radial trajectories. Therefore, non-Cartesian reconstruction has to be performed, which is computationally more demanding than standard Cartesian reconstruction. In model-based reconstruction, the reconstruction time is longer (in the range of minutes to hours, depending on spatial resolution and number of iterations) compared to usual non-Cartesian parallel image reconstruction as performed in cardiac motion corrected T_1 mapping. However model-based reconstruction provides additional clinically relevant information because T_1 mapping can be performed for arbitrary cardiac phases from one acquisition. Identifying changes of myocardial T_1 times in diastole as well as systole could provide higher diagnostic certainty. Furthermore, qualitative TI images with a high image quality were reconstructed as additional output during the iterative process, which are also important for clinical examinations to detect image artefacts that are not well visible in T_1 maps. No effort was made so far for minimization of computational time, but it could be for example reduced by implementation of GPU routines for non-uniform fast Fourier transform and T_1 fitting.

In principle, cardiac T_1 mapping using both approaches is not restricted to radial trajectories and gradient echo read out. The approach would gain clinical relevance by acquisition with bSSFP read out because higher SNR that is needed for lower field strength, since nowadays most clinical MRI examinations are performed on a 1.5 Tesla scanner. However, this implementation comes with challenges, such as magnetization transfer effect and T_2 dependencies [14]. These effects have to be included into the model function and preliminary results can be found in [C1]. Other trajectories that provide frequent coverage of low frequencies would be suitable for multiparametric imaging, such as spiral trajectories with golden radial ratio between two consecutive read outs, providing more information per read out line than radial spokes. Another option would be pseudo-random sampling along phase encoding, where compressed sensing with higher sampling rate of low frequencies for a good determination of the longitudinal magnetization during magnetization recovery and motion of the heart could be used instead of iterative SENSE reconstruction for faster image reconstruction.

Combining both approaches allowed for even further reduction of scan time (chapter 8). However, handling of the large amount of data during reconstruction is challenging. Therefore, the combination of both approaches was only evaluated with data of max. 4 s and a spatial

resolution of $1.3 \times 1.3 \times 8 \text{ mm}^3$. Further research into more data efficient techniques is required in order to make this approach applicable in a more general way. Maybe this problem could be tackled by data handling similar to low-rank reconstruction techniques [131].

In this study, clinical feasibility was tested for focal myocardial fibrosis, but in order to distinguish between healthy and pathological myocardium in diffuse cardiomyopathies, normal ranges of cardiac T_1 times need to be defined for each T_1 mapping method in order to integrate the techniques in clinical routine. T_1 times of healthy tissue can only be assessed in a large study with healthy volunteers, due to inter-subject variability of T_1 times in healthy tissue and to facilitate a broad implementation of the novel techniques [103].

The multiparametric approach allowed for cine imaging and T_1 mapping. The main idea was to replace cine imaging by that approach in clinical routine to get a clinically cine scan, and the additional information of T_1 . Cine imaging is a standard acquisition performed in all clinical examinations. Whereas T_1 maps can be inspected after examination, immediate visualization of cine images is important for planning of further scans needed within the examination. Therefore, a long reconstruction time for each slice is the main limitations of the multiparametric approach for clinical routine. Novel image reconstruction methods based on machine learning approaches may allow for fast online reconstruction of the data [132].

Due to the long acquisition times, T_1 mapping is carried out for a few selected slice positions in clinical practice. Without whole-heart coverage, it is very likely that focal spots of scar tissue are missed. Multislice and 3D approaches for T_1 mapping have been proposed, but lead to long scan times or only achieve low spatial resolution [61, 63, 119]. This makes it difficult to implement these approaches into clinical routine. Here we demonstrated that cardiac T_1 mapping for a high-resolution 2D slice would be possible in 2 s. Within one breathhold not just one but several 2D slices could be acquired without loss in spatial resolution. This could be a first important step for future research to achieve 3D high-resolution T_1 mapping of the whole heart.

CMR allows for non-invasive examination of the heart, including various diagnostic parameter obtained in subsequent scans. T_1 mapping is a promising technique for early detection of diffuse myocardial changes in many diseases involving the heart. Furthermore, quantitative imaging modalities allow for studying disease progression and treatment response over a long period of time. CMR has been challenging so far, because of inefficient acquisition strategies leading to long examination times. The imaging approaches proposed in this thesis have been demonstrated to hold great promise for fast and simultaneous acquisition of multiple clinically relevant parameter by efficient data sampling and advanced image reconstruction methods. Multiparametric approaches including quantitative imaging could be important for future directions in CMR including vendor-independent contrast-free examinations and a patient and personnel friendly scan wherein various clinically necessary parameter are acquired simultaneously.

References

- [1] Aktueller Deutscher Herzbericht. *Erfolgreiche Herzmedizin: Herzinfarktsterblichkeit stark gesunken – kardiologische Versorgung auf hohem Niveau*. 2014. URL: <http://www.herzstiftung.de/pdf/presse/herzbericht-2014-dgk-pm.pdf>.
- [2] Amit R. Patel and Christopher M. Kramer. “Role of Cardiac Magnetic Resonance in the Diagnosis and Prognosis of Nonischemic Cardiomyopathy”. In: *JACC: Cardiovascular Imaging* 10.10 (2017), pp. 1180–1193.
- [3] Steffen Bohl and Jeanette Schulz-Menger. “Cardiovascular Magnetic Resonance Imaging of Non-ischaemic Heart Disease: Established and Emerging Applications”. In: *Heart, Lung & Circulation* 19.3 (2010), pp. 117–32.
- [4] Florian Von Knobelsdorff-Brenkenhoff and Jeanette Schulz-Menger. “Cardiovascular Magnetic Resonance Imaging in Ischemic Heart Disease”. In: *Journal of Magnetic Resonance Imaging* 36 (2012), pp. 20–38.
- [5] Christopher M Kramer. “Role of Cardiac MR Imaging in Cardiomyopathies”. In: *Journal of Nuclear Medicine* 56 (2015), 39S–45S.
- [6] Peter Kellman and Andrew E Arai. “Cardiac imaging techniques for physicians: late enhancement”. In: *Journal of Magnetic Resonance Imaging* 36.3 (2012), pp. 529–542.
- [7] Philip Haaf et al. “Cardiac T1 Mapping and Extracellular Volume (ECV) in clinical practice: a comprehensive review”. In: *Journal of Cardiovascular Magnetic Resonance* 18.89 (2016).
- [8] Andrew J. Taylor et al. “T1 Mapping: Basic Techniques and Clinical Applications”. In: *JACC: Cardiovascular Imaging* 9.1 (2016), pp. 67–81.
- [9] Jeremy R Burt et al. “Myocardial T1 mapping: techniques and potential applications.” In: *Radiographics: a review publication of the Radiological Society of North America, Inc* 34.2 (2014), pp. 377–95.
- [10] Pan Ki Kim et al. “Myocardial T1 and T2 Mapping: Techniques and Clinical Applications”. In: *Korean journal of radiology* 18.1 (2017), pp. 113–131.
- [11] Ntobeko A.B. Ntusi et al. “Diffuse Myocardial Fibrosis and Inflammation in Rheumatoid Arthritis: Insights From CMR T1 Mapping”. In: *JACC: Cardiovascular Imaging* 8.5 (May 2015), pp. 526–536.

REFERENCES

- [12] Ntobeko A B Ntusi et al. “Subclinical myocardial inflammation and diffuse fibrosis are common in systemic sclerosis - a clinical study using myocardial T1-mapping and extracellular volume quantification”. In: *Journal of cardiovascular magnetic resonance* 16.21 (2014).
- [13] Valentina O. Puntmann et al. “Native T1 Mapping in Differentiation of Normal Myocardium From Diffuse Disease in Hypertrophic and Dilated Cardiomyopathy”. In: *JACC: Cardiovascular Imaging* 6.4 (Apr. 2013), pp. 475–484.
- [14] Peter Kellman and Michael S Hansen. “T1-mapping in the heart: accuracy and precision”. In: *Journal of Cardiovascular Magnetic Resonance* 16.2 (2014).
- [15] Sebastian Weingärtner et al. “Myocardial T1-mapping at 3T using saturation-recovery: reference values, precision and comparison with MOLLI”. In: *Journal of Cardiovascular Magnetic Resonance* 18.84 (2016).
- [16] Sébastien Roujol et al. “Accuracy, precision, and reproducibility of four T1 mapping sequences: A head-to-head comparison of MOLLI, ShMOLLI, SASHA, and SAPHIRE”. In: *Radiology* 272.3 (2014), pp. 683–689.
- [17] Elaine N Marieb and Katja Hoehn. *Human Anatomy & Physiology*. 9th ed. Pearson, 2013.
- [18] Dee Unglaub Silverthorn. *Human physiology: an integrated approach*. Ed. by San Francisco. 5th ed. Pearson, 2010, pp. 828–867.
- [19] Nadine Kawel et al. “Normal left ventricular myocardial thickness for middle aged and older subjects with SSFP cardiac MR: The Multi-Ethnic Study of Atherosclerosis”. In: *Circulation Cardiovascular Imaging* 5.4 (2012), pp. 500–508.
- [20] Siew Yen Ho and P. Nihoyannopoulos. “Anatomy, echocardiography, and normal right ventricular dimensions”. In: *Heart* 92 (2006), pp. i2–i13.
- [21] Marta Varela et al. “3D high-resolution atrial wall thickness maps using black-blood PSIR”. In: *Journal of Cardiovascular Magnetic Resonance* 17.P239 (2015).
- [22] Arthur C. Guyton and John e Hall. *Textbook of Medical Physiology*. January. 2006, pp. 86–89.
- [23] Shuo Zhang et al. “Real-time magnetic resonance imaging of cardiac function and flow-recent progress.” In: *Quantitative Imaging in Medicine and Surgery* 4.5 (2014), pp. 313–329.
- [24] Andrew C Larson et al. “Self-gated cardiac cine MRI”. In: *Magnetic resonance in medicine* 51.1 (Jan. 2004), pp. 93–102.
- [25] Grace M Nijm et al. “Comparison of self-gated cine MRI retrospective cardiac synchronization algorithms”. In: *Journal of magnetic resonance imaging* 28.3 (2008), pp. 767–772.
- [26] G L Nayler, D N Firmin, and D B Longmore. “Blood Flow Imaging by Cine Magnetic Resonance”. In: *Journal of Computer Assisted Tomography* 10.5 (1986), pp. 715–722.

-
- [27] Nathan Mewton et al. "Assessment of Myocardial Fibrosis With Cardiovascular Magnetic Resonance". In: *Journal of the American College of Cardiology* 57.8 (2011), pp. 891–903.
 - [28] Rahul H. Rathod, Andrew J. Powell, and Tal Geva. "Myocardial Fibrosis in Congenital Heart Disease". In: *Circulation Journal* 80.6 (2016), pp. 1300–1307.
 - [29] Wolter L. de Graaf et al. "Contrast-Enhanced T1-Mapping MRI for the Assessment of Myocardial Fibrosis". In: *Current Cardiovascular Imaging Reports* 7.4 (2014), pp. 1–12.
 - [30] Deborah H. Kwon Christine L. Jellis. "Myocardial T1 mapping- modalities and clinical applications". In: *Cardiovasc Diagn Ther* 4.2 (2014), pp. 126–137.
 - [31] Eugenio Picano et al. "In vivo quantitative ultrasonic evaluation of myocardial fibrosis in humans." In: *Circulation* 81 (1990), pp. 58–64.
 - [32] Jason Pellman, Jing Zhang, and Farah Sheikh. "Myocyte-Fibroblast Communication in Cardiac Fibrosis and Arrhythmias: Mechanisms and Model Systems". In: *Journal of Molecular and Cellular Cardiology* 94 (2016), pp. 22–31.
 - [33] Paul Knaapen et al. "Perfusable tissue index as a potential marker of fibrosis in patients with idiopathic dilated cardiomyopathy." In: *Journal of Nuclear Medicine* 45.8 (2004), pp. 1299–1304.
 - [34] M P M Graham-Brown et al. "Imaging of Myocardial Fibrosis in Patients with End-Stage Renal Disease: Current Limitations and Future Possibilities". In: *BioMed Research International* (2017), p. ID 5453606.
 - [35] Maike Baues et al. "Fibrosis imaging: Current concepts and future directions". In: *Advanced drug delivery reviews* 121 (2017), pp. 9–26.
 - [36] Peter Kellman et al. "Extracellular volume fraction mapping in the myocardium, part 1: evaluation of an automated method". In: *Journal of Cardiovascular Magnetic Resonance* 14.63 (2012).
 - [37] Raymond J Kim et al. "The Use of Contrast-Enhanced Magnetic Resonance Imaging to Identify Reversible Myocardial Dysfunction". In: *New England Journal of Medicine* 343.20 (2000), pp. 1445–1453.
 - [38] Ankur Gulati et al. "Association of Fibrosis With Mortality and Sudden Cardiac Death in Patients With Nonischemic Dilated CardiomyopathyFibrosis and Prognosis in Dilated Cardiomyopathy". In: *JAMA* 309.9 (2013), pp. 896–908.
 - [39] Steffen Bohl et al. "Delayed enhancement cardiac magnetic resonance imaging reveals typical patterns of myocardial injury in patients with various forms of non-ischemic heart disease". In: *International Journal of Cardiovascular Imaging* 24.6 (2008), pp. 597–607.
 - [40] Peter Hunold et al. "Myocardial Late Enhancement in Contrast-Enhanced Cardiac MRI: Distinction Between Infarction Scar and Non-Infarction-Related Disease". In: *American Journal of Roentgenology* 184.May (2005), pp. 1420–1426.

REFERENCES

- [41] Olurotimi Mesubi, Kelechi Ego-Osuala Jean, and James Jeudy. “Differences in quantitative assessment of myocardial scar and gray zone by LGE-CMR imaging using established gray zone protocols”. In: *International Journal of Cardiovascular Imaging* 31 (2015), pp. 359–368.
- [42] Christopher T Sibley et al. “T1 Mapping in cardiomyopathy at cardiac MR: comparison with endomyocardial biopsy”. In: *Radiology* 265.3 (2012), pp. 724–732.
- [43] Erik B Schelbert et al. “Myocardial extravascular extracellular volume fraction measurement by gadolinium cardiovascular magnetic resonance in humans: slow infusion versus bolus”. In: *Journal of Cardiovascular Magnetic Resonance* 13.16 (2011).
- [44] Timothy C Wong et al. “Association Between Extracellular Matrix Expansion Quantified by Cardiovascular Magnetic Resonance and Short Term Mortality”. In: *Circulation* 126.10 (2012), pp. 1206–1216.
- [45] D C Look and D R Locker. “Time Saving in Measurement of NMR and EPR Relaxation Times”. In: *Review of Scientific Instruments* 41.2 (1970), pp. 250–251.
- [46] Daniel R. Messroghli et al. “Modified look-locker inversion recovery (MOLLI) for high-resolution T 1 mapping of the heart”. In: *Magnetic Resonance in Medicine* 52 (2004), pp. 141–146.
- [47] Kelvin Chow et al. “Saturation recovery single-shot acquisition (SASHA) for myocardial T1 mapping”. In: *Magnetic Resonance in Medicine* 71.6 (2014), pp. 2082–2095.
- [48] Darius Dabir et al. “Reference values for healthy human myocardium using a T1 mapping methodology: results from the International T1 Multicenter cardiovascular magnetic resonance study.” In: *Journal of Cardiovascular Magnetic Resonance* 16.69 (2014).
- [49] Sebastian Weingaertner et al. “Combined Saturation / Inversion Recovery Sequences for Improved Evaluation of Scar and Diffuse Fibrosis in Patients with Arrhythmia or Heart Rate Variability”. In: *Magnetic Resonance in Medicine* 71 (2014), pp. 1024–1034.
- [50] Nadja M. Messner et al. “Saturation-Recovery Myocardial T1-Mapping during Systole: Accurate and Robust Quantification in the Presence of Arrhythmia”. In: *Scientific Reports* 8.1 (2018), p. 5251.
- [51] Carlo Tessa et al. “Myocardial T1 and T2 mapping in diastolic and systolic phase”. In: *International Journal of Cardiovascular Imaging* 31.5 (2015), pp. 1001–1010.
- [52] Vanessa M Ferreira et al. “Systolic ShMOLLI myocardial T1-mapping for improved robustness to partial-volume effects and applications in tachyarrhythmias”. In: *Journal of Cardiovascular Magnetic Resonance* 17.77 (2015).
- [53] Benjamin Marty et al. “Bloch equations-based reconstruction of myocardium T1 maps from modified look- locker inversion recovery sequence”. In: *PLoS ONE* 10.5 (2015).
- [54] Christos G Xanthis et al. “Parallel simulations for QUAntifying RELaxation magnetic resonance constants (SQUAREMR): an example towards accurate MOLLI T1 measurements”. In: *Journal of cardiovascular magnetic resonance : official journal of the Society for Cardiovascular Magnetic Resonance* 17.104 (2015).

-
- [55] Hui Xue et al. “Improved motion correction using image registration based on variational synthetic image estimation: application to inline t1 mapping of myocardium”. In: *Journal of Cardiovascular Magnetic Resonance* 13.Suppl 1 (2011), P21.
 - [56] Hui Xue et al. “Motion Correction for Myocardial T1 Mapping using Image Registration with Synthetic Image Estimation”. In: *Magnetic Resonance in Medicine* 67.6 (2012), pp. 1644–1655.
 - [57] Sebastien Roujol et al. “Adaptive Registration of Varying Contrast-Weighted Images for Improved Tissue Characterization (ARCTIC): Application to T1 Mapping”. In: *Magnetic Resonance in Medicine* 73.4 (2015), pp. 1469–1482.
 - [58] Yanjie Zhu et al. “Integrated motion correction and dictionary learning for free-breathing myocardial T1 mapping”. In: *Magnetic Resonance in Medicine* 81 (2019), pp. 2644–2654.
 - [59] Kelvin Chow et al. “Robust free-breathing SASHA T1 mapping with high-contrast image registration”. In: *Journal of Cardiovascular Magnetic Resonance* 18.47 (2016).
 - [60] Sebastian Weingärtner et al. “Free-breathing post-contrast three-dimensional T1 mapping: Volumetric assessment of myocardial T1 values”. In: *Magnetic Resonance in Medicine* 73.1 (2015), pp. 214–222.
 - [61] Giovanna Nordio et al. “3D Myocardial T1 Mapping Using Saturation Recovery”. In: *Journal of Magnetic Resonance Imaging* 46 (2017), pp. 218–227.
 - [62] Giovanna Nordio et al. “Whole-heart T1 mapping using a 2D fat image navigator for respiratory motion compensation”. In: *Magnetic Resonance in Medicine* 83 (2020), pp. 178–187.
 - [63] Jaime Shaw et al. “3D Whole-Ventricle, Free-Breathing, Non-ECG, Myocardial T1 and ECV Mapping with CMR Multitasking”. In: *Proceedings of the 26th Annual Meeting of ISMRM, Paris, France*. 2018, p. 4872.
 - [64] Haikun Qi et al. “Free-running 3D whole heart myocardial T1 mapping with isotropic spatial resolution”. In: *Magnetic Resonance in Medicine* 82.4 (2019), pp. 1331–1342.
 - [65] Michael Lustig, David Donoho, and John M. Pauly. “Sparse MRI: The application of compressed sensing for rapid MR imaging”. In: *Magnetic Resonance in Medicine* 58.6 (2007), pp. 1182–1195.
 - [66] Tamara G. Kolda and Brett W. Bader. “Tensor Decompositions and Applications”. In: *SIAM Review* 51.3 (2009), pp. 455–500.
 - [67] Dan Ma et al. “Magnetic resonance fingerprinting”. In: *Nature* 495.7440 (2013), pp. 187–192.
 - [68] Jesse I Hamilton et al. “MR fingerprinting for rapid quantification of myocardial T1, T2, and proton spin density”. In: *Magnetic Resonance in Medicine* 77.4 (2017), pp. 1446–1458.
 - [69] Gastao Cruz et al. “Cardiac Magnetic Resonance Fingerprinting: Technical Developments and Initial Clinical Validation”. In: *Current Cardiology Reports* 21.91 (2019).

REFERENCES

- [70] Bhairav B Mehta et al. “Accelerated and navigator-gated look-locker imaging for cardiac t1 estimation (ANGIE): Development and application to T1 mapping of the right ventricle”. In: *Magnetic Resonance in Medicine* 160 (2014), pp. 150–160.
- [71] Sebastian Weingaertner et al. “Temporally Resolved Parametric Assessment of Z-Magnetization Recovery (TOPAZ): Dynamic Myocardial T 1 Mapping Using a Cine Steady-State Look-Locker Approach”. In: *Magnetic Resonance in Medicine* (2017).
- [72] Daniel R. Messroghli et al. “Small Animal Look-Locker Inversion Recovery (SALLI) for Simultaneous Generation of Cardiac T1 Maps and Cine and Inversion Recovery-prepared Images at High Heart Rates: Initial Experience”. In: *Radiology* 261.1 (2011), pp. 258–265.
- [73] Anthony G Christodoulou et al. “Magnetic resonance multitasking for motion-resolved quantitative cardiovascular imaging”. In: *Nature Biomedical Engineering* 2 (2018), pp. 215–226.
- [74] Haikun Qi et al. “Free-running simultaneous myocardial T1/T2 mapping and cine imaging with 3D whole-heart coverage and isotropic spatial resolution”. In: *Magnetic Resonance Imaging* 63 (2019), pp. 159–169.
- [75] Philipp Ehse et al. “IR TrueFISP with a golden-ratio-based radial readout: Fast quantification of T1, T2, and proton density”. In: *Magnetic Resonance in Medicine* 69 (2013), pp. 71–81.
- [76] Johannes Tran-Gia et al. “Model-based Acceleration of Parameter mapping (MAP) for saturation prepared radially acquired data”. In: *Magnetic Resonance in Medicine* 70 (2013), pp. 1524–1534.
- [77] Johannes Tran-Gia et al. “Model-Based Acceleration of Look-Locker T1 Mapping”. In: *PLoS ONE* 10.4 (2015).
- [78] R Deichmann and A Haase. “Quantification of T1 Values by SNAPSHOT-FLASH NMR Imaging”. In: *Journal of Magnetic Resonance* 96 (1992), pp. 608–612.
- [79] A. Haase et al. “FLASH imaging. Rapid NMR imaging using low flip-angle pulses”. In: *Journal of Magnetic Resonance (1969)* 67.2 (1986), pp. 258–266.
- [80] R. R. Ernst and W. A. Anderson. “Application of fourier transform spectroscopy to magnetic resonance”. In: *Review of Scientific Instruments* 37.1 (1966), pp. 93–102.
- [81] Andrew D Scott, Jennifer Keegan, and David N Firmin. “Motion in cardiovascular MR imaging”. In: *Radiology* 250.2 (2009), pp. 331–351.
- [82] Kazuki Shimada et al. “In vivo Measurement of Longitudinal Relaxation Time of Human Blood by Inversion-recovery Fast Gradient-echo MR Imaging at 3T”. In: *Magnetic Resonance in Medical Sciences* 11.4 (2012), pp. 265–271.
- [83] N. G. Bellenger et al. “Comparison of left ventricular ejection fraction and volumes in heart failure by echocardiography, radionuclide ventriculography and cardiovascular magnetic resonance. Are they interchangeable?” In: *European Heart Journal* 21.16 (2000), pp. 1387–1396.

-
- [84] Valentina O. Puntmann et al. “T1-Mapping and Outcome in Nonischemic Cardiomyopathy All-Cause Mortality and Heart Failure”. In: *JACC: Cardiovascular Imaging* 9.1 (2016), pp. 40–50.
 - [85] Erik B Schelbert and Daniel R Messroghli. “State of the Art: Clinical Applications of Cardiac T1 Mapping”. In: *Radiology* 278.3 (2016), pp. 658–676.
 - [86] Daniel R Messroghli et al. “Clinical recommendations for cardiovascular magnetic resonance mapping of T1 , T2 , T2 * and extracellular volume : A consensus statement by the Society for Cardiovascular Magnetic Resonance (SCMR) endorsed by the European Association for Cardiovascular”. In: *Journal of Cardiovascular Magnetic Resonance* 19:75 (2017), pp. 1–24.
 - [87] Stefan K. Piechnik et al. “Shortened Modified Look-Locker Inversion recovery (ShMOLLI) for clinical myocardial T1-mapping at 1.5 and 3 T within a 9 heartbeat breathhold”. In: *Journal of Cardiovascular Magnetic Resonance* 12.69 (2010).
 - [88] Donnie Cameron et al. “Towards accurate and precise T1 and extracellular volume mapping in the myocardium: a guide to current pitfalls and their solutions”. In: *Magnetic Resonance Materials in Physics, Biology and Medicine* (2017).
 - [89] Kai Tobias Block, Martin Uecker, and Jens Frahm. “Model-based iterative reconstruction for radial fast spin-echo MRI”. In: *IEEE Transactions on Medical Imaging* 28.11 (2009), pp. 1759–1769.
 - [90] Tilman J. Sumpf et al. “Fast T2 Mapping With Improved Accuracy Using Undersampled Spin-Echo MRI and Model-Based Reconstructions With a Generating Function”. In: *IEEE Transactions on Medical Imaging* 33.12 (2014), pp. 2213–2222.
 - [91] Noam Ben-Eliezer et al. “Accelerated and motion-robust in vivo T2 mapping from radially undersampled data using Bloch-simulation-based iterative reconstruction”. In: *Magnetic Resonance in Medicine* 75.3 (2016), pp. 1346–1354.
 - [92] Xiaoqing Wang et al. “Model-based T1mapping with sparsity constraints using single-shot inversion-recovery radial FLASH”. In: *Magnetic Resonance in Medicine* 79.2 (2018), pp. 730–740.
 - [93] Stefanie Winkelmann et al. “An Optimal Radial Profile Order Based on the Golden Ratio for Time-Resolved MRI”. In: *IEEE Transactions on Medical Imaging* 26.1 (2007), pp. 68–76.
 - [94] Nicole Seiberlich et al. “Self-Calibrating GRAPPA Operator Gridding for Radial and Spiral Trajectories”. In: *Magnetic Resonance in Medicine* 59 (2008), pp. 930–935.
 - [95] Inati Souheil J, Michael S Hansen, and Peter Kellman. “A solution to the phase problem in adaptive coil combination”. In: *Proceedings of the 21th Annual Meeting of ISMRM, Salt Lake City, USA*. 2013, p. 2672.
 - [96] W. P. Segars et al. “4D XCAT phantom for multimodality imaging research”. In: *Medical Physics* 37.9 (2010), p. 4902.
 - [97] Lukas Wissmann et al. “MRXCAT: Realistic numerical phantoms for cardiovascular magnetic resonance”. In: *Journal of Cardiovascular Magnetic Resonance* 16.63 (2014).

REFERENCES

- [98] Manuel D Cerqueira et al. “Standardized Myocardial Segmentation and Nomenclature for Tomographic Imaging of the Heart: A Statement for Healthcare Professionals From the Cardiac Imaging”. In: *Circulation* 105.4 (2002), pp. 539–542.
- [99] Jeffrey Tsao, Peter Boesiger, and Klaas P Pruessmann. “k-t BLAST and k-t SENSE: Dynamic MRI With High Frame Rate Exploiting Spatiotemporal Correlations”. In: *Magnetic Resonance in Medicine* 50.5 (2003), pp. 1031–1042.
- [100] Roberto M Lang et al. “Recommendations for chamber quantification”. In: *European Journal of Echocardiography* 7 (2006), pp. 79–108.
- [101] Jason J Lee et al. “Myocardial T1 and Extracellular Volume Fraction Mapping at 3 Tesla”. In: *Journal of Cardiovascular Magnetic Resonance* 13.75 (2011).
- [102] Benjamin Marty, B Coppà, and P G Carlier. “Fast, Precise and Accurate Myocardial T1 Mapping Using a Radial MOLLI Sequence With FLASH Readout”. In: *Magnetic Resonance in Medicine* 79 (2018), pp. 1387–1398.
- [103] Florian von Knobelsdorff-Brenkenhoff et al. “Myocardial T1 and T2 mapping at 3 T: reference values, influencing factors and implications”. In: *Journal of Cardiovascular Magnetic Resonance* 15.53 (2013).
- [104] Gary Glover and John Pauly. “Projection reconstruction techniques for reduction of motion effects in MRI”. In: *Magnetic Resonance in Medicine* 28.2 (1992), pp. 275–289.
- [105] Jeanette Schulz-Menger et al. “Standardized image interpretation and post processing in cardiovascular magnetic resonance : Society for Cardiovascular Magnetic Resonance (SCMR) Board of Trustees Task Force on Standardized Post Processing”. In: *Journal of Cardiovascular Magnetic Resonance* 15.35 (2013).
- [106] Holger Thiele et al. “Improved Accuracy of Quantitative Assessment of Left Ventricular Volume and Ejection Fraction by Geometric Models with Steady-State Free Precession”. In: *Journal of Cardiovascular Magnetic Resonance* 4.3 (2002), pp. 327–339.
- [107] Peter Kellman et al. “Characterization of myocardial T1-mapping bias caused by intramyocardial fat in inversion recovery and saturation recovery techniques”. In: *Journal of Cardiovascular Magnetic Resonance* 17.1 (2015).
- [108] Ursula Reiter et al. “Normal Diastolic and Systolic Myocardial T1 Values at 1.5-T MR Imaging: Correlations and Blood Normalization.” In: *Radiology* 271.2 (2013), pp. 365–372.
- [109] Ralf Wassmuth et al. “Variability and homogeneity of cardiovascular magnetic resonance myocardial T2-mapping in volunteers compared to patients with edema”. In: *Journal of Cardiovascular Magnetic Resonance* 15.27 (2013).
- [110] A Boldt et al. “Fibrosis in left atrial tissue of patients with atrial fibrillation with and without underlying mitral valve disease”. In: *Heart* 90.4 (2004), pp. 400–405.
- [111] Christopher J McGann et al. “New Magnetic Resonance Imaging-Based Method for Defining the Extent of Left Atrial Wall Injury After the Ablation of Atrial Fibrillation”. In: *Journal of American College of Cardiology* 52.15 (2008), pp. 1263–1271.

- [112] Roy Beinart et al. “Cardiac magnetic resonance T1 mapping of left atrial myocardium”. In: *Heart Rhythm* 10.9 (2013), pp. 1325–1331.
- [113] Alex J A McLellan et al. “Diffuse Ventricular Fibrosis Measured by T 1 Mapping on Cardiac MRI Predicts Success of Catheter Ablation for Atrial Fibrillation”. In: *Circulation: Arrhythmia and Electrophysiology* 7.5 (2014), pp. 834–840.
- [114] Zhong Chen et al. “Myocardial tissue characterization by cardiac magnetic resonance imaging using T1 mapping predicts ventricular arrhythmia in ischemic and non-ischemic cardiomyopathy patients with implantable cardioverter-defibrillators”. In: *Heart Rhythm* 12.4 (2015), pp. 792–801.
- [115] Kirsten M Becker et al. “Simultaneous high-resolution cardiac T1 mapping and cine imaging using model-based iterative image reconstruction”. In: *Magnetic Resonance in Medicine* 81.2 (2019), pp. 1080–1091.
- [116] Jianing Pang et al. “High efficiency coronary MR angiography with nonrigid cardiac motion correction”. In: *Magnetic Resonance in Medicine* 76.5 (2016), pp. 1345–1353.
- [117] Christoph Kolbitsch et al. “Cardiac and Respiratory Motion Correction for Simultaneous Cardiac PET/MR”. In: *Journal of Nuclear Medicine* 58.5 (2017), pp. 846–852.
- [118] Sébastien Roujol et al. “Impact of motion correction on reproducibility and spatial variability of quantitative myocardial T2 mapping”. In: *Journal of Cardiovascular Magnetic Resonance* 17.46 (2015).
- [119] Sebastian Weingärtner et al. “Free-breathing multislice native myocardial T1 mapping using the slice-interleaved T1 (STONE) sequence”. In: *Magnetic Resonance in Medicine* 74.1 (2015), pp. 115–124.
- [120] Kai Tobias Block, Martin Uecker, and Jens Frahm. “Undersampled radial MRI with multiple coils. Iterative image reconstruction using a total variation constraint”. In: *Magnetic Resonance in Medicine* 57.6 (2007), pp. 1086–1098.
- [121] D Rueckert et al. “Nonrigid Registration Using Free-Form Deformations - Application to Breat MR Images.pdf”. In: *IEEE Transactions on Medical Imaging* 18.8 (1999), pp. 712–721.
- [122] Marc Modat, Jamie McClelland, and Sébastien Ourselin. “Lung Registration Using the NiftyReg Package”. In: *MICCAI2010 Workshop: Medical Image Analysis For The Clinic - A Grand Challenge* (2010), pp. 33–42.
- [123] Klaas P Pruessmann et al. “SENSE: Sensitivity encoding for fast MRI”. In: *Magnetic Resonance in Medicine* 42.5 (1999), pp. 952–962.
- [124] Gabriella Captur et al. “A medical device-grade T1 and ECV phantom for global T1 mapping quality assurance - the T1 Mapping and ECV Standardization in cardiovascular magnetic resonance (T1MES) program”. In: *Journal of Cardiovascular Magnetic Resonance* 18.58 (2016).
- [125] Stefan K. Piechnik et al. “Normal variation of magnetic resonance T1 relaxation times in the human population at 1.5 T using ShMOLLI”. In: *Journal of Cardiovascular Magnetic Resonance* 15.13 (2013).

REFERENCES

- [126] Wang Zhou. “A Universal Image Quality Index”. In: *IEEE Signal Processing Letters* (2002).
- [127] J. Jane Cao et al. “A comparison of both DENSE and feature tracking techniques with tagging for the cardiovascular magnetic resonance assessment of myocardial strain”. In: *Journal of Cardiovascular Magnetic Resonance* 20.26 (2018).
- [128] Dina Radenkovic et al. “T1mapping in cardiac MRI”. In: *Heart Failure Reviews* 22.4 (2017), pp. 415–430.
- [129] Peter Kellman et al. “Extracellular volume fraction mapping in the myocardium , part 1: evaluation of an automated method”. In: *Journal of Cardiovascular Magnetic Resonance* 14.63 (2012).
- [130] Hiroshi Ashikaga et al. “Changes in regional myocardial volume during the cardiac cycle: implications for transmural blood flow and cardiac structure”. In: *American journal of physiology. Heart and circulatory physiology* 295.2 (2008), H610–H618.
- [131] Anthony G Christodoulou et al. “A general low-rank tensor framework for high-dimensional cardiac imaging: Application to time-resolved T1 mapping”. In: *Proceedings of the 24th Annual Meeting of ISMRM, Singapore, Singapore*. 2016, p. 867.
- [132] Bo Zhu et al. “Image reconstruction by domain-transform manifold learning”. In: *Nature* 555 (2018), pp. 487–492.

List of Author's Publications

Journal Articles

- J1 **Kirsten M Becker**, Edyta Blaszczyk, Stephanie Funk, André Nuesslein, Jeanette Schulz-Menger, Tobias Schaeffter, Christoph Kolbitsch, Fast myocardial T1 mapping using cardiac motion correction, *Magnetic Resonance in Medicine*, 2020;83:438-451, DOI: [10.1002/mrm.27935](https://doi.org/10.1002/mrm.27935), CC BY 4.0.
- J2 **Kirsten M Becker**, Jeanette Schulz-Menger, Tobias Schaeffter, Christoph Kolbitsch, Simultaneous high-resolution cardiac T1 mapping and cine imaging using model-based iterative image reconstruction, *Magnetic Resonance in Medicine*, 2019;81:1080–1091, DOI: [10.1002/mrm.27474](https://doi.org/10.1002/mrm.27474).
- J3 Evita C Wiegers*, **Kirsten M Becker***, Hanne M Rooijackers, Federico C von Samson-Himmelstjerna, Cees J Tack, Arend Heerschap, Bastiaan E de Galan, Marinette van der Graaf, Cerebral blood flow response to hypoglycemia is altered in patients with type 1 diabetes and impaired awareness of hypoglycemia, *Journal of Cerebral Blood Flow & Metabolism*, 2017;37(6):1994–2001, DOI: [10.1177/0271678x16658914](https://doi.org/10.1177/0271678x16658914), *: shared first authorship.

Conference Proceedings

- C1 Sven Lukanek, Jeanette Schulz-Menger, Tobias Schaeffter, Christoph Kolbitsch, **Kirsten M Becker**, Efficient cardiac T1 mapping using cardiac motion correction at 1.5 T, *Proceedings of the 36th Annual Meeting of ESMRMB*, Rotterdam, The Netherlands, 2019.
- C2 **Kirsten M Becker**, Edyta Blaszczyk, Stephanie Funk, Jeanette Schulz-Menger, Tobias Schaeffter, Christoph Kolbitsch, Efficient high-resolution cardiac motion-corrected T1 mapping, *Proceedings of the 27th Annual Meeting of ISMRM*, Montreal, Canada, 2019.
- C3 Christoph Kolbitsch, **Kirsten M Becker**, Judith Lehnert, Jean-Pierre Bassenge, Xenios Milidonis, Myles Capstick, Clemens Elster, Amedeo Chiribiri, Tobias Schaeffter, Dynamic T1 Mapping for Quantitative Myocardial Perfusion Imaging, *Proceedings of the 27th Annual Meeting of ISMRM*, Montreal, Canada, 2019.
- C4 **Kirsten M Becker**, Jeanette Schulz-Menger, Tobias Schaeffter, Christoph Kolbitsch, In vivo myocardial tissue characterization of all four chambers using high-resolution quantitative MRI, 2018, *Annual meeting of the German Society for Biomedical*

9. LIST OF AUTHOR'S PUBLICATIONS

Engineering (BMT), Aachen, Germany, Current Directions in Biomedical Engineering, 2018,4(1):263-266, DOI: [10.1515/cdbme-2018-0064](https://doi.org/10.1515/cdbme-2018-0064), CC BY-NC-ND 3.0.

- C5 **Kirsten M Becker**, Jeanette Schulz-Menger, Tobias Schaeffter, Christoph Kolbitsch, Simultaneous high-resolution cardiac T1 mapping and cine imaging using model-based iterative image reconstruction, *Proceedings of the 26th Annual Meeting of ISMRM*, Paris, France, 2018.
- C6 **Kirsten M Becker**, Jeanette Schulz-Menger, Tobias Schaeffter, Christoph Kolbitsch, Multi-parametric cardiac MRI for T1 mapping and cine imaging using model-based iterative image reconstruction, *Proceedings of the 25th Annual Meeting of ISMRM*, Honolulu, US, 2017.
- C7 Evita C Wieggers, **Kirsten M Becker**, Hanne M Rooijackers, Cees J Tack, Arend Heerschap, Marinette van der Graaf, Bastiaan E de Galan, Cerebral blood flow response to hypoglycemia is altered in patients with type 1 diabetes and impaired awareness of hypoglycemia, *Proceedings of the 52nd Annual Meeting of European Association for the Study of Diabetes (EASD)*, Munich, Germany, 2016.
- C8 Evita C Wieggers, **Kirsten M Becker**, Hanne M Rooijackers, Cees J Tack, Arend Heerschap, Bastiaan E de Galan, Marinette van der Graaf, Hypoglycemia-Induced Changes in Global and Regional Cerebral Blood Flow; Impact of Type 1 Diabetes and Impaired Awareness of Hypoglycemia, *Proceedings of the 24th Annual Meeting of ISMRM*, Singapore, 2016.
- C9 **Kirsten M Becker**, Evita C Wieggers, Hanne M Rooijackers, Cees J Tack, Arend Heerschap, Bastiaan E de Galan, Marinette van der Graaf, Altered cerebral blood flow during hypoglycemia in patients with type 1 diabetes and impaired hypoglycemic awareness – initial results, *Proceedings of the Annual Meeting of ESMRMB*, Edinburgh, UK, 2015.
- C10 Evita C Wieggers, **Kirsten M Becker**, Hanne M Rooijackers, Cees J Tack, Arend Heerschap, Bastiaan E de Galan, Marinette van der Graaf, Hypoglycemia increases global cerebral blood flow in patients with type 1 diabetes and impaired awareness of hypoglycemia, *Proceedings of the Annual Dutch Diabetes Research Meeting (ADDRM)*, Oosterbeek, The Netherlands, 2015.